COO-1574-38

EXPERIMENTAL AND THEORETICAL STUDIES IN LOW TEMPERATURE PHYSICS: SUBLIMATION AND VAPOR PRESSURE OF Ar^{36} AND THE COMBINED EFFECTS OF PHONON ATTENUATION AND IMPEDANCE MATCHING ON KAPITZA RESISTANCE

By

Jon Lynn Opsal

A DISSERTATION

Submitted to

Michigan State University

in partial fulfillment of the requirements

for the degree of

DOCTOR OF PHILOSOPHY

MASTER

Department of Physics

1974

DISTRIBUTION OF THIS DOCUMENT IS UNLIMITED

DISCLAIMER

This report was prepared as an account of work sponsored by an agency of the United States Government. Neither the United States Government nor any agency Thereof, nor any of their employees, makes any warranty, express or implied, or assumes any legal liability or responsibility for the accuracy, completeness, or usefulness of any information, apparatus, product, or process disclosed, or represents that its use would not infringe privately owned rights. Reference herein to any specific commercial product, process, or service by trade name, trademark, manufacturer, or otherwise does not necessarily constitute or imply its endorsement, recommendation, or favoring by the United States Government or any agency thereof. The views and opinions of authors expressed herein do not necessarily state or reflect those of the United States Government or any agency thereof.

DISCLAIMER

Portions of this document may be illegible in electronic image products. Images are produced from the best available original document.

MASTER

NOTICE
This report was prepared as an account of work sponsored by the United States Government. Neither the United States nor the United States Atomic Energy Commission, nor any of their employees, nor any of contractors, subcontractors, or their employees, any warranty, express or implied, or assumes any bility or responsibility for the accuracy, completeness or usefulness of any information, apparatus, product or process disclosed, or represents that its use would not infringe privately owned rights.

ABSTRACT

EXPERIMENTAL AND THEORETICAL STUDIES IN LOW TEMPERATURE PHYSICS: SUBLIMATION AND VAPOR PRESSURE OF Ar^{36} AND THE COMBINED EFFECTS OF PHONON ATTENUATION AND IMPEDANCE MATCHING ON KAPITZA RESISTANCE

By

Jon Lynn Opsal

The sublimation and vapor pressure of Ar^{36} were measured in the temperature range 23.752-87.375 K. Pressures below 1 Torr were measured with a McLeod gauge and corrected for effects of thermal transpiration and mercury streaming. The estimated accuracy of these pressure measurements ranges from 1% near 1 Torr to 10% near 10^{-5} Torr. Above 1 Torr a calibrated Bourdon gauge was used to give pressures to ± 0.03 Torr. Temperatures were measured to ± 3 mK with a N.B.S.-calibrated Pt resistance thermometer. A liquid helium bath was used throughout the temperature range for which the experiment was done. The data were fit to theoretical sublimation pressure curves to obtain values for the static lattice energy, lattice vibrational energy, and geometric mean frequency of the phonon spectrum. The data were also compared with theoretical calculations of others based on an anharmonic self-consistent phonon theory. Equivalent sublimation-pressure data on normal Ar are compared with our Ar^{36} data in the temperature range 62.315-84.503 K. This comparison yields vapor-pressure ratios which are in reasonable agreement with theory and other experiments. Thermodynamic properties of normal Ar and of Ar^{36} calculated from these data are also compared. It is found that several of the differences in properties may be qualitatively understood in terms of the increased

MASTER

DISTRIBUTION OF THIS DOCUMENT IS UNLIMITED

zero-point energy of Ar^{36} compared to normal Ar.

The Kapitza resistance, $R_K(T)$, is calculated for a Cu-He^4 interface using the acoustic mismatch theory of Khalatnikov and of Mazo and Onsager. Included in the calculation are the effects of: phonon attenuation in the copper as well as impedance matching due to the increased He density near the interface. We calculate $R_K(T)$ for several values of attenuation in the Cu; detailed calculations are displayed for the case of equal attenuations for longitudinal and transverse waves in the solid. Also considered are different attenuation profiles in the Cu. We use a density profile, for the He, calculated from compressibility data and the van der Waals attractive force between He and the Cu substrate. Our model includes the effect of a solid layer of He at the copper surface, i.e. in such a He layer both longitudinal and transverse waves are allowed. Included in our calculations are the effects of different density profiles for the He. The calculations indicate that for suitable choices of the physical parameters, the theoretical results for $R_K(T)$ agree in magnitude as well as T dependence with the experimental data. Unfortunately, the important physical properties have not yet been experimentally determined and a definitive test of this theory must await such data.

EXPERIMENTAL AND THEORETICAL STUDIES IN LOW TEMPERATURE PHYSICS: SUBLIMATION AND VAPOR PRESSURE OF Ar^{36} AND THE COMBINED EFFECTS OF PHONON ATTENUATION AND IMPEDANCE MATCHING ON KAPITZA RESISTANCE

By

Jon Lynn Opsal

A DISSERTATION

Submitted to

Michigan State University

in partial fulfillment of the requirements

for the degree of

DOCTOR OF PHILOSOPHY

Department of Physics

1974

ACKNOWLEDGMENTS

I should like to express my deep appreciation to Professor G.L. Pollack, who suggested both the experiment and theoretical problem, for his helpful supervision throughout the course of this research. I would also like to thank David Christen and Thomas Milbrodt for their assistance in doing the experiments and for their many helpful discussions and suggestions during the course of the theoretical calculation.

Special thanks are also due to Professor R.D. Spence for several conversations and much valuable advice relating to the theoretical calculation. Finally, I would like to acknowledge the financial support of the United States Atomic Energy Commission and the National Science Foundation.

TABLE OF CONTENTS

Chapter		Page
I.	INTRODUCTION	1
	A. Discussion of Sublimation and Vapor Pressure	1
	B. Description of the Kapitza Resistance Effect	2
II.	THE EXPERIMENT ON SUBLIMATION AND VAPOR PRESSURE	6
	A. Theory	6
	B. Experimental Method	11
	1. Temperature Measurement	12
	2. Pressure Measurement	14
	3. Gas Sample Analysis	17
	C. Results of the Experiment	17
	1. Discussion of Equation 16	21
	2. Obtaining Thermodynamic Properties From the Data	25
	D. Discussion	27
	1. Behavior of Lattice Vibrational Energy	30
	2. Comparing Properties of Ar^{36} and Ar^{N}	30
	3. Comparison with the Work of Others	34
III.	THE THEORETICAL CALCULATION OF KAPITZA RESISTANCE	36
	A. The Model	36
	B. Theory	39
	1. Elastic and Viscoelastic Materials	39
	2. The Heat Flux and Kapitza Resistance	44
	C. Numerical Method	44
	D. Discussion	45
	1. Effects Due to Phonon Attenuation	45
	2. Effects of Including Impedance Matching	47
IV.	SUMMARY AND CONCLUSIONS	69
	A. The Sublimation and Vapor Pressure Experiment	69
	B. The Calculation of Kapitza Resistance	70
Appendices		
A.	DECOMPOSITION OF THE DISPLACEMENT FIELD	72
B.	THE ENERGY FLUX	74

Appendices

		Page
C.	THE TRANSMISSION COEFFICIENTS.	76
D.	KAPITZA RESISTANCE PROGRAM	80
E.	ADDITIONAL FIGURES OF TR	94
F.	TABULATION OF CALCULATED $R_K T^3$ VALUES	108
	LIST OF REFERENCES.	114

LIST OF TABLES

Table		Page
1	Experimental Sublimation- and vapor-pressure and temperature data.	19
2	Typical values of various terms which appear in Equation 16.	24
3	The static lattice energy, E_o, and geometric mean of the lattice vibrational spectrum, ω_g, calculated from our data using Equation 16, are shown in the second and fourth columns, respectively. The third column shows the values of the heat of sublimation calculated from our data using Equation 5.	26
4	Lattice vibrational energies calculated from Equation 20 are shown in the second column. Theoretically predicted values from Equation 22 are shown in the third column.	28
5	Comparison of sublimation pressures of Ar^{36} and Ar^N. Data for Ar^N in the temperature range 62.315-74.681 K are taken from Reference 1. For the temperature range 75.557-84.503 K, the unpublished data on Ar^N of Christen and Opsal[37] are used.	31
6	Kapitza resistance, R_K, in the form R_KT^3, as a function of phonon attenuation in the copper.	46
D1	List of the FORTRAN program, KR and its subroutines, used to calculate the Kapitza resistance.	80
F1	Kapitza resistance, R_K, in the form R_KT^3, as a function of phonon attenuation in the copper.	108
F2	Calculated R_KT^3 values used in Figure 8.	110
F3	Calculated R_KT^3 values used in Figures 9-11.	111
F4	Calculated R_KT^3 values used in Figures 12 and 13.	112
F5	Calculated R_KT^3 values for Figures 14-17.	113

LIST OF FIGURES

Figure		Page
1	A sketch of the apparatus used for this experiment.	13
2	Sublimation pressure of Ar^{36} as a function of temperature.	18
3	Plot of $\ell n(PT^{1/2})$ versus 1/T for data ranging from T = 68.902 K, P = 44.47 Torr to T = 83.639 K, P = 510.82 Torr.	22
4	A system of solid and liquid layers typical of those used in the calculations.	42
5	Calculated energy transmission coefficient, TR, at three frequencies as a function of angle of incidence. The frequencies are expressed in terms of temperatures defined by $\omega = 3.7 \times 10^{11} T$ (sec^{-1}). Both longitudinal and transverse waves are included in the first, most dense He layer.	48
6	TR calculated at three frequencies. Only longitudinal waves are included in the first He layer.	49
7	TR calculated at three frequencies. Only longitudinal waves are included in the first He layer.	52
8	$R_K T^3$ calculated as a function of temperature T. For the lower curve both longitudinal and transverse waves are included in the first helium layer, while only longitudinal waves in the first helium layer are used to calculate the upper curve.	57
9	$R_K T^3$ calculated for two attenuations in the copper. The first helium layer is considered to be a solid; i.e., both longitudinal and transverse are used.	58
10	$R_K T^3$ calculated for two attenuations with a helium density factor F = 1.4.	59
11	$R_K T^3$ calculated for two attenuations with a helium density factor F = 1.5.	60

Figure		Page
12	$R_K T^3$ calculated for two attenuations and a helium density factor F = 1.4. Transverse waves are included only in the first, most dense, helium layer.	61
13	$R_K T^3$ calculated for two attenuations and a helium density factor F = 1.5. Transverse waves are included only in the first, most dense, helium layer.	62
14	$R_K T^3$ calculated using an attenuation profile in the copper V = 0.25 for a layer which extends from the copper surface 20 Å into the copper, and V = 0.12 beyond the layer. The individual points are experimental values; ▲ - Reference 21, + - Reference 51, □ - Reference 52, x - Reference 55.	65
15	$R_K T^3$ calculated using an attenuation profile in the copper: V = 0.30 for 20 Å, V = 0.12 for the next 250 Å, and V = 0.6 beyond the layers. The individual points are experimental values; ▲ - Reference 21, + - Reference 51, □ - Reference 52, x - Reference 55.	66
16	$R_K T^3$ calculated using an attenuation profile in the copper: V = 0.42 for 25 Å, V = 0.12 for the next 250 Å, and V = 0.06 beyond the layers. The individual points are experimental values; ▲ - Reference 21, + - Reference 51, □ - Reference 52, x - Reference 55.	67
17	$R_K T^3$ calculated using an attenuation profile in the copper: V = 0.50 for 25 Å, V = 0.12 for the next 100 Å, and V = 0.06 beyond the layers. The individual points are experimental values; ▲ - Reference 21, + - Reference 51, □ - Reference 52, x - Reference 55.	68
E1	TR calculated at frequencies corresponding to the temperatures; 1.6, 1.75, 2.0 and 3.0 K. Only longitudinal waves are included in the first He layer.	95
E2	TR calculated at frequencies corresponding to the temperatures; 0.1, 1.0, 1.25 and 1.4 K.	96
E3	TR calculated at frequencies corresponding to the temperatures 1.43, 1.44, 1.45, and 1.46 K.	97
E4	TR calculated at frequencies corresponding to the temperatures; 1.47, 1.48, 1.49, and 1.5 K.	98
E5	TR calculated at frequencies corresponding to the temperatures; 1.55, 1.6, 1.75, and 2.0 K.	99
E6	TR calculated at frequencies corresponding to the temperatures; 2.25, 2.5, 2.75, and 3.0 K.	100

Figure		Page
E7	TR calculated at frequencies corresponding to the temperatures 3.25, 3.5, 3.75, and 4.0 K.	101
E8	TR calculated for a small attenuation, V = 0.01, at frequences corresponding to the temperatures; 0.1, 1.0, 1.25, and 1.4 K.	102
E9	TR calculated for a small attenuation, V = 0.01, at frequencies corresponding to the temperatures; 1.43, 1.44, 1.45, and 1.46 K.	103
E10	TR calculated for a small attenuation, V = 0.01, at frequencies corresponding to the temperatures; 1.47, 1.48, 1.49, and 1.5 K.	104
E11	TR calculated for a small attenuation, V = 0.01, at frequencies corresponding to the temperatures; 1.55, 1.6, 1.75, and 2.0 K.	105
E12	TR calculated for a small attenuation, V = 0.01, at frequencies corresponding to the temperatures; 2.25, 2.5, 2.75, and 3.0 K.	106
E13	TR calculated for a small attenuation, V = 0.1, at frequencies corresponding to the temperatures; 3.25, 3.5, 3.75, and 4.0 K.	107

I. INTRODUCTION

There are many areas for fundamental theoretical and experimental research in low temperature physics. This thesis deals with two different phenomena which occur at low temperatures: The first is an experiment to measure the sublimation and vapor pressure of the argon isotope, Ar^{36}, in the temperature range 23.752-87.375 K. In the second, we make a theoretical investigation of the thermal boundary resistance which occurs at the interface between two different materials when heat flows across the interface. This effect is commonly known as Kapitza resistance and is most pronounced between liquid He^4 (or He^3) and a dense, elastic solid, for example a metal at very low temperatures, $T \lesssim 1$ K.

The sublimation and vapor pressure experiment is discussed in Chapter II of this thesis and the theoretical calculation of Kapitza resistance is the topic of Chapter III.

A. Discussion of Sublimation and Vapor Pressure

Properties of the rare-gas solids have long been of interest because the interatomic forces are weak, short-ranged, and relatively well understood. To a good approximation these forces can be represented by two-body central forces, and comparatively simple theories can therefore be used to predict properties of the rare-gas solids. In particular sublimation pressure is calculable from lattice-dynamical theories and consequently can be used as a test of such theories. The

purpose of this experiment is to provide an accurate table of sublimation-pressure data for Ar^{36} which extend over several orders of magnitude. From these data we calculate the static lattice energy, heat of sublimation, vibrational energy, and geometric mean frequency of the phonon spectrum. Since the sublimation pressure of normal argon (Ar^N) has been measured previously with the same apparatus,[1,2] we compare the sublimation pressure of Ar^N with that of Ar^{36} and discuss the observed differences. We also discuss the observed differences in some of the calculated properties mentioned above.

Vapor and sublimation pressures of Ar^N have recently been measured in the range 75-85.2 K by Chen, Aziz, and Lim.[3] Lee, Fuks, and Bigeleisen[4] have, also recently, made differential measurements comparing vapor and sublimation pressures of Ar^N and Ar^{36}. Their data, in the form of $P(Ar^N)$ and $P(Ar^{36}) - P(Ar^N)$, extend from 62-102 K. Earlier measurements on the argon isotopes have been made by Clusius and co-workers[5] in the range 84-88 K, and by Boato and co-workers[6-8] in the ranges 84-119 and 72-83.7 K.

The vapor-pressure ratios for isotopes of solid Ne and Ar have been calculated by Klein, Blizard, and Goldman[9] using the improved self-consistent phonon scheme of Goldman, Horton, and Klein.[10]

B. Description of the Kapitza Resistance Effect

The thermal boundary resistance, R_K, between liquid helium and a solid is known as Kapitza resistance, and is defined by

$$R_K = A\ \Delta T/\dot{Q}\ (\mathrm{cm}^2\ \mathrm{K/W})\ . \qquad (1)$$

In Equation 1, $\dot{Q}$ is the heat flow, A is the area of the interface, and ΔT is the temperature discontinuity across the interface. Kapitza[11] discovered the phenomenon in 1941 while investigating the thermal

conductivity of superfluid He^4. He observed a temperature discontinuity, ΔT, between a heated metal surface (Cu) and the liquid helium of approximately 2 mK per mW/cm^2 of heat flux, $\dot{Q}/A$ (between 1.6 K and the lambda point). That is $R_K \approx 2\ cm^2\ mK/mW$ (= 2 cm^2 K/W) in the temperature range 1.6-2.172 K.

A possible explanation of the phenomenon was first put forth by Khalatnikov[12,13] in 1952 and later, but independently, by Mazo and Onsager.[13,14] Each of these authors treated the heat flow across the liquid-solid interface as a thermal distribution of quantized elastic waves and calculated the transmission coefficient for waves incident at the interface using classical elastic waves. Since the velocity of sound in a solid may be an order of magnitude or more larger than in liquid helium, and the density of a solid may be 1-2 orders of magnitude larger than that of liquid helium, there will be a large acoustic mismatch and the flow of phonon energy across the liquid-solid interface will therefore be impeded. R_K's calculated using this acoustic mismatch theory have a T^{-3} temperature dependence (due to assuming a Debye density of states for the phonon modes). However, experimentally observed R_K's are typically an order of magnitude or more smaller than the theoretical values and have temperature dependences ranging from T^{-2} to $T^{-4.5}$.[13]

In an attempt to resolve some of these discrepancies between theory and experiment, several alternative theories have been proposed, of which we shall mention the ones closely related to our work. Challis, Dransfeld, and Wilks[15] modified the original acoustic mismatch theory of Khalatnikov and of Mazo and Onsager by taking into account the improved matching due to the increased density of liquid He^4 near solid

surfaces.[16] They suggested that the improved acoustic matching would result in an increase in the energy flux across the liquid-solid interface and therefore decrease R_K. Although R_K calculated with their model has a temperature dependence of $T^{-4.2}$ above 1 K, we feel that the improved agreement with experiment in the magnitude of R_K is significant.

Concurrent with our present calculations of Kapitza resistance, there has been other work[17-20] dealing directly with the effects of phonon attenuation in the solid, in particular copper, on R_K. The basic assumption used in the models proposed by these other workers (and by us) is that within 1000 Å or so of the solid surface there is a region in which the phonons are more strongly attenuated than in the bulk solid. Kuang Wey-Yen[21] in analyzing his experimental R_K data for several materials considered the effects of an amorphous layer (the Beilby layer) which is formed on the surface of a cold worked metal. Such a deformed layer has a thickness of about 50-100 Å and it is estimated[21] that the transition to the bulk polycrystalline properties occurs over a distance of 10^3-10^4 Å. His analysis considered the possibility of the elastic constants being lower (hence lower sound velocities) in this amorphous region, which of course would improve the acoustic matching for the system and thereby decrease R_K. While we agree completely that the effects associated with a thin deformed layer beneath the surface of the solid (in particular phonon attenuation) are significant with respect to decreasing R_K, we feel that the impedance matching effects associated with the dense helium region at the liquid-solid interface should be included.

The purpose of the third chapter of this thesis then is to demonstrate that the combined effects of impedance matching and phonon

attenuation in the solid result in calculated Kapitza resistances which agree quite well with experimental data. We first describe the model which we use and then the theory required to obtain the desired quantity, R_K. Following this we give a brief description of the numerical techniques used and give the accuracy which we expect from such calculations. Finally, we present our results for a variety of parameters and make some comparisons with experimental data.

II. THE EXPERIMENT ON SUBLIMATION AND VAPOR PRESSURE

A. Theory

The condition for a multi-phase thermodynamic system to be in thermal equilibrium is that the specific Gibbs free energies for each of the phases in thermal equilibrium be equal. For a solid-vapor system (or liquid-vapor system) this is expressed as

$$G[\text{Vapor}] = G[\text{solid(or liquid)}] \ . \tag{2}$$

The calculations of G for each phase in Equation 2 may involve assumptions about the system which neglect properties unique to the boundary separating the two phases. This problem can be circumvented however, by treating the interface as a third phase, separate from the bulk materials on either side of the interface. That is, thermal equilibrium for a three-phase system implies equilibrium between any two phases [in particular the solid(or liquid) and vapor phases] and Equation 2 is therefore applicable in general.

Applying classical thermodynamics to a solid-vapor system (or liquid-vapor system) in thermal equilibrium yields the Clausius-Clapeyron equation which may be written[22]

$$\frac{d(\ell nP)}{d(1/T)} = \frac{-L}{R[1 - P(v_c - \bar{B})/RT]} \ . \tag{3}$$

In Equation 3 P is the pressure, T is the temperature, L is the heat of sublimation, R is the gas constant, and v_c is the molar volume of the condensed phase, i.e., the solid or liquid. The second virial

coefficient, $\mathcal{B}$, is defined by the gaseous equation of state:

$$Pv_g = RT(1 + \mathcal{B}/v_g) \ , \tag{4}$$

in which v_g is the molar volume of the gas. Over a sufficiently narrow temperature interval Equation 3 can be integrated to give the classical vapor-pressure equation:

$$\ell n \ P = A/T + B \ , \tag{5}$$

where

$$A = \frac{-L}{R[1 - P(v_c - \mathcal{B}/RT]} \ . \tag{6}$$

The heat of sublimation L may then be calculated by fitting sublimation-pressure data to Equation 5. If data for a large temperature range are available, then the temperature dependence of L may be calculated by successively applying this technique to adjacent narrow temperature intervals.

Using statistical mechanics to calculate the Gibbs free energy of the gaseous phase, a somewhat different vapor-pressure equation can be obtained. The classical partition Function, $\mathcal{Q}$, for a canonical ensemble of N particles is defined by[23]

$$\mathcal{Q} = (1/h^{3N}N!)\int dr^{3N} \ dp^{3N} \ \exp(-\beta H) \ . \tag{7}$$

In Equation 7 the variables of intergration, r_i and p_i, denote components of the canonical position and momentum coordinates, respectively. The variable H is the total hamiltonian for the system, h is Planck's constant, and β is defined by $\beta = (k_B T)^{-1}$ where k_B is Boltzmann's constant and T is the temperature. For a system of N particles in a volume V, Equation 7 can be written

$$\mathcal{Q} = (1/N!) \ (mk_B T/2\pi\hbar^2)^{3N/2} \int dr^{3N} \exp(-\beta \sum_{i<j} v_{ij}) \ , \tag{8}$$

where m is the mass of each particle, $\hbar$ is defined by $\hbar = h/2\pi$, and

ν_{ij} is the pair potential describing the interaction of the ith and jth particles, i.e., $\nu_{ij} \equiv \nu(|\vec{r}_i - \vec{r}_j|)$. Using the cluster expansion techniques described in Reference 23, the integral in Equation 8 can be evaluated to first order in ν_{ij} to give

$$\mathcal{Q} = (V^N/N!)(mk_BT/2\pi\hbar^2)^{3N/2}\ \{1 - \mathcal{B}(T)[N(N-1)/V]\}\ . \tag{9}$$

In Equation 9 the second virial coefficient, $\mathcal{B}(T)$, is defined by

$$\mathcal{B}(T) = (+1/2)\int dr^3\{1 - \exp[-\beta\nu(r)]\}\ . \tag{10}$$

The second virial coefficient defined by Equation 10 is the same as that defined by Equation 4.

For a canonical ensemble, the Helmoltz free energy, F, is given by

$$F = -(k_BT)\ell n\mathcal{Q}\ . \tag{11}$$

Using Equations 9 and 11 for the gaseous phase and the thermodynamic relation, G = F + PV, another form of the vapor-pressure equation is obtained:

$$\ell nP - P(v_c - \mathcal{B})/RT = F/RT + (5/2)\ell n(k_BT) + (3/2)\ell n(m/2\pi\hbar^2)\ . \tag{12}$$

In Equation 12, F is the Helmoltz free energy of the solid and the remaining symbols are the same as those defined in Equations 3 and 8.

For physical analysis of experimental data, it is necessary to complement Equation 12 with a theory which gives values for the Helmoltz free energy, F, of the solid. In the case of the rare-gas solids, much progress has been made in lattice-dynamical theories from which F (and consequently P) can be calculated. There are basically two forms of lattice dynamics which have been applied to the analysis of sublimation-pressure data. These are known as the quasi-harmonic and self-consistent theories of lattice dynamics. We shall now give a brief description of each of these theories.

In the quasi-harmonic theory, the fundamental assumption made is that the energy eigenstates of the solid can be accounted for solely by non-interacting phonons. A further assumption, and that which makes the theory quasi-harmonic, is that anharmonicity in the solid results only in a temperature dependent phonon frequency spectrum and volume. That is, phonon-phonon interactions are not considered. The actual frequency spectrum, as a function of temperature, is obtained by applying a variational principle to the Helmoltz free energy as a function of lattice parameter.[24] For our purposes, however, we do not require the complete theory.

Assuming a perfect monatomic crystal structure and quasi-harmonic lattice vibrations, Salter derived an expression for the vapor-pressure equation[25]:

$$\ell n(PT^{1/2}) + \exp(-g_s/k_BT) - P(v_c - B)/RT$$

$$-3\sum_{n=1}^{\infty}(-1)^{n-1}(1/n)(\hbar/2k_BT)^{2n}\langle\omega^{2n}\rangle\left[\sum_{j=1}^{\infty}(1/\pi j)^{2n}\right] = a/T + b \ , \quad (13)$$

where

$$a = E_o/R \quad (14)$$

and

$$b = 3\ell n\omega_g + (1/2)\ell n[(m/2\pi)^3(1/k_B)] \ . \quad (15)$$

In these equations, E_o is the static lattice energy and g_s is the Gibbs free energy of mono-vacancy formation. The 3N lattice frequencies, ω_i, determine the geometric mean frequency of the lattice frequencies, ω_g, and the 2nth moment of the lattice frequencies, $\langle\omega^{2n}\rangle$. The remaining symbols are the same as those defined in Equations 3 and 8. If one uses the Debye approximation for $\langle\omega^{2n}\rangle$ and truncates the infinite series in Equation 13 at the 4th order term, Equation 13

becomes;

$$\ell n(PT^{1/2}) + \exp(-g_s/k_BT) - P(v_c - \mathcal{B})/RT$$
$$- (3/40)(\Theta_D/T)^2 + (1/2240)(\Theta_D/T)^4 = a/T + b \ . \qquad (16)$$

In Equation 16, Θ_D is the characteristic Debye temperature of the solid. The static lattice energy, E_o, represents the binding energy of the solid and can therefore be calculated by summing, over all lattice sites, the potential of pair interaction evaluated at the mean separation distance for the atoms.

It should be mentioned at this point, that Equation 13 was obtained through the use of an expansion which is valid only for high temperatures, $T \gtrsim 40$ K. A difficulty with this theory then, is that in the range where it is most easily used (for example Equation 16 is valid for $T \gtrsim 58$ K) phonon-phonon interactions are important and should not be neglected. In fact, in analyzing our experimental data using Equation 16, we do obtain results which suggest that the quasi-harmonic lattice theory is not valid for such high temperatures.

The improved self-consistent phonon theory of Goldman, Horton, and Klein[10] for the Helmoltz free energy of the anharmonic crystal does include phonon-phonon interactions and appears to be a valid theory for argon even at temperatures near the triple point ($T \simeq 84$ K). In their theory, anharmonic effects are included in two ways: The change in the potential with temperature, which is consistent with temperature dependent changes in the frequency spectrum and lattice spacing (due to anharmonicity) is considered in the self-consistent portion of their theory. This results in the so-called "effective potential". The phonons thus obtained are said to be renormalized and have infinite lifetimes. Using this newly calculated "effective potential", they then

calculate the third order terms which describe interactions between renormalized phonons. This is the "improved" part of their theory. It is interesting to note that the self-consistent theory resembles the quasi-harmonic theory in that anharmonicity results in a temperature dependence in the crystal volume and frequency spectrum. However, the quasi-harmonic theory does not consider that the potential between any pair of atoms in the crystal lattice is altered by the motions of all the neighboring atoms. In the self-consistent theory, this effect is taken into account by replacing the pair potential with the thermally averaged pair potential. The self-consistent nature of the theory becomes apparent at this point: The thermally averaged potential is calculated using the phonon distribution function and summing over all phonon modes. However, the phonon modes are themselves determined by this thermally averaged potential. Such a calculation must then be iterated until a self consistent set of results is obtained.

The improved self-consistent theory of Goldman, Horton, and Klein[10] has been used to calculate vapor pressure ratios of isotopes of Ne and Ar by Klein, Blizard, and Goldman.[9] Their calculations have been carried out for both (13, 6) and (12, 6) potentials of the Lennard-Jones type using nearest neighbor interactions. We use their calculated values of the Helmoltz free energies of Ar^{36} and Ar^{40} to make comparisons of our sublimation-pressure data and vapor-pressure ratios with theory.

B. Experimental Method

A detailed description of the apparatus and experimental technique used is given in Reference 1. A schematic representation of the

apparatus is shown in Figure 1. There are, however, some important modifications which were made for this experiment.

With the gas-sample container open to the apparatus, the pressure of the gas sample at room temperature was about 180 Torr. Since this is below the triple-point pressure of Ar, it was necessary to condense the sample directly from the vapor to the solid beginning at about 76 K. The volume of the solid formed was approximately 0.15 cm^3 at 50 K. After cooling to 30 K, volatile impurities were removed by repeated fractional distillation.

The sample temperature was controlled manually with a 10-turn, 5000 - Ω potentiometer in series with a regulated power supply which supplied current to the heater on the copper block. By carefully controlling the amount of He exchange gas, the heater current required was minimized. This was done to insure that no thermal gradients would be set up along the copper block. For temperatures above 55 K, the sample temperature could in this manner be controlled during the course of a single measurement to $\pm$ 1 mK, as judged by the response of the Bourdon gauge. Temperature control below 55 K was within the limits of the thermometer accuracy, $\pm$ 3 mK. To insure that thermal equilibrium had been established such control was generally maintained for 1/2 h.

1. Temperature Measurement

The sample temperature was measured using a Pt resistance thermometer imbedded in the Cu block as shown in Figure 1. The thermometer was a four-lead Model 8164 Leeds and Northrup capsule-type and a calibration of the thermometer was supplied by the National Bureau of Standards. A small amount of vacuum grease was used to enhance the thermal contact between the thermometer and the Cu block. To further

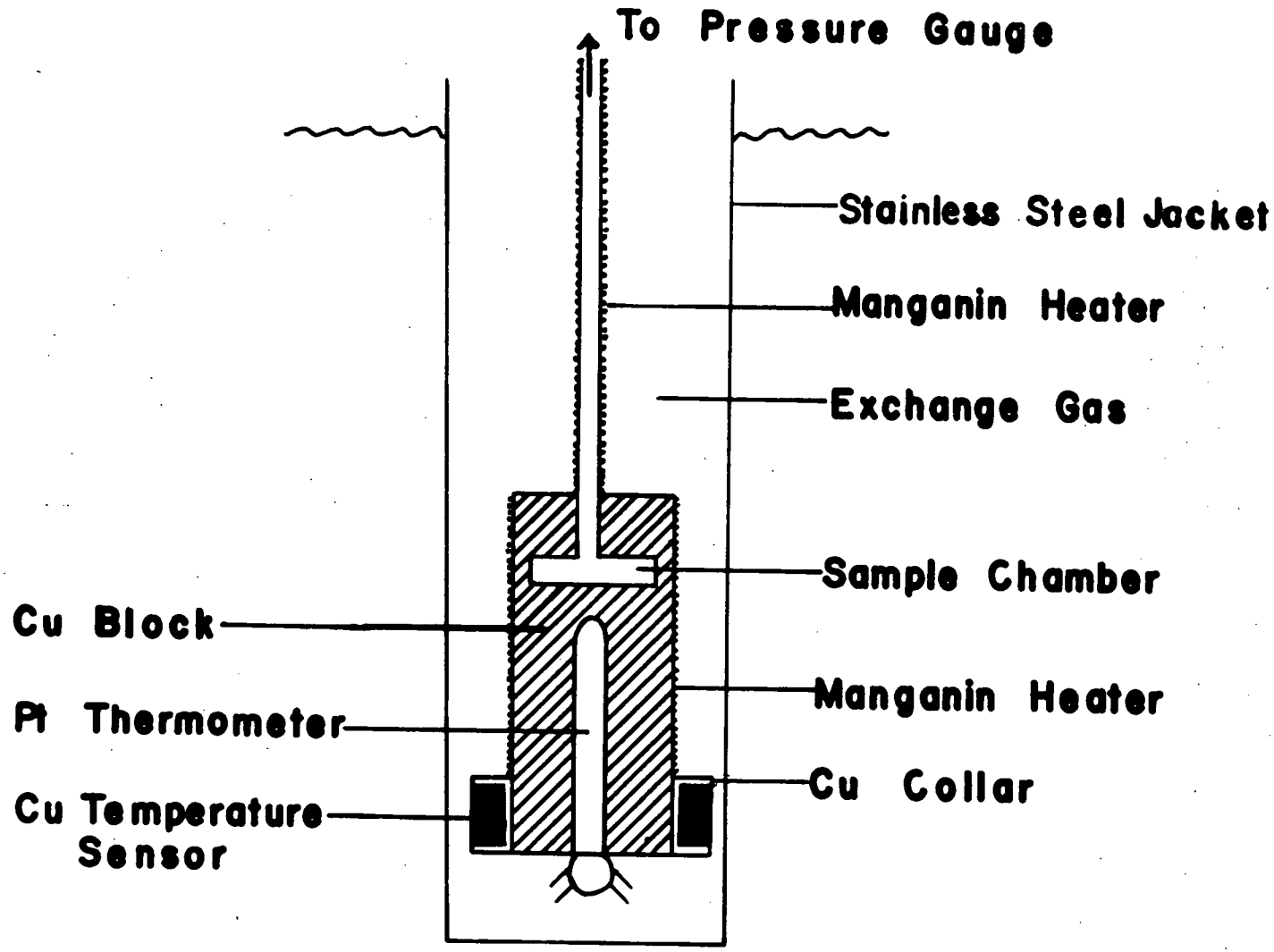

Figure 1: A sketch of the apparatus used for this experiment.

insure that the thermometer and Cu block were at the same temperature, the thermometer leads were thermally anchored to the Cu block.

A single-potentiometer technique was used to measure thermometer resistance and hence the sample temperature. Two of the leads were connected to a DC constant current source of 2 mA. The remaining two leads were run to a Leeds and Northrup K-5 potentiometer to measure the potential drop across the thermometer. To account for thermal emfs along the thermometer leads, all resistance measurements were repeated with the direction of the thermometer current reversed. Although the sensitivity of the measurements using this technique is approximately 0.5 mK, the estimated accuracy is $\pm$ 3 mK.

This is due primarily to the time factor involved in making each measurement. That is, during the course of a single measurement, the thermal emfs (as well as the sample temperature) can change slightly. These effects combined with the uncertainties in the thermometer calibration ($\pm$ 1 mK) give the estimated accuracy of temperature measurement, $\pm$ 3 mK.

2. Pressure Measurement

The sublimation and vapor pressures of Ar^{36} extend over several orders of magnitude for the temperature range used in this experiment. For this reason it was necessary to use two techniques covering two pressure ranges to measure pressure.

For pressures above 1 Torr, a calibrated Bourdon gauge was used. The particular instrument was a Texas Instruments Model 142 quartz spiral Bourdon gauge. A single Bourdon tube, which covered pressures from 0-1000 Torr, was sufficient for this experiment. For our Bourdon gauge, a photocell detector is used to detect the deflection of the Bourdon

tube by locating a beam of light reflected from a mirror attached to the Bourdon Tube. A counter which divides the full scale deflection into 300,000 counts is attached to the photocell detector. For a Bourdon tube with a pressure range of 1000 Torr then, the corresponding sensitivity of the gauge is about 3 microns.

A mercury manometer read with a Wild cathetometer was used to calibrate the Bourdon gauge. With the cathetometer, the mercury level in the manometer could be measured to $\pm$ 0.02 mm. Corrections were applied to these readings to account for the capillary depression of the mercury meniscus.[26] Corrections were also made for the thermal expansion of mercury (readings were corrected to the 0° C density of mercury) and for the local deviation from the standard gravitational acceleration (the standard value is g = 980.350 cm/sec^2, while at Michigan State University g = 980.665 cm/sec^2). The correction for the thermal expansion of mercury was the largest correction ($\lesssim$ 0.5%) but was nevertheless an accurate enough correction so as to not introduce any new errors. No errors were introduced by the gravitational correction since it, too, is known to a high degree of precision. The correction for the depression of the mercury meniscus was a small correction ($\lesssim$ 0.06 Torr) but was also the most uncertain. From the tables in Reference 26 it was clear that we could expect as much as a 15% error in the meniscus correction. That is, an additional error of $\pm$ 0.01 Torr is introduced by the meniscus depression effect. As judged by our calibration curve for the Bourdon gauge, the accuracy of our pressure measurements could be given as $\pm$ 0.03 Torr. This accuracy is consistent with the above mentioned uncertainty in the meniscus correction combined with the errors associated with the cathetometer readings.

To measure pressures below 1 Torr, a Consolidated Vacuum Corporation Type GM-100-A McLeod gauge was used. A liquid nitrogen cold trap separated the McLeod gauge from the sample chamber and thus prevented any mercury contamination of the sample. Because of this cold trap, however, it was necessary to correct the McLeod gauge readings for mercury streaming.[27] Mercury vapor will condense in the cold trap; therefore, there will be a flow of mercury vapor from the McLeod gauge to the cold trap which will then result in a reduced pressure in the McLeod gauge. Data and equations given in Reference 27 were used to make this correction, which was always less than 10% of the McLeod gauge reading.

It was also necessary to correct for the effects of thermomolecular flow.[28,29] When the mean free path of molecules in a tube (connecting two chambers at different temperatures) is comparable to or larger than the diameter of the tube, a pressure gradient is observed along the length of the tube. The pressure will be higher in the warmer chamber. As the mean free path becomes shorter, the pressure difference decreases and eventually goes to zero. This effect is most pronounced at low temperatures and low pressures. An empirical relation and experimental data given in Reference 28 were used to make this correction. At the lowest temperatures and pressures measured, this correction lowered the measured pressure by as much as a factor of 3. At temperatures near 50 K and pressures of 0.1-1.0 Torr, the correction was less than 2% of the measured pressure. The correction became negligible at higher temperatures and pressures.

3. Gas Sample Analysis

The gas sample was purchased from the Mound Laboratory and provided with a mass-spectrometer analysis. Amounts by mole fraction of each constituent were given as: Ar greater than 99.5%, N_2 less than 0.4%, H_2 and O_2 each less than 0.1%; of the Ar, more than 99.9% was Ar^{36}. Our own mass-spectrometer analysis, performed by the Chemistry Department at Michigan State University upon completion of the experiment, yielded by mole fraction the following impurity concentrations: N_2 less than 0.1%, O_2 less than 0.02%, and H_2 less than 0.0004%.

C. Results of the Experiment

The experimental sublimation- and vapor-pressure and temperature data are shown in Table 1 and plotted in Figure 2. At the lower temperatures, say below 35 K, the observed pressures begin to level off and the scatter in the data increases. The leveling off is due primarily to the presence of those volatile impurities which could not be removed from the sample. Another limiting factor, and one which contributes to the scatter in the data, is that these pressures were the lowest which could be measured with our McLeod gauge.

In order to obtain a measure of the amount of scatter in the data shown in Table 1, we used a truncated form of Equation 16:

$$\ell n(PT^{1/2}) = a/T + b \ , \qquad (17)$$

where the parameters a and b are the same as those defined in Equations 14 and 15, respectively. We first fit the data by the method of least squares to Equation 17 over two temperature ranges in the solid. The calculated coefficients are a = -988.088, b = 20.2338 for the temperature range 35.479 - 60.183 K, and a = -994.1123, b = 20.33541 for the temperature range 60.326 - 83.760 K. We used Equation 5 to represent

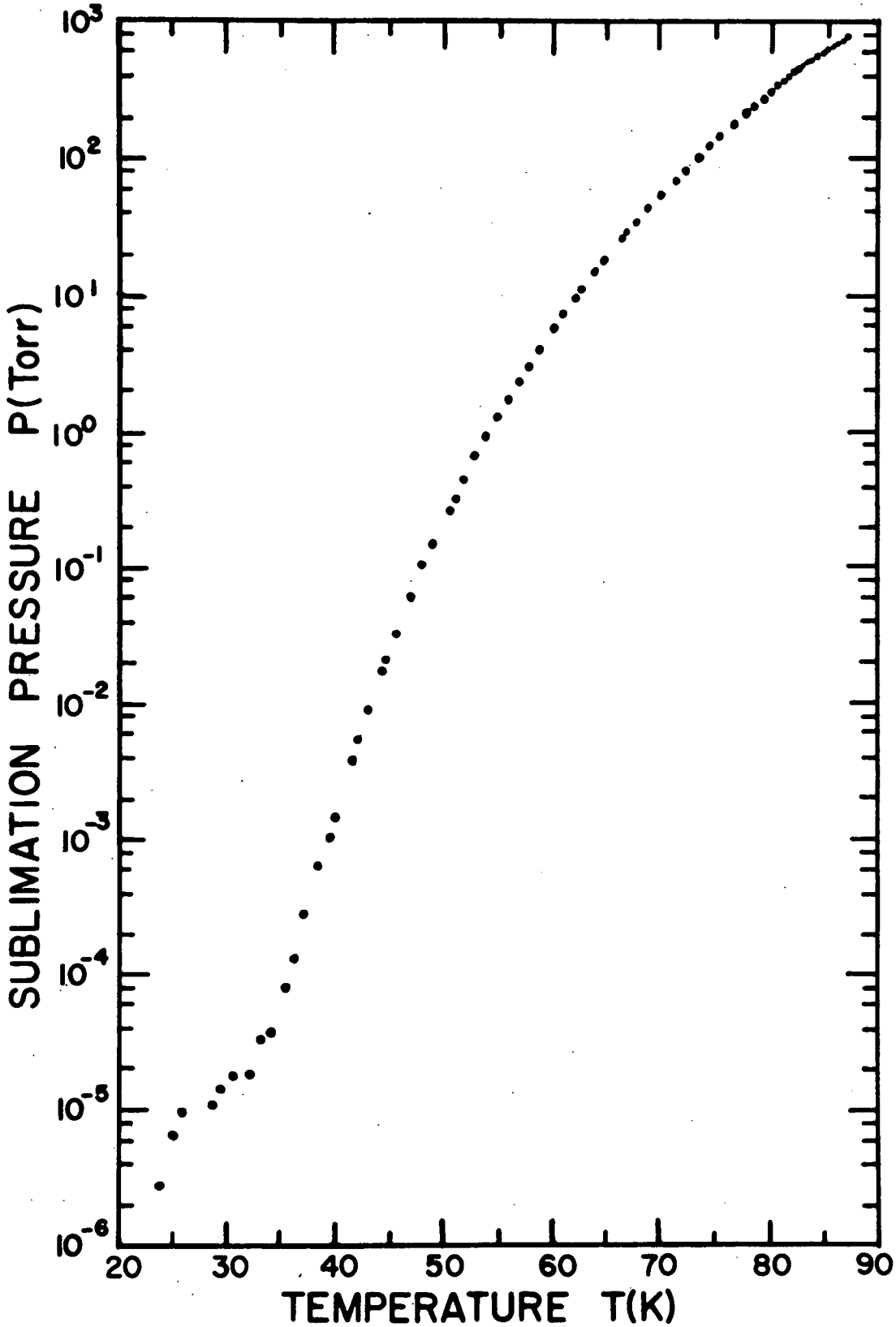

Figure 2: Sublimation pressure of Ar^{36} as a function of temperature.

TABLE 1

Experimental sublimation- and vapor-pressure and temperature data.

Temperature T (K)	Pressure P (Torr)	$P-P_{calc}$ (Torr)	$\frac{\lvert P-P_{calc}\rvert}{P}$
23.752	2.8×10^{-6}		
24.768	6.5×10^{-6}		
25.898	9.9×10^{-6}		
28.576	1.1×10^{-5}		
29.324	1.4×10^{-5}	$+ 1.4 \times 10^{-5}$	1.00
30.637	1.8×10^{-5}	$+ 1.7 \times 10^{-5}$	0.94
32.121	1.8×10^{-5}	$+ 1.3 \times 10^{-5}$	0.72
33.305	3.4×10^{-5}	$+ 2.0 \times 10^{-5}$	0.59
33.968	3.8×10^{-5}	$+ 1.4 \times 10^{-5}$	0.37
35.479	8.5×10^{-5}	$+ 0.2 \times 10^{-5}$	0.024
36.113	1.3×10^{-4}	$- 0.4 \times 10^{-5}$	0.031
36.945	2.9×10^{-4}	$+ 0.5 \times 10^{-4}$	0.172
38.152	6.3×10^{-4}	$+ 0.7 \times 10^{-4}$	0.111
39.276	1.02×10^{-3}	$- 0.14 \times 10^{-3}$	0.137
39.774	1.44×10^{-3}	$- 0.14 \times 10^{-3}$	0.097
41.430	3.85×10^{-3}	$- 0.33 \times 10^{-3}$	0.086
41.972	5.50×10^{-3}	$- 0.15 \times 10^{-3}$	0.027
42.951	9.26×10^{-3}	$- 0.29 \times 10^{-3}$	0.031
44.212	0.0172	- 0.0009	0.0523
44.493	0.0206	- 0.0002	0.0097
45.489	0.0327	- 0.0008	0.0245
46.933	0.0621	- 0.0022	0.0354
47.940	0.107	+ 0.008	0.0748
48.962	0.157	+ 0.006	0.0382
50.453	0.272	+ 0.002	0.0074
51.009	0.339	+ 0.007	0.0206
51.930	0.470	+ 0.006	0.0128
52.937	0.670	+ 0.010	0.0149
53.928	0.928	+ 0.007	0.0075
54.956	1.31	+ 0.03	0.0229
55.987	1.80	+ 0.02	0.0111
57.005	2.40	0.00	0.0000
57.935	3.17	+ 0.02	0.0063
58.889	4.08	- 0.04	0.0098
60.152	5.76	- 0.05	0.0087
60.183	5.80	- 0.04	0.0069
60.326	6.07	- 0.02	0.0033
61.118	7.47	- 0.02	0.0027
62.315	10.15	+ 0.01	0.0010
62.904	11.71	- 0.01	0.0009
64.139	15.76	+ 0.03	0.0019
64.887	18.70	0.00	0.0000
66.633	27.59	+ 0.02	0.0007
66.956	29.54	- 0.01	0.0003
67.927	36.26	- 0.02	0.0006
68.902	44.47	+ 0.16	0.0036
70.154	56.90	+ 0.09	0.0016

Table 1 (cont'd.)

Temperature T (K)	Pressure P (Torr)	$P-P_{calc}$ (Torr)	$\frac{\lvert P-P_{calc} \rvert}{P}$
71.471	73.29	+ 0.22	0.0030
72.356	86.07	- 0.02	0.00023
73.510	105.96	- 0.01	0.00009
74.681	130.30	+ 0.32	0.00246
75.557	150.62	- 0.16	0.00106
76.826	185.95	+ 0.12	0.00065
78.167	230.12	+ 0.10	0.00043
78.702	249.91	- 0.03	0.00012
79.612	286.81	- 0.30	0.00105
80.403	323.29	+ 0.25	0.00077
80.885	346.06	- 0.64	0.00185
81.439	375.37	- 0.28	0.00075
81.440	375.46	- 0.24	0.00064
81.878	399.37	- 0.61	0.00153
82.324	426.06	+ 0.05	0.00012
82.668	446.42	- 0.61	0.00137
83.241	484.02	+ 0.08	0.00017
83.639	510.82	- 0.20	0.00039
83.760	519.62	+ 0.13	0.00025
83.991	533.57	- 0.25	0.00047
84.045	537.13	0.00	0.00000
84.503	565.80	- 0.01	0.00002
85.047	601.60	+ 0.16	0.00027
85.492	632.02	+ 0.13	0.00021
85.998	668.16	+ 0.20	0.00030
86.482	704.22	+ 0.25	0.00036
87.031	746.65	+ 0.01	0.00001
87.244	763.73	0.00	0.00000
87.316	769.43	- 0.15	0.00019
87.375	774.06	- 0.33	0.00043

the data in the liquid range 83.991 - 87.375 K with calculated parameters A = -806.7794 and B = 15.88561. The third and fourth columns of Table 1 are based on these parameters applied to the appropriate temperature ranges. Notice that the calculation of pressure, with parameters a and b for the lowest temperature range, has been extended to 29.324 K on Table 1. This illustrates that the sublimation pressures begin to level off at the lower temperatures. For the most part the deviations of the actual pressures from the corresponding equations is what one would expect with scatter of $\pm$ 3 mK and $\pm$ 0.03 Torr.

Figure 3 is a plot of $\ell n(PT^{1/2})$ versus 1/T for data ranging from T = 68.902 K, P = 44.47 Torr to T = 83.639 K, P = 510.82 Torr. The straight line is the least squares fit, of the data shown, to Equation 17 with calculated parameters a = -992.9865 and b = 20.31851. A measure of the "goodness of fit" of Equation 17 to the data, is the average fractional deviation $|\Delta P/P|_{ave} \equiv |(P_{exp} - P_{calc})/P_{exp}|_{ave}$. For the set of points in Figure 3, $|\Delta P/P|_{ave} = 0.00087$, which is too small to be observed in the figure.

1. Discussion of Equation 16

Sublimation-pressure data can be used to determine several properties of Ar^{36} by comparison with theory. We did this by fitting P(T) data of Table 1 to the theoretically derived Equation 16. Further discussion of this equation is now in order to make clear how this was done and what it means.

The second term in Equation 16 expresses the effect of vacancy formation on vapor pressure. It can be written as $\exp(-g_s/k_BT) = \exp(s/k_B)\exp(-h/k_BT)$, where s and h are, respectively, the entropy and enthalpy of mono-vacancy formation. This term is equal to the fractional

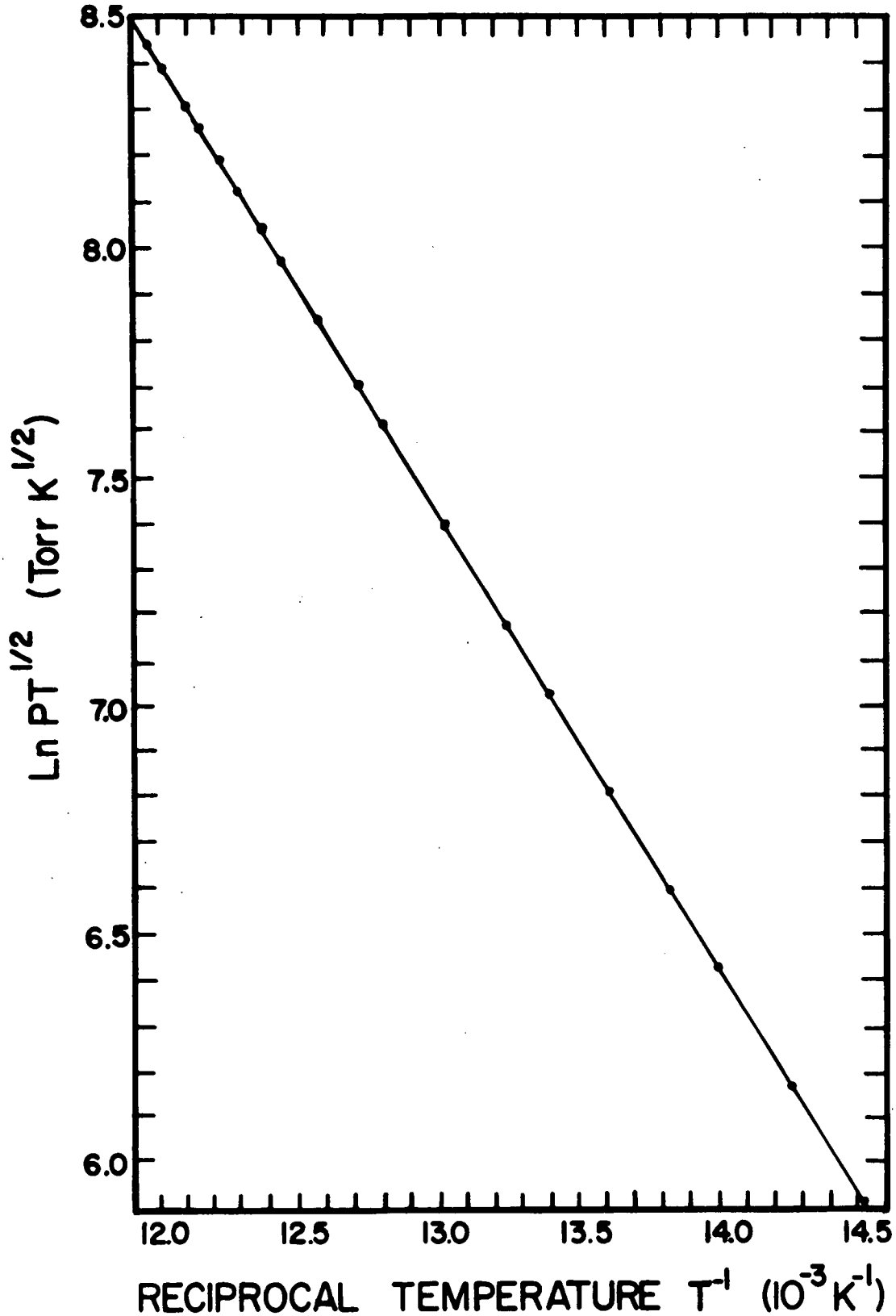

Figure 3: Plot of $\ell n(PT^{1/2})$ versus 1/T for data ranging from T = 68.902 K, P = 44.47 Torr to T = 83.639 K, P = 510.82 Torr.

vacancy concentration. We take the value of s/k_B for Ar^{36} to be that suggested by other workers[30] for normal argon, $s/k_B \simeq 2.0$, since no value for the isotope is available. A suitable value for the parameter h/k_B is then determined from measurements[31] which give the vacancy concentration of normal argon at the triple-point as $\exp(-g_s/k_BT_{tr}) \lesssim 0.13\%$. This gives $h/k_B \gtrsim 724.57$ K. The vacancy formation term, as a function of temperature, is at most then $\exp(-g_s/k_BT) = \exp(2)\exp(-724.57/T)$. This is the form used for our analysis; some typical values are given in Table 2. For temperatures near the triple point, 80.403 - 83.760 K, one effect of including this vacancy correction term is to decrease the parameter a of Equation 16 by 0.079%. This effect becomes smaller at lower temperatures and in particular, for the temperature range 58.889 - 66.633 K, is only 0.005%.

A somewhat larger effect is found in the third term of Equation 16, $-P(v_c - \mathcal{B})/RT$. This term combines the effects of finite crystal volume and gas imperfection. Values for the molar volume, v_c, are obtained from Dobbs and Jones.[32] The second virial coefficient, $\mathcal{B}$, is calculated according to Hirschfelder, Curtiss, and Byrd.[33] Some representative magnitudes of v_c, $\mathcal{B}$, and $-P(v_c - \mathcal{B})/RT$ are given in Table 2. In the temperature range 80.403 - 83.760 K, the inclusion of the finite crystal volume-gas imperfection term increases the parameter a of Equation 16 by 1.61%. At the lower temperatures, 58.889 - 66.633 K, the effect on a due to this term is reduced to 0.98%.

The 4th and 5th terms of Equation 16, $-(3/40)(\Theta_D/T)^2$ and $(1/2240)(\Theta_D/T)^4$, respectively, are the leading terms of the infinite series contained in Equation 13. To estimate these terms we used for the Debye temperature of Ar^{36}, $\Theta_D{}^{36} = 88.02$ K. This Debye temperature

TABLE 2

Typical values of various terms which appear in Equation 16.

Temperature T(K)	Vacancy correction[a,b] $\exp(-g_s/k_BT)$	Crystal molar volume[c] v_c (cm^3/mole)	Second virial coefficient[d] $-B$ (cm^3/mole)	Gas imperfection-finite volume correction $P(v_c - B)/RT$	Quantum-mechanical corrections $(3/40)(\Theta_D/T)^2$	$(1/2240)(\Theta_D/T)^4$
58.889	3.4×10^{-5}	23.59	451.37	5.3×10^{-4}	0.168	2.2×10^{-3}
62.904	7.4×10^{-5}	23.73	398.14	1.3×10^{-3}	0.147	1.7×10^{-3}
68.902	2.0×10^{-4}	23.96	335.30	3.7×10^{-3}	0.122	1.2×10^{-3}
73.510	3.9×10^{-4}	24.15	297.41	7.4×10^{-3}	0.108	9.2×10^{-4}
78.702	7.4×10^{-4}	24.36	262.79	0.0146	0.0938	7.0×10^{-4}
80.403	9.0×10^{-4}	24.44	253.48	0.0179	0.0899	6.4×10^{-4}
83.639	1.3×10^{-3}	24.57	235.77	0.0255	0.0831	5.5×10^{-4}

[a]Reference 30

[b]Reference 31

[c]Reference 32

[d]Reference 33

for Ar^{36} was calculated from that obtained by Morrison and co-workers[34] for Ar^N, $\Theta_D{}^N = 83.5$ K, assuming that Θ_D varies inversely as the square root of the mass. Values for the fourth and fifth terms of Equation 16 at various temperatures are given in Table 2. Their effects on the parameter a of Equation 16 are as follows: For the temperature range 80.403 - 83.760 K, $-(3/40)(\Theta_D/T)^2$ decreases a by 1.40% and $(1/2240)(\Theta_D/T)^4$ increases a by 0.027%. For the temperature range 58.889 - 66.633 K, $-(3/40)(\Theta_D/T)^2$ decreases a by 1.75% and $(1/2240)(\Theta_D/T)^4$ increases a by 0.064%. For intermediate temperatures these effects change monotonically.

The next higher order term in the infinite series in Equation 13 can be approximated as $(-1/180740)(\Theta_D/T)^6$. For temperatures greater than 58 K, its magnitude is less than 2% of the term in T^{-4}, and is therefore negligible.

2. Obtaining Thermodynamic Properties From the Data

We fit P(T) data of Table 1 to Equation 16 by the method of least squares in the following manner: Beginning at T = 58.889 K, P = 4.08 Torr, the first 10 points in order of increasing temperature and pressure are fit to Equation 16. Then the first point is dropped, the 11th point is added and another 10-point fit is made. This procedure is repeated until the last data point to be used, T = 83.991 K, P = 533.57 Torr, is included in the fit. In all, 25 intervals were fit to the data. For each interval of fit, the average of the inverse temperature, $\langle T^{-1}\rangle$, is calculated. The temperature corresponding to that average, $\langle T^{-1}\rangle^{-1}$, is used to obtain the temperature dependence of the parameters a and b for that interval; these values for each data interval are shown in the first column of Table 3.

TABLE 3

The static lattice energy, E_o, and geometric mean of the lattice vibrational spectrum, ω_g, calculated from our data using Equation 16, are shown in the second and fourth columns, respectively. The third column shows the values of the heat of sublimation calculated from our data using Equation 5.

Temperature T(K)	Static lattice energy $-E_o$(cal/mole)	Heat of sublimation L(cal/mole)	Geometric mean frequency $\omega_g(10^{12}\ sec^{-1})$
62.068	2022.05	1923.63	7.681
62.866	2018.64	1919.80	7.610
63.627	2014.79	1915.55	7.533
64.490	2011.89	1912.18	7.478
65.470	2009.94	1909.63	7.440
66.502	2007.77	1906.80	7.400
67.502	2006.00	1904.32	7.367
68.563	2003.08	1900.61	7.314
69.614	2003.05	1899.76	7.313
70.685	1999.69	1895.51	7.254
71.694	1998.21	1893.06	7.229
72.812	1995.18	1888.94	7.179
73.896	1991.60	1884.07	7.121
74.978	1990.00	1881.15	7.095
76.014	1988.55	1878.32	7.072
76.966	1987.40	1875.66	7.054
77.891	1984.36	1871.11	7.008
78.703	1981.45	1866.66	6.965
79.438	1981.45	1865.20	6.964
80.131	1977.64	1860.35	6.909
80.726	1975.36	1857.26	6.876
81.237	1976.33	1857.33	6.890
81.735	1975.75	1856.15	6.882
82.153	1974.80	1854.48	6.869
82.513	1970.31	1849.12	6.805

In the manner just described we obtain, as functions of temperature, the static lattice energy, $E_o = a\,R$, and the geometric mean frequency, $\omega_g = [(2\pi/m)k_B^{1/3}]^{1/2} \exp(b/3)$. The first two columns of Table 3 show the values our analysis gives for T and E_o, respectively. Values obtained for ω_g are shown in the last column of Table 3.

Sublimation-pressure data can also be used to obtain the temperature dependence of the heat of sublimation L. To do this, the same P(T) data used to obtain E_o and ω_g are fit to Equation 5 over successive temperature intervals in the manner described above. Values for L resulting from this analysis are shown in the third column of Table 3.

The lattice vibrational energy, E_{vib}, can now be calculated according to the thermodynamic relation,

$$L = U_g - U_c + P(v_g - v_c) \ . \tag{18}$$

In this equation U_g and U_c are, respectively, the internal energies of the gas and crystal, and v_g and v_c are the molar volumes discussed previously. Now U_c can be expressed as, $U_c = E_o + E_{vib}$, which leads to:

$$E_{vib} = -E_o - L + P(v_g - v_c) + U_g \ . \tag{19}$$

To order of the second virial coefficient, Equation 19 can be rewritten as:

$$E_{vib} = -E_o - L - P(v_c - B) + (5/2)RT - (RT^2/v_g)(dB/dT) \ . \tag{20}$$

Values for B are the same as those used in the calculations of E_o and L. The results of these calculations for E_{vib} are shown in the second column of Table 4.

D. Discussion

In Table 3 the static lattice energy, $E_o(T)$, derived from our data, appears as an increasing function of temperature. Qualitatively,

TABLE 4

Lattice vibrational energies calculated from Equation 20 are shown in the second column. Theoretically predicted values from Equation 22 are shown in the third column.

Temperature T(K)	Lattice Vibrational Energy (experiment) E_{vib}(cal/mole)	(Debye theory) E_{vib}(cal/mole)
62.068	406.46	406.37
62.866	410.78	410.66
63.627	414.89	414.81
64.490	419.56	419.51
65.470	424.91	424.86
66.502	430.54	430.48
67.502	436.05	435.94
68.563	441.89	441.78
69.614	447.68	447.58
70.685	453.59	453.50
71.694	459.24	459.07
72.812	465.46	465.24
73.896	471.65	471.26
74.978	477.80	477.30
76.014	483.72	483.09
76.966	489.34	488.40
77.891	494.76	493.57
78.703	499.68	498.10
79.438	504.13	502.21
80.131	507.95	506.09
80.726	511.10	509.44
81.237	513.98	512.33
81.735	516.48	515.14
82.153	518.77	517.50
82.513	520.98	519.53

one expects this behavior since the crystal expands with increasing temperature. However, a quantitative comparison between the $E_o(T)$ values for Ar^{36}, in Table 3, and the theoretical $E_o(T)$ presents numerous difficulties. In principle one could calculate $E_o(T)$, in the effective two-body approximation, from the Lennard-Jones 6-12 potential and lattice parameter data, $a_o(T)$, for Ar^{36}. However, $a_o(T)$ for Ar^{36} has apparently not yet been determined so that one is forced to use $a_o(T)$ obtained from measurements on Ar^N. If this is done and a lattice sum calculation for an fcc lattice taken over all neighbors is made, the general result for $E_o(T)$ is given, for example in Kittel[35] as

$$E_o(T) = 2\varepsilon[12.131(\sigma\sqrt{2}/a_o(T))^{12} - 14.454(\sigma\sqrt{2}/a_o(T))^6] \ . \qquad (21)$$

Using lattice parameter data as given by Dobbs and Jones[32] and energy and distance potential parameters, respectively as $\varepsilon/k_B = 119.4$ K and $\sigma = 3.40$ Å, obtained by Zucker,[36] we find the resulting $E_o(T)$ to be higher than our experimental values by about 30 cal/mole. That is, our data show that the Ar^{36} solid is more tightly bound than predicted by this theory.

There are two principal sources of this disagreement. The first is simply that $a_o(T)$ for Ar^{36} is different from $a_o(T)$ for Ar^N. However, since $a_o(T)$ for Ar^{36} is expected to be larger than that for Ar^N, making this correction would still further increase the theoretical $E_o(T)$. As will be seen later though, estimates of this increase are small, less than 2 cal/mole. We believe that the main source of disagreement between theory and experiment is due to the effects of anharmonicity on the interatomic potential and therefore also on the lattice dynamics for the system.

It is interesting to note that if one mistakenly excludes the terms, $-(3/40)(\Theta_D/T)^2$ and $(1/2240)(\Theta_D/T)^4$, from Equation 16 and makes the empirical fit to the data with the equation truncated in this way, then the resultant values of $E_o(T)$ coincidentally agree remarkably well with the effective two-body theory. It is also interesting to note that excluding the term $-P(v_c - \mathcal{B})/RT$ from Equation 16 significantly alters the behavior of $E_o(T)$. Instead of increasing monotonically with T, $E_o(T)$ reaches a maximum at T = 75 K and thereafter is a decreasing function of T.

1. Behavior of Lattice Vibrational Energy

The lattice vibrational energy, in the Debye theory, is given by[23]:

$$E_{vib} = (9/8)R\Theta_D + 3RT\,\mathcal{D}(\Theta_D/T) \ , \tag{22}$$

where

$$\mathcal{D}(y) = (3/y^3)\int_0^y dx\, x^3\,(e^x - 1)^{-1}.$$

Values for E_{vib}, based on this theory and using $\Theta_D{}^{36}$ = 88.02 K, are shown in the third column of Table 4. The agreement with the experimental results in the second column is quite good.

2. Comparing Properties of Ar^{36} and Ar^N

We compared sublimation-pressure data shown in Table 1 for Ar^{36} with that given in Reference 1 for Ar^N and found the sublimation pressure of Ar^{36} to be consistently higher than that of Ar^N. This difference in sublimation pressure is small, ranging from about 1.4% at T = 62 K to approximately 0.6% at T = 83 K.

In Table 5 we compare P(T) data of Ar^{36} with that of Ar^N in the form $P^{36} - P^N$. For temperatures in the range 62-75 K we used the P^N data given in Reference 1. In the temperature range 75-84 K we used

TABLE 5

Comparison of sublimation pressures of Ar^{36} and Ar^{N}. Data for Ar^{N} in the temperature range 62.315-74.681 K are taken from Reference 1. For the temperature range 75.557-84.503 K, the unpublished data on Ar^{N} of Christen and Opsal[37] are used.

Temperature T(K)	Pressure difference $P^{36}-P^{N}$ (Torr)	Present work $10^2(P^{36}-P^{N})/P^{N}$	Data of Reference 4 $10^2(P^{36}-P^{N})/P^{N}$
62.315	0.14	1.399	1.466
62.904	0.17	1.473	1.434
64.139	0.22	1.416	1.373
64.887	0.23	1.245	1.323
66.633	0.35	1.285	1.255
66.956	0.33	1.130	1.240
67.927	0.37	1.031	1.207
68.902	0.64	1.460	1.167
70.154	0.71	1.264	1.121
71.471	1.01	1.397	1.078
72.356	0.91	1.069	1.051
73.510	1.20	1.145	1.020
74.681	1.46	1.133	0.983
75.557	1.12	0.749	0.960
76.826	1.69	0.917	0.926
78.167	2.04	0.894	0.895
78.702	2.12	0.856	0.880
79.612	2.26	0.794	0.869
80.403	3.19	0.997	0.840
80.885	2.54	0.739	0.833
81.439	3.19	0.857	0.823
81.440	3.22	0.865	0.823
81.878	3.08	0.777	0.811
82.324	3.84	0.909	0.801
82.668	3.35	0.756	0.803
83.241	4.26	0.888	0.787
83.639	4.15	0.819	0.803
83.760	4.58	0.889	0.736
83.991	3.92	0.740	0.651
84.045	4.18	0.784	0.649
84.503	4.34	0.773	0.638

newer, improved, data taken independently on the same apparatus by Christen and Opsal.[37] It was found by these workers, in a reexamination of the Ar^N data of Reference 1, that in the range of 75-84 K the earlier data were about 0.3% (i.e. 0.5 to 1 Torr) too high due to uncontrolled temperature gradients in the Cu block. These temperature gradients were due to excessive heat input into the stainless-steel inlet tube. In the work of Christen and Opsal on Ar^N and in the present experiment, these temperature gradients and their effects were eliminated. Table 5 shows that P^{36} is still consistently higher than P^N; the improved data increase the difference at 83 K to 0.89%.

In an attempt to quantitatively explain this difference we fit the Ar^N data of Reference 1 to Equation 16 in the same manner as described for Ar^{36}. We obtained values for the geometric mean frequency, ω_g^N, of Ar^N which when multiplied by the ratio of the square roots of the masses, $\sqrt{40/36}$, averaged 0.5% higher than those shown in the fourth column of Table 3 for Ar^{36}. The significance of this small difference will be discussed below.

The values obtained for the static lattice energies of Ar^{36} and Ar^N are very close and one cannot say with any certainty just how much they do differ. Part of the difficulty is that the Ar^N data gave a comparatively irregular $E_o(T)$. We did, however, calculate the average difference $(E_o^{36} - E_o^N)_{ave}$, with the result $(E_o^{36} - E_o^N)_{ave}$ = 1.72 cal/mole. A rough approximation of this difference may be obtained from theory in the following way: The lattice sum calculations mentioned earlier predict for the $E_o(T)$ curve (of Ar^N) an average slope, $\Delta E_o/\Delta T$ = 2.10 cal/mole K, in the temperature range 62.068-82.315 K. For this same temperature range, the Debye theory gives the average

slope for the $E_{vib}(T)$ curve (of Ar^N), $\Delta E_{vib}/\Delta T = 5.57$ cal/mole K. Using these values then, an estimate of the dependence of static lattice energy on vibrational energy is found to be, $\Delta E_o/\Delta E_{vib} = 0.378$. The Debye theory further predicts the average difference in the vibrational energies of Ar^{36} and Ar^N for this temperature range to be, $(E^{36}_{vib} - E^{40}_{vib})_{ave} = 3.15$ cal/mole. Based on this discussion, we expect then an average difference in static lattice energies, $(E_o{}^{36} - E_o{}^{40})_{ave} =$ 1.19 cal/mole. We believe that this compares favorably with the observed value, considering all the approximations we have made.

Although our analysis of Ar^{36} and Ar^N data does not yield a conclusive explanation of the observed difference in sublimation pressure, we do believe it to be consistent with the following explanation: The zero-point vibrational energy, E_z, of a solid in the harmonic approximation is simply a sum over frequencies, $E_z = (1/2) \sum_{i=1}^{3N} \hbar\omega_i$. Since the interatomic potentials of Ar^{36} and Ar^N are the same, the effective force constants which determine the ω_i are the same. Thus, the zero-point vibrational energy of Ar^{36} should be higher than that of Ar^N by the mass dependent factor, $\sqrt{40/36}$. This means that Ar^{36} will be more anharmonic and therefore expand more with increasing temperature. That is, a higher zero-point energy implies a higher static lattice energy which in turn explains the higher sublimation pressure.

Of course, a point is reached where effects of anharmonicity in the interatomic potential become important. Qualitatively, from the shape of the interatomic potential, one expects the effective force constants, which determine the frequency spectrum, to decrease as anharmonicity increases. Our analysis reflects this in two ways. The

geometric mean frequency, ω_g, of Ar^{36} is a decreasing function of temperature as shown in Table 3. Secondly, the geometric mean of Ar^{36} averages about 0.5% less than $\sqrt{40/36}$ times that of Ar^N, that is $[(\omega_g^N\sqrt{40/36} - \omega_g^{36})/\omega_g^{36}]_{ave} = 0.5\%$. This also is consistent with Equation 16. For example at T = 72 K, the observed difference in sublimation pressure, $(P_{36} - P_{40})/P_{40} \simeq 1\%$. Assuming the static lattice energies to differ by $E_o^{36} - E_o^N = 1.2$ cal/mole, and assuming the difference in Debye temperatures, $\Theta_D^{36} - \Theta_D^N = 4.52$ K, the difference in geometric means must, according to Equation 16, compare as: $(\sqrt{40/36}\ \omega_g^N - \omega_g^{36})/\omega_g^{36} = 0.3\%$.

3. Comparison with the Work of Others

We compared our Ar^{36} data with that of Lee, Fuks, and Bigeleisen,[4] (LFB) and found our pressures to be lower than theirs for temperatures below 73.5 K and higher for temperatures above 73.5 K. These differences range from about -0.6 Torr at 63 K to + 2.2 Torr at 83 K. However, LFB's temperature measurements are based on the Ar^N vapor-pressure data of Flubacher, Leadbetter, and Morrison.[34] We therefore compared Ar^N data from Table 5 with that of Flubacher, Leadbetter, and Morrison and found the differences to be similar to those described above for Ar^{36}. We have found no explanations for these differences but have been able to conclude that the measurements made on Ar^N and Ar^{36} in our laboratory are consistent with one another.

To make a comparison of our sublimation-pressure data with an anharmonic crystal theory, we used Equation 12 and the Helmoltz free energy as calculated with a (13,6) potential by Klein and co-workers.[9,38] Our experimental pressures were higher than those predicted by Equation 12 throughout the temperature range 60-80 K.

These differences ranged from 3% at 60 K to 1.6% at 80 K.

In order to compare our vapor-pressure ratios with theory and other experiments, we made a least squares fit of the values shown in Table 5 to the equation:

$$\Delta P/P^N = c/T^2 + d/T \ , \tag{23}$$

where $\Delta P = P^{36} - P^N$. Equation 23 is an approximate form of Bigeleisen's[39] expression for the natural-logarithm isotope separation factor, α, given by $\ell n\alpha = [1 - P^{40}(v_c - B)/RT]\ \ell n(P^{36}/P^{40})$. The calculated coefficients are c = 57.87 and d = -0.014. Using these values for c and d in Equation 23 we find that our vapor-pressure ratios are about 4% higher than LFB's in the temperature range 62-83 K. In the fourth column of Table 5, we have included LFB's vapor-pressure ratios which have been interpolated to our temperatures.

We also calculated $\ell n\alpha$ and compared our results with the theoretical predictions of Klein _et al._,[9] as given on Figure 4 of Reference 9. In comparison with theirs, assuming a (13,6) potential, our values are lower by less than 1% at 60 K, essentially equal at 65 K, and about 3% higher at 80 K.

III. THE THEORETICAL CALCULATION OF KAPITZA RESISTANCE

A. The Model

The model we propose begins as follows: The copper has a thin deformed layer[21] (i.e., perhaps a region of high dislocation density[40,41]) beneath the surface, which will absorb the evanescent waves generated by a large fraction of the phonons incident from the liquid helium. These are phonons which normally, in the absence of such an absorbing layer, would be totally reflected. For the Cu-He^4 system under consideration this corresponds to phonons incident at angles greater than $\sim 6^o$ (i.e., the critical angle of reflection associated with transverse waves in the solid.) Since energy will be therefore dissipated in the deformed layer, there will naturally arise the question: What happens to the dissipated energy? While we cannot answer this completely, we can, however, make a plausible argument. If this energy goes into phonon modes, then the energy may be assumed, for the most part, to remain in the solid. That is, since the probability of reflection from the solid to liquid interface is quite high ($\gtrsim 0.99$), the scattering of phonons back into the liquid helium can be neglected.

As part of our model we consider the density of helium near the Cu-He^4 interface to increase as the copper surface is approached. In order to calculate this density profile as a function of distance from the interface, we proceed in the manner of Challis _et al._[15] We assume that the van der Waals force between a helium atom and the copper

substrate varies as d^{-4}, where d is the distance from the substrate. The potential energy of a single helium atom can then be written as $\Phi(d) = -\alpha d^{-3}$. For the constant α we take the value originally given by Schiff,[42] (which was used in Reference 15) $\alpha = 5.3 \times 10^{-37}$ erg cm^3. Other estimates of α, for metals, have been made by Sabisky and Anderson[43] using the Lifshitz theory of the van der Waals force. For a metal with a plasma frequency, $\omega_p = 10$ eV, (for Cu, $\omega_p \simeq 10$ eV) they obtain $\alpha = 2.14 \times 10^{-37}$ erg cm^3 for $d \leq 10$ Å. However, for distances as great as $d \simeq 20$ Å, the change in α is not more than 1%. The potential $\Phi(d) = -\alpha d^{-3}$ can therefore be used with α constant, since in our calculations d never exceeds 15 Å. At first it might appear that the large difference in the two values of the potential parameter might be important. As will be seen later, however, the effect on the density profile, with respect to our calculations, is not so important. Treating the helium as a continuum, we associate with a potential gradient, $\underset{\sim}{\nabla}\Phi$, a corresponding pressure gradient, $\underset{\sim}{\nabla}P$; for which

$$(\rho/m)\underset{\sim}{\nabla}\Phi = -\underset{\sim}{\nabla}P \ . \tag{24}$$

In Equation 24, ρ is the density of the helium as a function of distance from the copper substrate and m is the mass of a helium atom. Equation 24 is equivalent to the integral equation

$$(\alpha/m)d^{-3} = \int_{P(\infty)}^{P(d)} dP/\rho(P) \ . \tag{25}$$

In order to solve Equation 25 for P(d) and hence $\rho(d)$, we use experimental data[44-47] which give liquid and solid helium densities as a function of pressure extrapolated to 0 K. Our calculated density profile, using $\alpha = 5.3 \times 10^{-37}$ erg cm^3, has a discontinuity in ρ at $d \simeq 8$ Å which corresponds to the liquid-solid transition. For the potential parameter, $\alpha = 2.14 \times 10^{-37}$ erg cm^3, the liquid-solid

transition occurs at $d \simeq 6$ Å. Since the zero-point motion of the atoms is so large for helium, it is unlikely that the transition will be so well defined. In order to account for this and at the same time to consider that the potential parameter α may be too large, we have smoothed out the calculated density profile. The smoothed profile which we then use has the analytic form

$$\rho(d) = \rho_{He}(1 + a/x^b) \ , \tag{26}$$

where $a = 9.95$, $b = 1.79$, and ρ_{He} is density of bulk liquid helium. The density profile described by Equation 26 gives a value for $\rho(d)$ corresponding to the density of solid helium at $d \simeq 7$ Å; that is $\rho(7\ \text{Å}) = 0.189\ \text{gm/cm}^3$.

We should mention at this point that in our calculations we consider the effects of changing the density profile in a number of ways. Our first approach is to consider the density as a constant for distances, d, within 7 Å of the copper substrate. In this way we first see the effects of including transverse waves in the dense helium region. Next we consider cases in which the density attains a higher value, becoming constant at distances of 6, 5, and 4 Å from the substrate. Finally we consider the effects of actually changing the shape of the profile in the region where the density is increasing (for example; $7 \leq d \leq 15$ Å). We should like to point out now that the latter has only a slight effect on our calculated R_K values.

It is perhaps appropriate at this point to describe a portion of the calculation. In order to calculate the energy flux associated with the propagation of waves through a medium with a continuously varying density, we subdivide that medium into thin layers. The density at the midpoint of each layer is equal to the real density at that point

in the medium. We make the layers thin enough so that none ever satisfies the 1/4 wavelength condition for optimum transmission.[48]

B. Theory

We first consider the propagation of waves through a system of solid and liquid layers. In order to establish the conventions used in our calculations, we present a brief description of the elastic theory of solids and liquids. More mathematical details of the theory are given in Appendices A, B and C.

1. Elastic and Viscoelastic Materials

For an isotropic, elastic, solid[48] the stress-strain relations can be expressed in the simple form

$$T_{ij} = \mu[(\partial S_i/\partial x_j) + (\partial S_j/\partial x_i)] + \lambda\delta_{ij}(\partial S_k/\partial x_k) \ . \tag{27}$$

In Equation 27, T_{ij} is the stress tensor, λ and μ are the Lamé parameters, S_i is the displacement field, $(1/2)[(\partial S_i/\partial x_j) + (\partial S_j/\partial x_i)]$ is the strain tensor, and δ_{ij} is the unit tensor. Summation is implied over repeated indices. The equations of motion for the system are given by

$$\rho(\partial^2 S_i/\partial t^2) = \partial T_{ij}/\partial x_j \ , \tag{28}$$

where ρ is the density of the material. Because isotropy is assumed, a solution of Equation 28 can be decomposed into two fields; a curl-free field plus a divergence-free field. Therefore, we can choose to work with a velocity field, $\vec{v}$ (with cartesian components defined by $v_i = \partial S_i/\partial t$) which can be obtained from a scalar potential, ϕ, and a vector potential, $\vec{\psi}$.

These potentials satisfy wave equations

$$\rho(\partial^2\phi/\partial t^2) = (\lambda + 2\mu)\nabla^2\phi \ , \tag{29}$$

$$\rho(\partial^2\vec{\psi}/\partial t^2) = \mu\nabla^2\vec{\psi} \ , \tag{30}$$

which have plane-wave solutions. For waves propagating in the xz-plane

then, these potentials are given explicitly by:

$\phi = [A \exp(i\vec{k}\cdot\vec{r}) + B \exp(-i\vec{k}\cdot\vec{r})]\exp(-i\omega t)$ and $\vec{\psi} = (0,\psi,0)$ where

$\psi = [C \exp(i\vec{\kappa}\cdot\vec{r}) + D \exp(-i\vec{\kappa}\cdot\vec{r})]\exp(-i\omega t)$. The corresponding total velocity field is given by, $\vec{v} = \vec{v}_\ell + \vec{v}_t$, where $\vec{v}_\ell = \underset{\sim}{\nabla}\phi$, $v_t = \underset{\sim}{\nabla} \times \vec{\psi}$, and the subscripts ℓ and t refer to longitudinal and transverse waves, respectively.

For the case of a non-viscous fluid, Equations 27, 28 and 29 apply with the shear modulus, μ, set equal to zero. When viscosity is present[49] the shear modulus is pure imaginary, $\mu = -i\omega\eta$ and Equations 27, 28, 29 and 30 are used. η is the coefficient of viscosity of the fluid. Finally when the material is a visco-elastic solid,[49] the elastic constants λ and μ are replaced by $\lambda - i\omega[\xi-(2/3)\eta]$ and $\mu-i\omega\eta$, respectively, where η and ξ are coefficients of viscosity. Equations 27, 28, 29 and 30 are used for this case also.

The cases for which the elastic constants are complex result in plane waves which are attenuated, that is the wave vectors are complex. We therefore consider the effects of phonon attenuation in our calculations by using complex wave vectors in the absorbing material. For example, for a longitudinal wave vector, k, we then have

$$k = (\omega/c_\ell)(1 + iV_\ell) \ , \tag{31}$$

where V_ℓ and c_ℓ are, respectively, the loss factor and velocity for longitudinal waves. Similarly, for a transverse wave vector, κ, we have

$$\kappa = (\omega/c_t)(1 + iV_t) \ , \tag{32}$$

where V_t and c_t are, respectively, the loss factor and velocity for transverse waves. At this point we should mention that since the complex elastic constants are restricted to lie in the 4th quadrant of the complex plane,[49] the loss factors can only have values between 0 and 1 (i.e., $0 \leq V_{\ell,t} \leq 1$).

Restricting ourselves, once again, to waves propagating in the xz-plane, we consider the boundary conditions[49] (based on Equation 28) which are appropriate to the cases encountered in our calculations. For a non-viscous liquid-liquid interface, the conditions are that the normal components of the velocity field and stress tensor be continuous. Since we will always be dealing with plane boundaries in the xy-plane, this requires that T_{xz}, T_{zz}, and v_z be continuous. Continuity of T_{xz} is trivially satisfied since $\mu = 0$ on both sides of the interface. For a liquid-solid interface, we then have the same conditions (continuity of T_{xz}, T_{zz}, and v_z with $T_{xz} = 0$), however, all three must be used, since there are now three unknown wave amplitudes to determine. At a solid-solid interface, we must have continuity of T_{xz}, T_{zz}, v_x, and v_z, and there are (in this case) four unknown wave amplitudes to solve for.

In Figure 4, we have a diagram of a system of solid and liquid layers which is typical of those used in our calculations. The labeling of the x and z axes indicates the positive directions along those axes. The boundary of the semi-infinite solid is at $z = z_o \equiv 0$ and the semi-infinite liquid has its boundary at $z = z_n$. In between the semi-infinite solid and semi-infinite liquid is a system of n layers, some liquid and some solid. The subscripted variables, z_i, along the bottom of the figure, indicate the values of z which bound each layer. Also shown are the resulting waves which propagate through the layers when a wave is incident from the liquid at $z = z_n$. The solid layers support both longitudinal and transverse waves (indicated by k_i and κ_i, respectively), while in the liquid layers, there are only longitudinal waves (indicated by k_i). The angles shown from the normal (θ_i and γ_i)

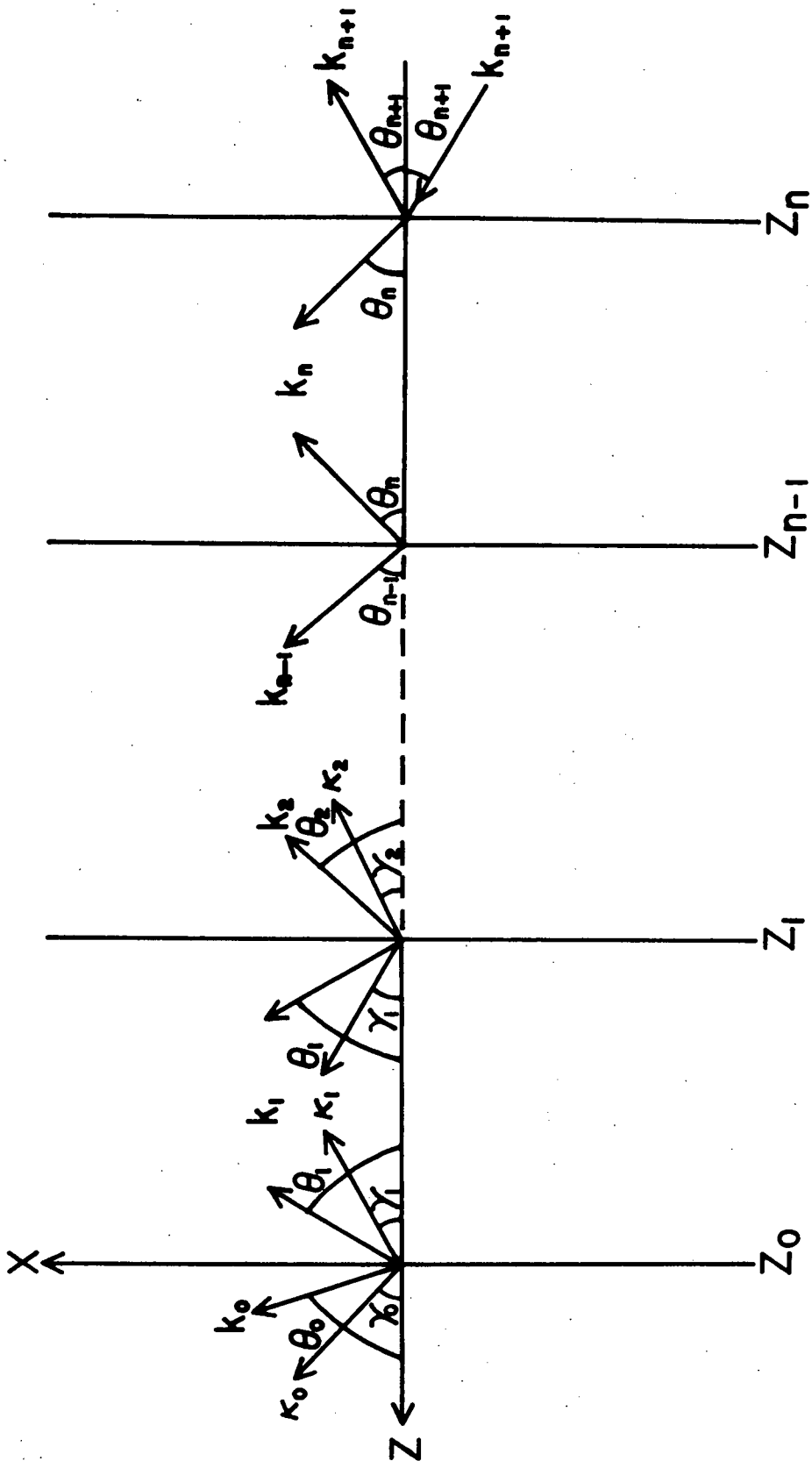

Figure 4: A system of solid and liquid layers typical of those used in the calculations.

correspond to real angles only when the corresponding wave vectors are real (no attenuation). When attenuation is present, the real angles have to be determined from the real parts of the wave vectors. The dashed line in the middle of the figure along the z-axis is used to imply the presence of the n-2 layers not shown.

To calculate the propagation of energy through the system of layers shown in Figure 4, we employ the method given in Reference 48. For the solid layers we relate the stress and velocity components of the mth layer to those in the (m-1)st layer by applying the boundary conditions appropriate at solid-solid interfaces. Since there are some differences between our results and those given in Reference 48, (most likely misprints) we show our results in Appendix C of this thesis. For the liquid layers, we use the concept of the input impedance of a layer as discussed in Reference 48. Results of these calculations are also shown in Appendix C. For the entire system of solid and liquid layers, we then calculate the transmitted wave amplitudes in the solid at $z = 0$ and the reflected wave amplitude in the liquid at $z = z_n$, for unit amplitude of the incident wave. Knowing these amplitudes we then calculate the energy transmission coefficient, TR, as a function of frequency, ω, and angle of incidence, $\theta \equiv \theta_{n+1}$. From Equations 27 and 28, it follows that the cartesian components of the energy flux, $\vec{P}$, at any point in the medium are given by [49]

$$P_i = (1/2)\ \mathrm{Re}(-T_{ij}v_j^*)\ , \tag{33}$$

and therefore the energy transmission coefficient, TR, is given by

$$\mathrm{TR} = [\mathrm{Re}(-T_{xz}v_x^*) + \mathrm{Re}(-T_{zz}v_z^*)]/\omega\rho_{n+1}\mathrm{Re}(k_z)_{n+1}\ . \tag{34}$$

Our reason for calculating TR at both ends of the system of layers is to provide a check on our calculations. That is, since energy must be

conserved, in the absence of attenuation, TR must be the same at both ends of the layered system. In our subsequent calculations, conservation of energy was always satisfied where required.

2. The Heat Flux and Kapitza Resistance

To calculate the Kapitza resistance, we proceed along the lines of the acoustic mismatch theories of Khalatnikov[12] and of Mazo and Onsager.[14] We quantize the incident energy flux, $P_z^{(inc)}$, according to $P_z^{(inc)} = (\hbar\omega/\Omega)c_{He}\cos\theta$. Ω is the volume, c_{He} is the sound velocity in bulk liquid helium, and ω is the angular frequency of the incident wave. The transmitted flux, P_z, is then given by $P_z = (\hbar\omega/\Omega)TR(\omega,\theta)c_{He}\cos\theta$. Assuming a Debye density of states for the incident phonons, we then calculate the total heat flux, W(T), as a function of temperature, T,

$$W(T) = (\hbar/4\pi^2 c_{He}^2) \int_0^\infty d\omega\ \omega^3\ n(\omega,T) \int_0^{\pi/2} d\theta\ TR(\omega,\theta)\ \sin\theta\ \cos\theta \quad . \qquad (35)$$

In Equation 35 $n(\omega,T)$ is the Bose-Einstein distribution function, $n(\omega,T) = [\exp(\hbar\omega/k_BT) - 1]^{-1}$, k_B is Boltzmann's constant, and $\hbar$ is Planck's constant divided by 2π. The Kapitza resistance is defined by $R_K^{-1} = dW/dT$, and using Equation 35 we then obtain

$$R_K^{-1} = (k_B/\hbar)^4(\hbar/4\pi^2c_{He}^2)T^3 \int_0^\infty dx\ x^4e^x(e^x - 1)^{-2} \int_0^{\pi/2} d\theta\ TR(k_BTx/\hbar,\theta)\sin\theta\cos\theta. \qquad (36)$$

Equation 36 is the expression we use to calculate R_K. In the next section we describe the numerical method used to obtain values for R_K as a function of temperature.

C. Numerical Method

In order to calculate R_K using Equation 36, we must evaluate the double integral

$$I(T) = \int_0^\infty dx\ x^4\ (e^x - 1)^{-2}\ g(k_BTx/\hbar)\ . \qquad (37)$$

where

$$g(k_B Tx/\hbar) = \int_0^{\pi} d\theta \; TR(k_B Tx/\hbar, \theta) \sin\theta \cos\theta \; . \tag{38}$$

Remembering that $\omega = k_B Tx/\hbar$, we first form an array of points, $g(\omega_i)$, over a range of ω values suitable to the temperature range for which R_k is to be evaluated. To obtain the points in this array, we use an adaptive numerical integration scheme which varies the increment size, $\Delta\theta$, according to the amount of curvature in the integrand. We then evaluate $g(k_B Tx/\hbar)$ for arbitrary values of x and T by linearly interpolating between the appropriate points in the array $g(\omega_i)$. The same integration scheme is then employed to perform the integral over x in Equation 37 and thereby obtain I(T).

For temperatures $T \lesssim 1.0$ K, we expect better than 1% accuracy in our integrations. Above 1.0 K, the accuracy will decrease to perhaps as much as 5% at T = 2.0 K.

The computer program used to perform these integrations is shown in Appendix D.

D. Discussion

1. Effects Due to Phonon Attenuation

In Table 6 we show results of our initial calculations in which only the effects of phonon attenuation in the copper are included, i.e., impedance matching is omitted. A more complete tabulation of these results is given in Table F1. Only a single attenuation variable, V, is shown, since we have taken the loss factors, V_ℓ and V_t, [defined in Equations 31 and 32] as equal. That is, $V \equiv V_\ell = V_t$.

This is a reasonable choice for the following reason: In making these calculations we found that for a given transverse wave attenuation, V_t, the calculated R_K values were relatively insensitive to changes in

TABLE 6

Kapitza resistance, R_K, in the form $R_K T^3$, as a function of phonon attenuation in the copper.

Loss Factor V	Kapitza Resistance x (Temperature)^3 $R_K T^3$ ($cm^2\ K^4/W$)
0.0	1270
0.001	~540
0.002	501.9
0.01	401.8
0.02	334.3
0.06	201.4
0.10	145.0
0.12	127.2
0.15	107.6
0.20	85.8
0.25	71.5
0.30	61.4
0.40	48.1
0.50	39.6
0.70	29.7
1.0	22.0

the longitudinal wave attenuation, V_ℓ. Also, the relationship between V_ℓ and V_t is not yet well understood. Acoustic experiments[50] on water-stainless steel interfaces do, however, show V_ℓ and V_t to be the same order of magnitude (actually, $V_t \simeq 2V_\ell$) for ultrasonic frequencies up to about 100 MHz.

The loss factor, V, is further assumed to be independent of frequency and temperature. Under these assumptions, still neglecting impedance matching, $R_K T^3$ is independent of temperature. Effects of frequency dependence in V on R_K are discussed in Reference 17. For the density and sound velocities in copper we use; $\rho_{Cu} = 8.93$ gm/cm^3, $c_\ell = 5.0 \times 10^5$ cm/sec, and $c_t = 2.3 \times 10^5$ cm/sec. In the bulk liquid helium we use; $\rho_{He} = 0.145$ gm/cm^3 and $c_{He} = 2.38 \times 10^4$ cm/sec. We can use the results shown on Table 6 to determine the range of values of V which should be used for our subsequent calculations. The smallest values of V that give R_K values which agree with Kapitza resistance experiments at low temperatures, lie in the range 0.10-0.12. Anderson, Connolly, and Wheatley[51] measured Kapitza resistances and obtained: $R_K T^3 = 134$ cm^{2}K^4/W at T = 0.06 K and $R_K T^3 = 127$ cm^{2}K^4/W at T = 0.08 K. However, from R_K values measured by Zinov'eva[52] we find; $R_K T^3 \simeq 60$ cm^{2}K^4/W at T = 0.08 K and from Table 6 this corresponds to a loss factor $V \simeq 0.30$. At higher temperatures, somewhat higher attenuations are required to fit this theory to experiment. For our subsequent calculations then, we use values of V in the range V = 0.12-0.50.

2. Effects of Including Impedance Matching

We shall now discuss the results when the effects of impedance matching are included in the theory. In Figures 5 and 6 we show the

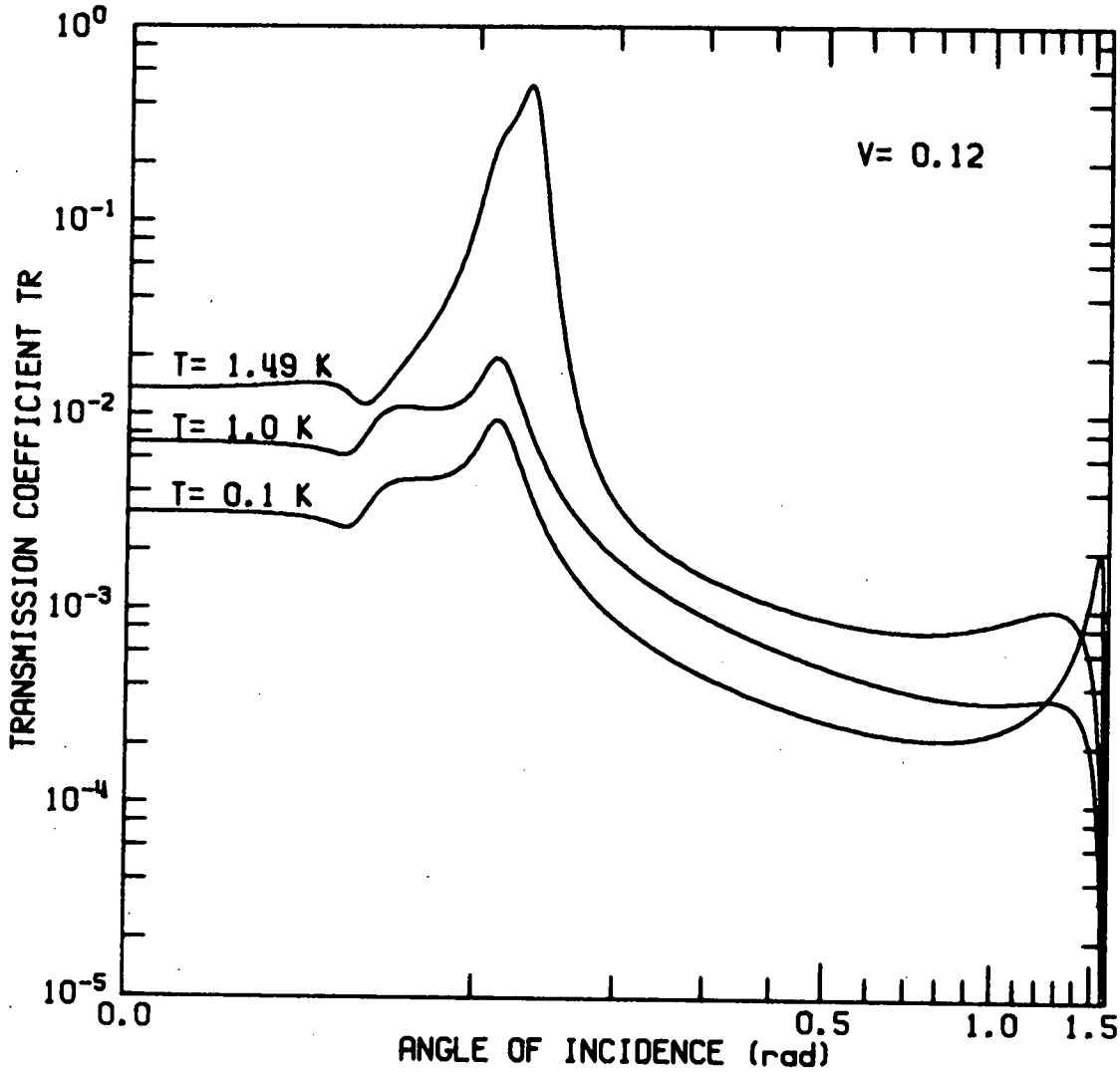

Figure 5: Calculated energy transmission coefficient, TR, at three frequencies as a function of angle of incidence. The frequencies are expressed in terms of temperatures defined by $\omega = 3.7 \times 10^{11} T$ (sec^{-1}). Both longitudinal and transverse waves are included in the first, most dense He layer.

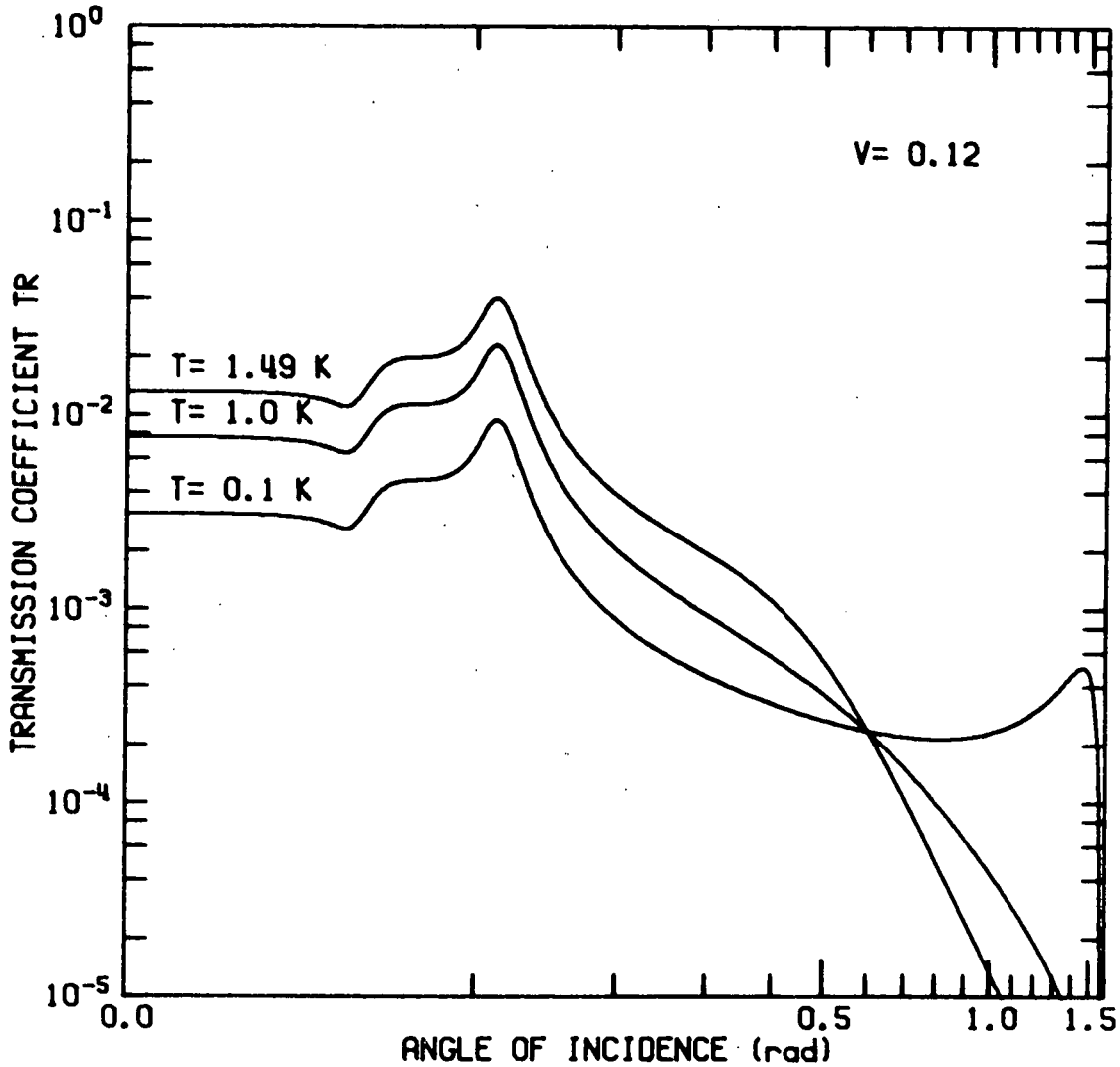

Figure 6: TR calculated at three frequencies. Only longitudinal waves are included in the first He layer.

calculated energy transmission coefficient, TR, at three frequencies. The frequencies are expressed in terms of temperatures for which $\omega^3\, n(\omega,T)$ is a maximum; i.e., $\omega = 3.7 \times 10^{11} T\ (\mathrm{sec}^{-1})$. The axis corresponding to the angle of incidence is expressed in radians and ranges from 0.0-1.6 rad. The point where all the curves in Figure 5 tend toward zero is $\pi/2$ rad = 90°. We have made this axis non-linear to bring out the structure in TR at small angles of incidence; that is, the axis is expanded for small angles. For the density profile we use Equation 26 and the parameters, a and b, as given below Equation 26. It is convenient to introduce a variable, F, which defines the maximum density, ρ_1, of the helium by: $\rho_1 = F\, \rho_{He}$. When the distance from the copper surface is such that the helium density is equal to ρ_1, the density is taken to be constant from that point to the surface. For the calculated curves in Figures 5 and 6, F = 1.3 and the corresponding distance over which the density is constant is 7 Å.

Since F = 1.3 corresponds to the lowest density for which He^4 is a solid, the effects of including transverse waves in the dense helium region should be considered for values of $F \geq 1.3$. For calculating the curves shown in Figure 5 then, transverse waves are included in the solid helium layer. For comparison, the curves shown in Figure 6 are calculated with the solid helium layer treated as a liquid in the sense that transverse waves are excluded.

The sound velocity in liquid helium, a linear function of density, is taken from the experimental work of Abraham and co-workers.[53] In the solid helium we use the sound velocity, c_ℓ, for longitudinal waves, also a linear function of density, as measured by Vignos and Fairbank.[54]

We then choose $c_t = (1/2)c_\ell$ as a suitable average for the sound velocity of transverse waves.

To illustrate more clearly the structure of the transmission coefficient, TR, as a function of angle of incidence, we show in Figure 7 TR calculated for a small attenuation, V = 0.01. The other parameters used for calculating the curves shown in Figure 7 are the same as those used for Figure 6 (i.e., only longitudinal waves are included in the first, most dense He layer). For the lowest frequency shown (corresponding to T = 0.1 K) the TR curve in Figure 7 is almost identical to the curve one would obtain if the impedance matching effects were neglected. That is, the impedance matching region has very little effect at this lowest frequency, since the wavelength in bulk He corresponding to T = 0.1 K ($\lambda \simeq 400$ Å) is much longer than the thickness of the impedance matching region ($d \simeq 15$ Å).

The first dip in this curve corresponds to the critical angle of incidence associated with longitudinal waves in the Cu; $\theta_{cr\ell} = \sin^{-1}(c_{He}/c_\ell) = 0.0475$ rad. When no absorption is present, longitudinal waves in the Cu, for angles of incidence beyond this critical angle, travel along the interface and are exponentially attenuated inward from the interface. This attenuation should not be confused with the attenuation resulting from absorption. When the attenuation of a wave is along the wavefront (that is, perpendicular to the direction of propagation) there is no absorption of energy. Energy absorption in a wave is present only when the wave has some attenuation along its direction of propagation. Waves which are attenuated laterally are called evanescent waves and in the absence of absorption carry energy only along the interface. That is, evanescent waves will

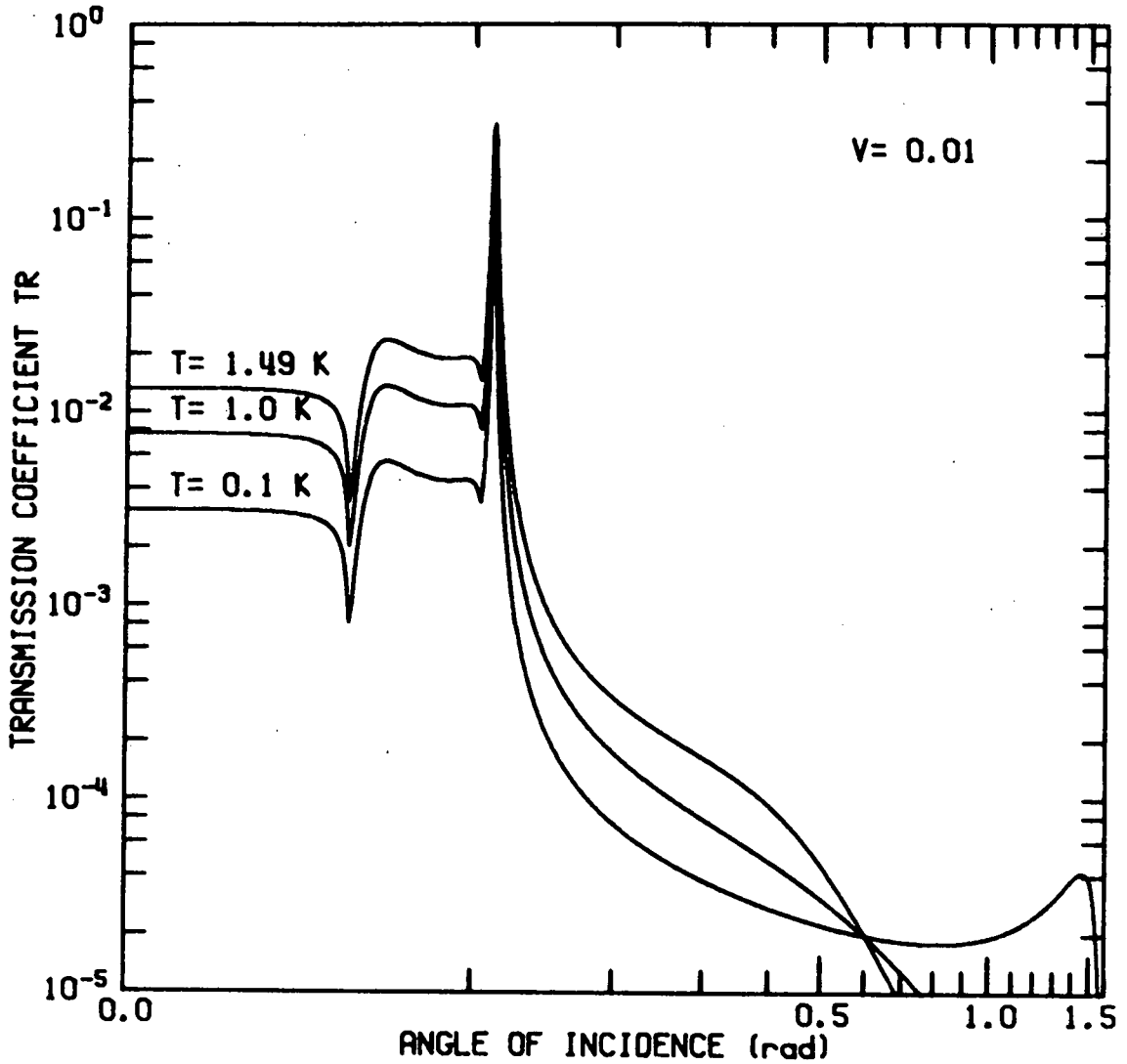

Figure 7: TR calculated at three frequencies. Only longitudinal waves are included in the first He layer.

give no contribution to the transmission of energy from the liquid to the solid. This is clear since k_z [= $(\omega/c_\ell)\cos\theta_\ell$] becomes pure imaginary when $\sin\theta_\ell$ [= $(c_\ell/c_{He})\sin\theta$] is greater than 1 and the energy flux through the interface is proportional to the real part of k_z. Including absorption in the solid (as we have done in Equations 31 and 32) results in k_z values which always have a real part; i.e., energy is transmitted through the interface for all angles of incidence.

The second dip in this curve corresponds to the critical angle of incidence associated with transverse waves in the Cu; $\theta_{crt} = \sin^{-1}(c_{He}/c_t) = 0.1035$ rad. The transverse waves are then also evanescent for angles of incidence greater than θ_{crt}. Just beyond the transverse critical angle is the Rayleigh peak at an angle of incidence called the Rayleigh angle; $\theta_R = 0.110$ for this Cu-He^4 system. For the small attenuation used in Figure 7 the peak is quite narrow and well defined. It corresponds to the angle of incidence for which the longitudinal and transverse evanescent waves are propagating in exactly the same direction. As V approaches zero the width of the Rayleigh peak approaches zero and its contribution to TR thus goes to zero. As V becomes larger (see Figure 6 for example) the Rayleigh peak broadens and much of the other structure also becomes less pronounced. There is an additional small peak for angles of incidence near $\pi/2$ (=90°). This peak represents the strong coupling of waves at grazing incidence from the liquid to the transverse waves in the solid. For the higher frequencies shown in Figure 7, this peak does not appear for reasons which will be explained later.

The effects of including transverse waves in the solid helium layer are quite evident when the curves in Figures 5 and 6 are compared.

Associated with the longitudinal waves in the first, i.e., most dense, He layer there is a critical angle of incidence. In Figure 6 only longitudinal waves are allowed in this layer, and therefore for waves incident from the bulk at angles greater than this critical angle, only evanescent waves exist in the layer. The critical angle is very close to the point where the three curves in Figure 6 appear to intersect. In this supercritical region, the penetration depth for evanescent waves is proportional to the wavelength of the evanescent waves. Therefore, as the frequency increases the transmission coefficient in the supercritical region will decrease. By comparison, in Figure 5, the critical angle for longitudinal waves is not even apparent, since the transverse waves seem to play the dominant role in determining TR. This is not surprising since the critical angle for transverse waves is very near $\pi/2$. The considerable enhancement of TR at the frequency corresponding to T = 1.49 K is due solely to the transverse waves in the first helium layer.

In Appendix E, we show a more complete set of figures in order to illustrate the frequency dependence of the transmission coefficient TR. The TR curves in Figure E1 combined with those in Figure 6 span the frequency range corresponding to 0.1-3.0 K, for the case of no transverse waves in the He. These TR curves show that the penetration depth of the evanescent longitudinal waves in the first, most dense He layer decreases with increasing frequency. For angles of incidence near 0.5 rad, a peak begins to appear in the T = 3.0 K curve of Figure E1. This corresponds to a strong coupling of the longitudinal waves in the first He layer with the transverse waves in the Cu. This peak is analogous to the peak which occurs near $\pi/2$ rad in the T = 0.1 K curve of Figure 6.

The curves in Figures E2-E7 show the transmission coefficient, TR, for frequencies corresponding to the temperature range 0.1-4.0 K. As the wavelength is decreased (frequency is increased) we see that the significant enhancement of TR occurs at increasing angles of incidence. This behavior is consistent with a condition for optimizing transmission of waves through a layer[48]; $\lambda/4 = d \cos\theta$, where λ, d and θ are respectively, the wavelength, thickness, and angle of transmission for the layer. Applying this condition to the transverse waves in the first He layer yields results which are consistent with the behavior of the TR curves in Figures E2-E7. If one views the transmission of waves through a layer in terms of multiple reflections within the layer, the optimum transmission occurs when the waves undergo constructive interference. Comparing the T = 3.0 K curve of Figure E6 with that of Figure E1, we can see the results of destructive and constructive interference of both types of waves in the first He layer. As an example, for angles of incidence beyond about 0.5 rad, the T = 3.0 K TR curve of Figure E6 is significantly less than the lower frequency TR curves shown in Figures E5-E6. We can only attribute this to important interference effects which must occur between the additional evanescent longitudinal waves which accompany the multiple reflections of transverse waves within the layer. With the exception of the strong peak near 0.5 rad, the T = 3.0 K curve of Figure E6 looks very much like the T = 3.0 K curve of Figure E1. The strong peak, of course, is due to constructive interference of the transverse waves in the first He layer; and as the wavelength is decreased, this peak occurs at increasing angles of incidence. Figures E2-E7 show this dependence quite clearly.

When comparing the TR curves of Figures E1 and E6 one must remember that the longitudinal sound velocities in the first He layer, in each case, are not the same. For the calculated TR curves of Figure E1, experimental sound velocity data for liquid He^4 are used, while for Figure E6 experimental sound velocity data for solid He^4 in the first He layer are used. The critical angle for longitudinal waves in the first He layer will be less when the solid He^4 data are used (Figure E6) than when the liquid He^4 data are used (Figure E1) since the longitudinal sound velocity in solid He^4 is greater than in liquid He^4 (for equal densities).

In Figures E8-E13 we show calculated TR curves using a small attenuation, V = 0.01, and with all parameters identical to those used for Figures E2-E7. The purpose of these is to enable one to identify the structure of the TR curve as a function of angle of incidence and frequency. For example, in Figure E10 we can see the contributions to TR associated with the two critical angles, $\theta_{cr\ell} = 0.0475$ rad and $\theta_{crt} = 0.1035$ rad, the Rayleigh peak at $\theta_R = 0.110$ rad, and the peak associated with the constructive interference of transverse waves in the first He layer (which occurs at increasing angles of incidence as the frequency is increased).

We show calculated Kapitza resistance values as a function of temperature (in the form $R_K T^3$) in Figures 8-17. The parameters used in calculating the lower $R_K T^3$ curve in Figure 8 are the same as those used for Figure 5. Similarly, the upper $R_K T^3$ curve in Figure 8 is calculated using the same parameters as those used for Figure 6. The relatively higher transmission coefficients associated with including transverse waves in the solid He layer, as shown in Figure 5,

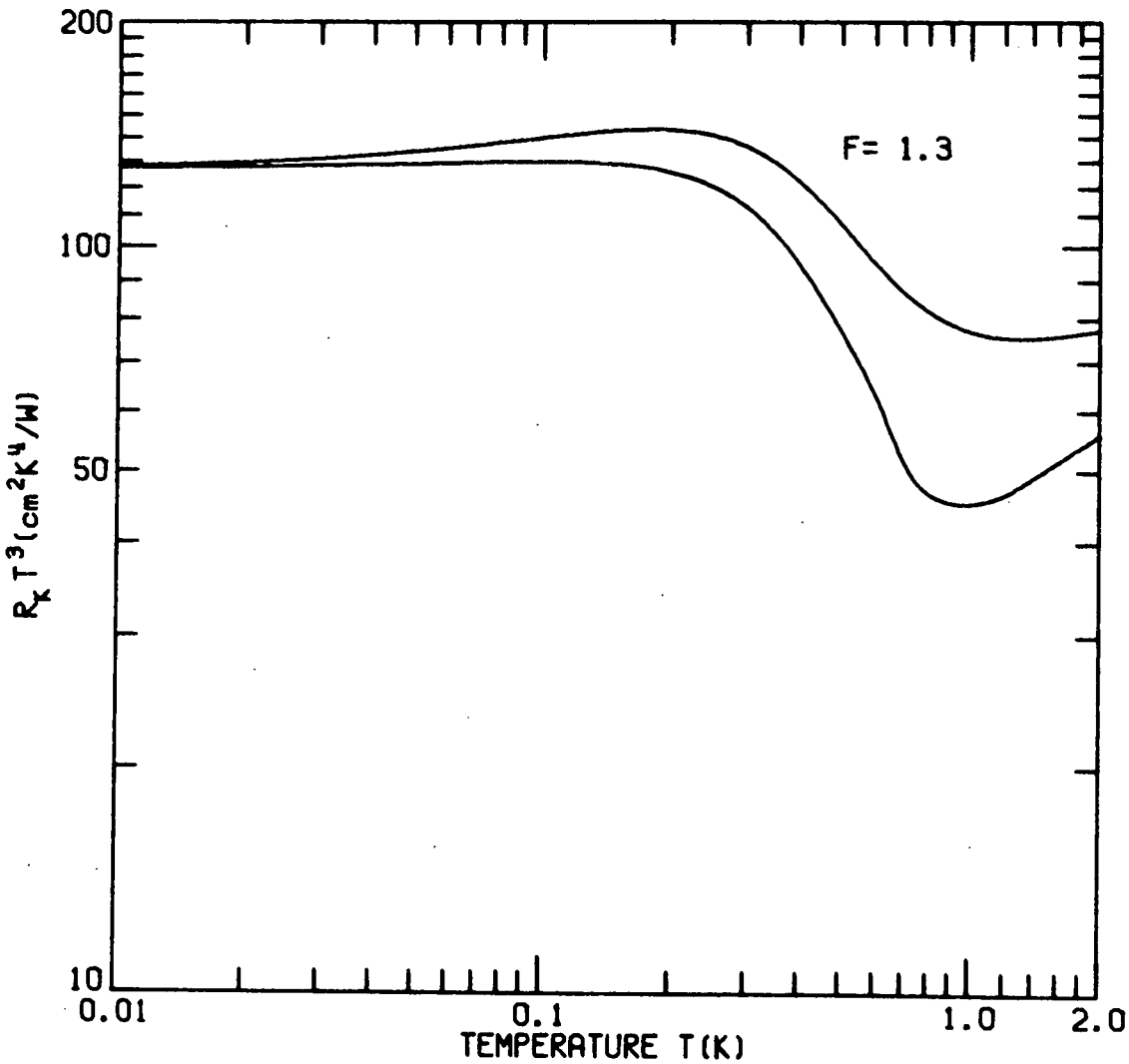

Figure 8: $R_K T^3$ calculated as a function of temperature T. For the lower curve both longitudinal and transverse waves are included in the first helium layer, while only longitudinal waves in the first helium layer are used to calculate the upper curve.

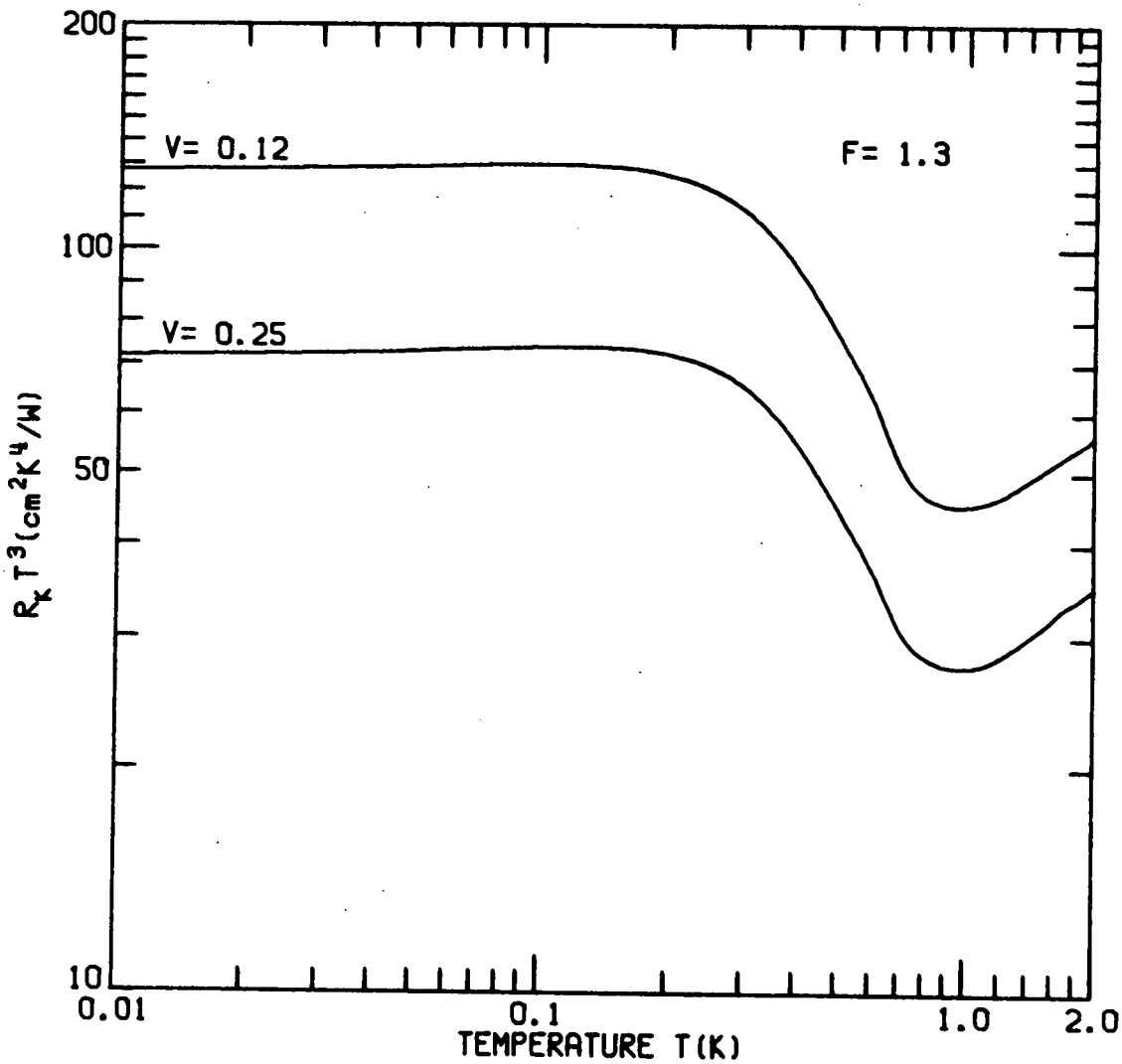

Figure 9: $R_K T^3$ calculated for two attenuations in the copper. The first helium layer is considered to be a solid; i.e., both longitudinal and transverse are used.

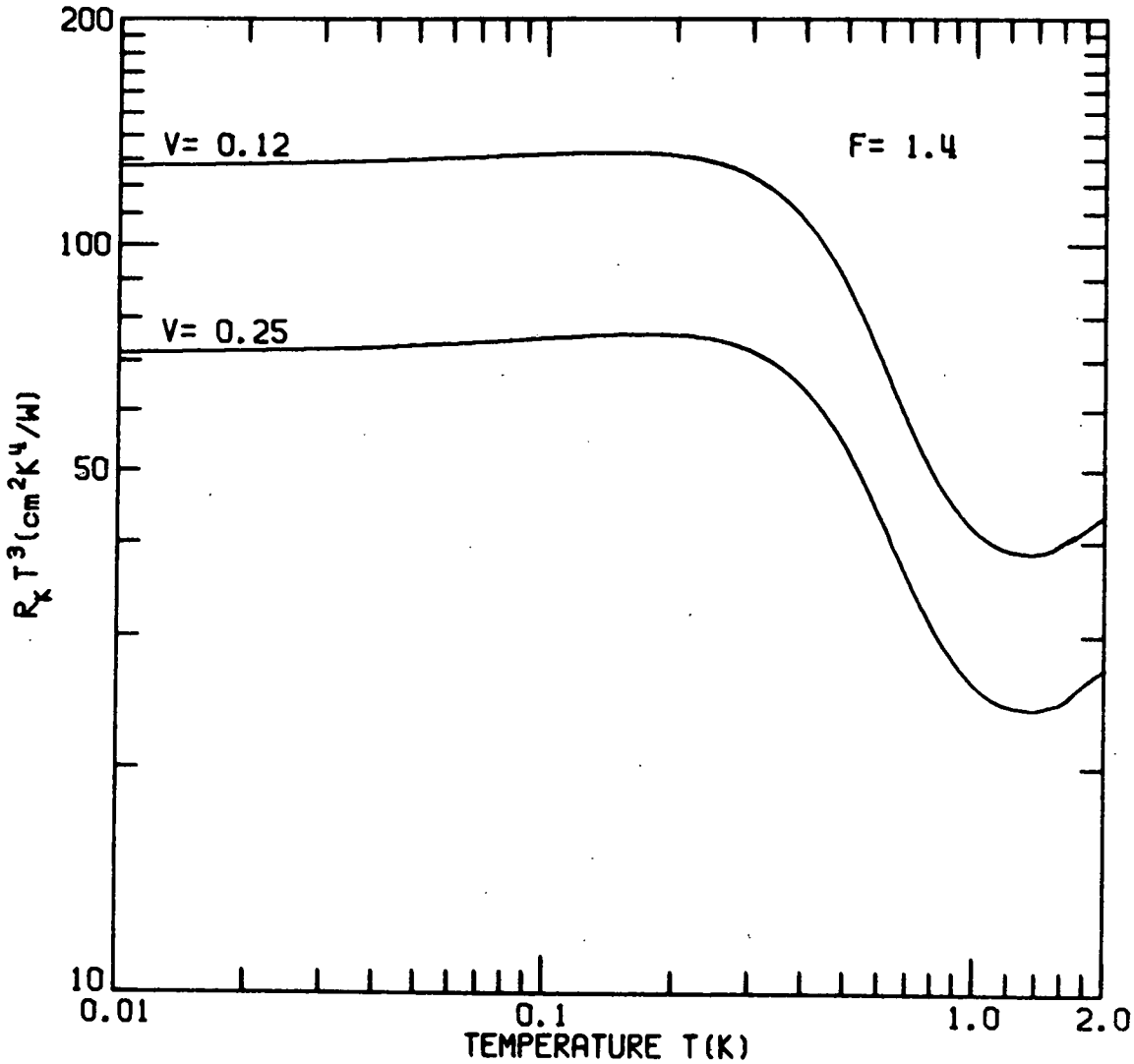

Figure 10: $R_K T^3$ calculated for two attenuations with a helium density factor F = 1.4.

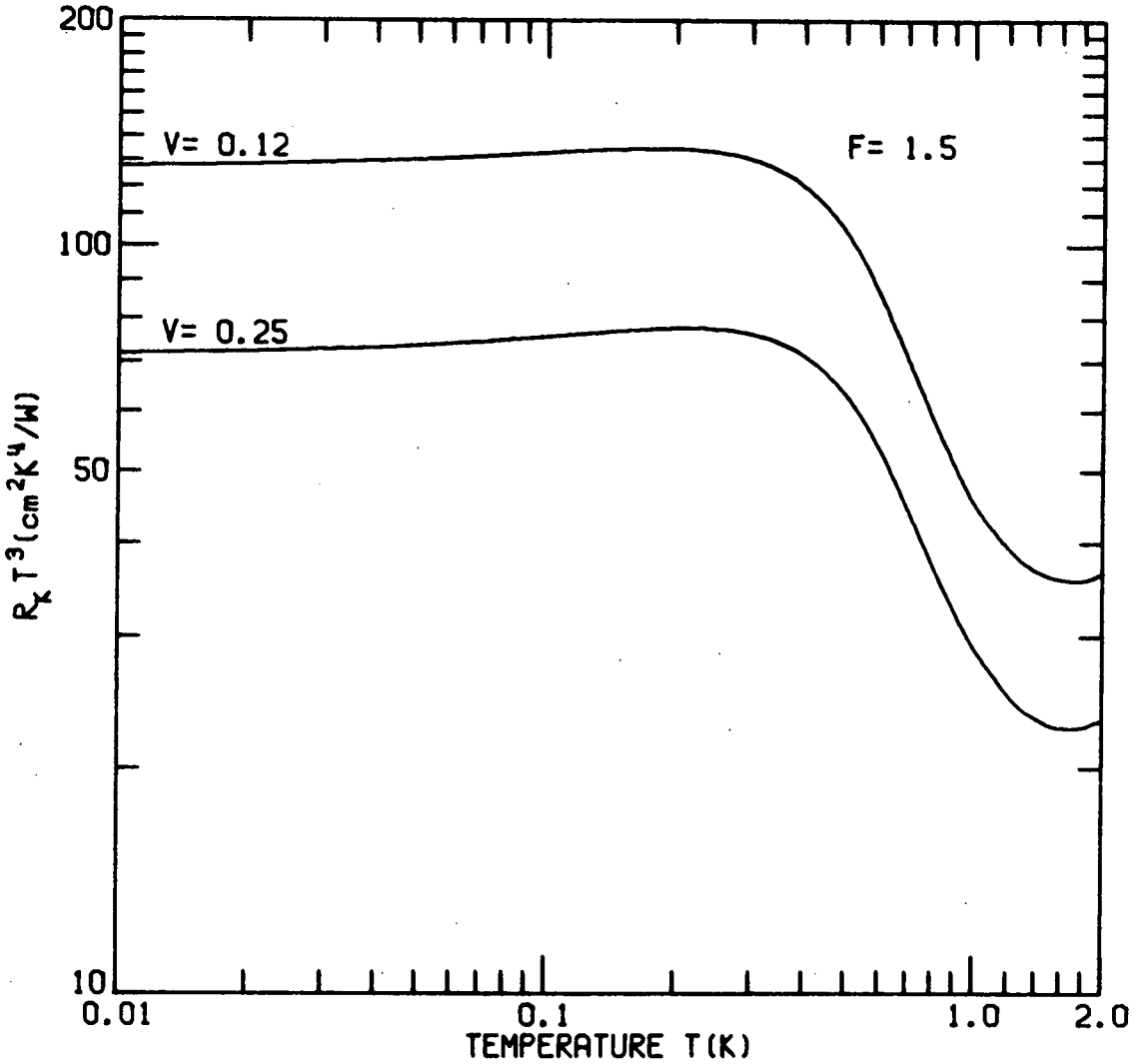

Figure 11: $R_K T^3$ calculated for two attenuations with a helium density factor F = 1.5.

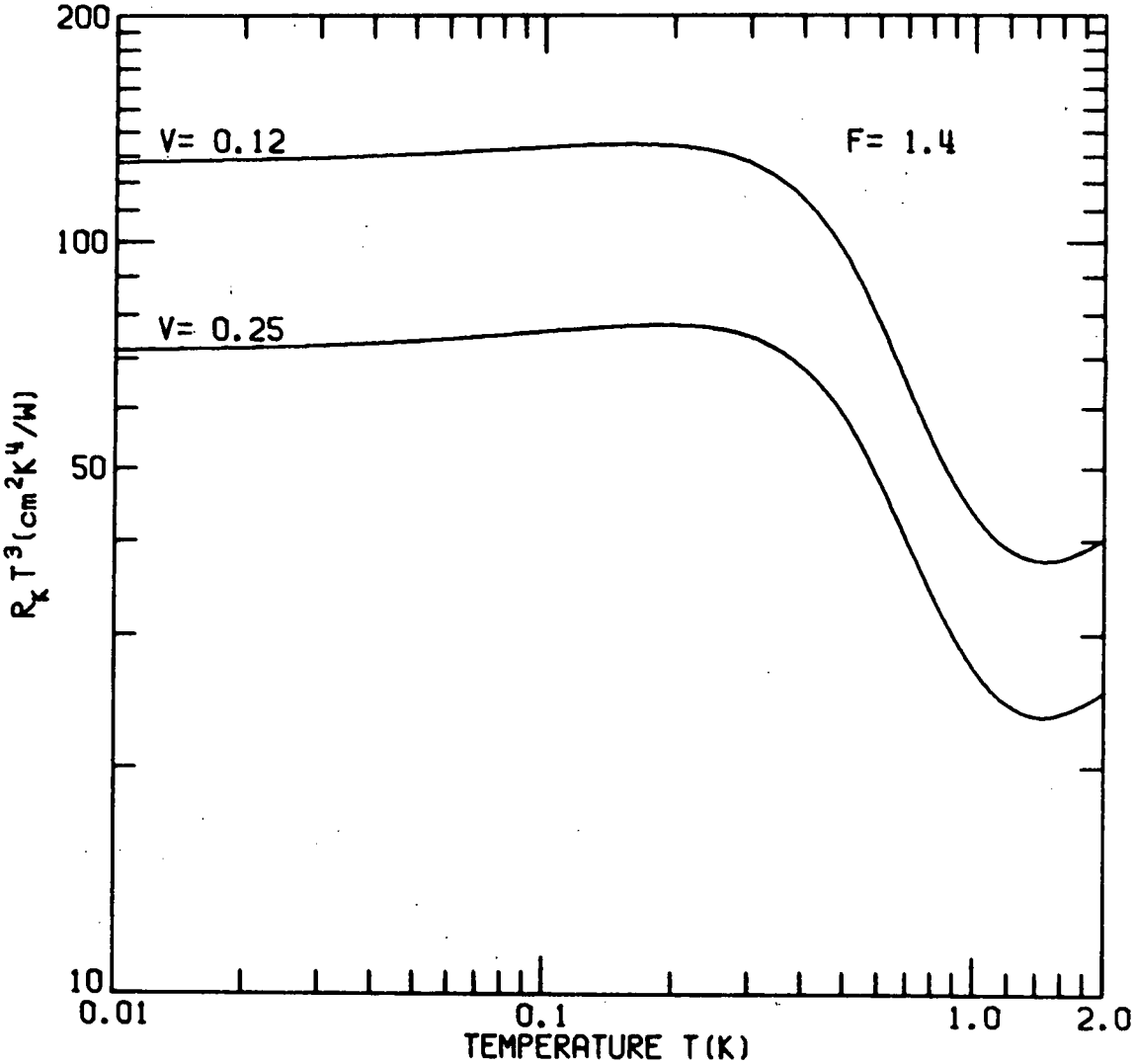

Figure 12: $R_K T^3$ calculated for two attenuations and a helium density factor F = 1.4. Transverse waves are included only in the first, most dense, helium layer.

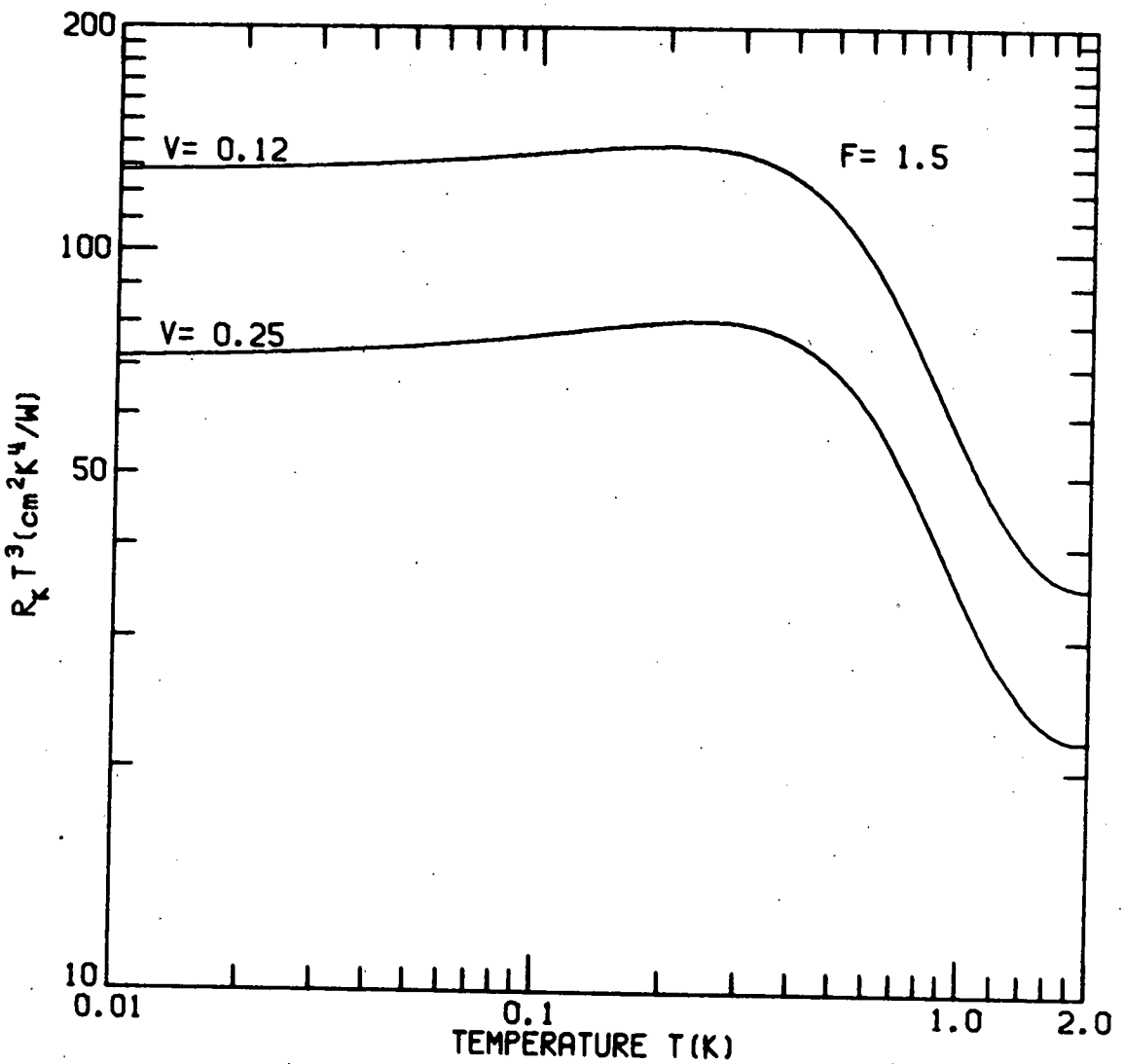

Figure 13: $R_K T^3$ calculated for two attenuations and a helium density factor F = 1.5. Transverse waves are included only in the first, most dense, helium layer.

correspond, naturally, to a lower R_K. The effect of including transverse waves in the solid helium layer is seen to be significant over a wide temperature range. Figure 9 shows the effect on $R_K T^3$ of using a higher attenuation, V = 0.25, for the case of transverse waves allowed. The effect of this increased attenuation is to lower the R_K, although the overall T dependence is still the same.

In Figures 10 and 11 we compare $R_K T^3$ values for two different attenuations in each figure but with higher values for the parameter F. In Figure 10, the distance from the copper substrate for which the helium density is constant ($\rho_1 = 1.4\ \rho_{He}$) is about 6 Å. Similarly, in Figure 11 the distance for which the helium density is constant ($\rho_1 = 1.5\ \rho_{He}$) is about 5.3 Å. We see that the basic shape of the $R_K T^3$ curve in either case has not changed by comparison with Figure 9. The $R_K T^3$ minimum, for a given value of V, is lower and occurs at a higher temperature when F is increased. We observed this trend to hold, for increasing F, on up to F = 2.0. The physical reason for this trend is that higher values for the density of the first He layer give higher sound velocities and this corresponds to longer characteristic wavelengths.

In Figures 12 and 13 we show calculated $R_K T^3$ values using (with one exception) the same parameters, respectively, as for the curves shown in Figures 10 and 11. For the curves shown in Figures 12 and 13 transverse waves are included only in the first, most dense, He layer (in Figure 12 for $\rho_1 = 1.4\ \rho_{He}$, $d_1 = 6$ Å and in Figure 13 for $\rho_1 = 1.5\ \rho_{He}$, $d_1 = 5.3$ Å) whereas, in Figures 10 and 11, transverse waves are allowed in the dense He region for $\rho \geq 1.3\ \rho_{He}$, $d \leq 7$ Å. Including transverse waves over a longer distance in the dense He

region improves the impedance matching. This can be seen by comparing the $R_K T^3$ curves in Figures 10 and 11 to those in Figures 12 and 13, respectively.

In order to test how sensitive our results were to the details of the density profile we investigated the effect of changes in the analytic form of $\rho(d)$ given in Equation 26. We observed only small changes resulted in the calculated values of $R_K T^3$. That is, the two important factors in the density profile are the maximum values of the density, and the distance over which the density is constant.

In Figures 14, 15, 16 and 17 we show $R_K T^3$ values for attenuations in the copper which vary with distance from the copper surface. This is what one expects for a real solid. We also show on these figures some experimental data[21,51,52,55] to facilitate comparisons. In Figure 14, V in the Cu has the following simple dependence: V = 0.25 for a layer which extends from the copper surface 20 Å into the copper, and V = 0.12 beyond the layer. For Figure 15: V = 0.30 for 20 Å, V = 0.12 for the next 250 Å, and V = 0.06 beyond the layers. For Figure 16: V = 0.42 for 25 Å, V = 0.12 for the next 250 Å, and V = 0.06 beyond the layers. Finally, for Figure 17: V = 0.50 for 25 Å, V = 0.12 for the next 100 Å, and V = 0.06 beyond the layers.

The calculated $R_K T^3$ values used in Figures 8-17 are also tabulated in Appendix F.

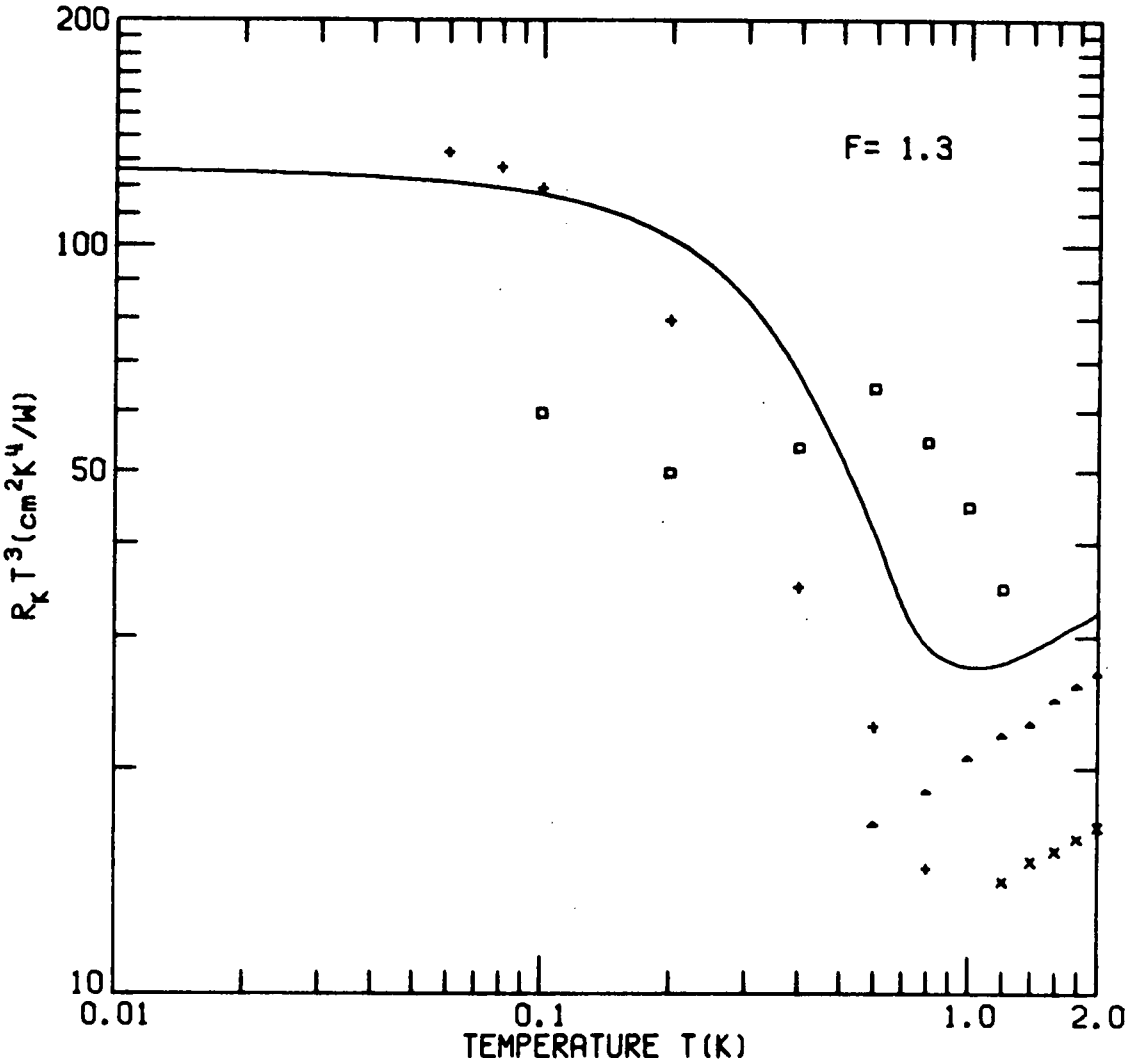

Figure 14: $R_K T^3$ calculated using an attenuation profile in the copper: $V_o = 0.25$ for a layer which extends from the copper surface 20 A into the copper, and V = 0.12 beyond the layer. The individual points are experimental values; ▲ - Reference 21, + - Reference 51, ▫ - Reference 52, x - Reference 55.

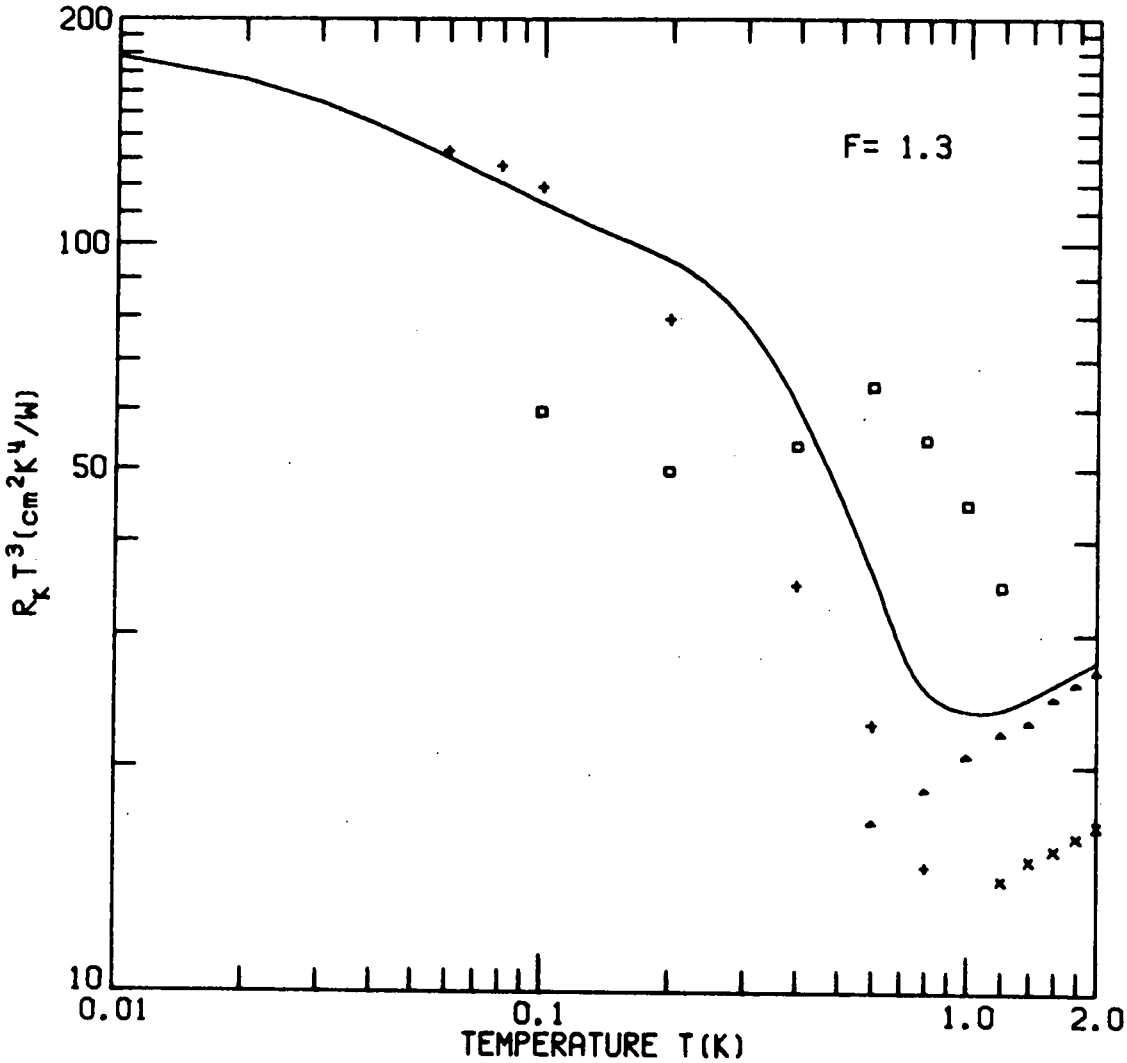

Figure 15: $R_K T^3$ calculated using an attenuation profile in the copper: V = 0.30 for 20 Å, V = 0.12 for the next 250 Å, and V = 0.06 beyond the layers. The individual points are experimental values; ▲ - Reference 21, + - Reference 51, ▫ - Reference 52, x - Reference 55.

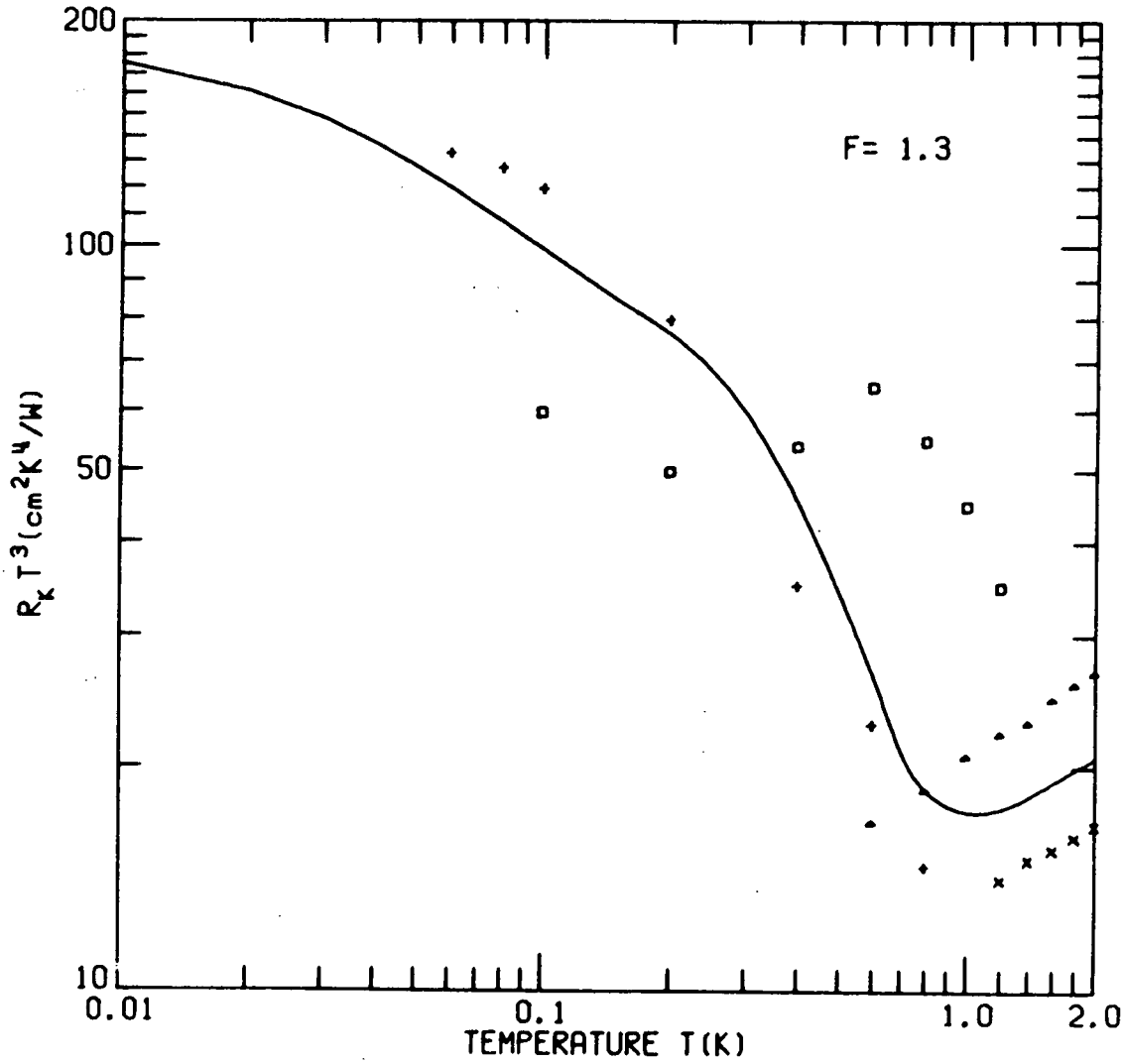

Figure 16: $R_K T^3$ calculated using an attenuation profile in the copper: V = 0.42 for 25 Å, V = 0.12 for the next 250 Å, and V = 0.06 beyond the layers. The individual points are experimental values; ▲ - Reference 21, + - Reference 51, ▫ - Reference 52, x - Reference 55.

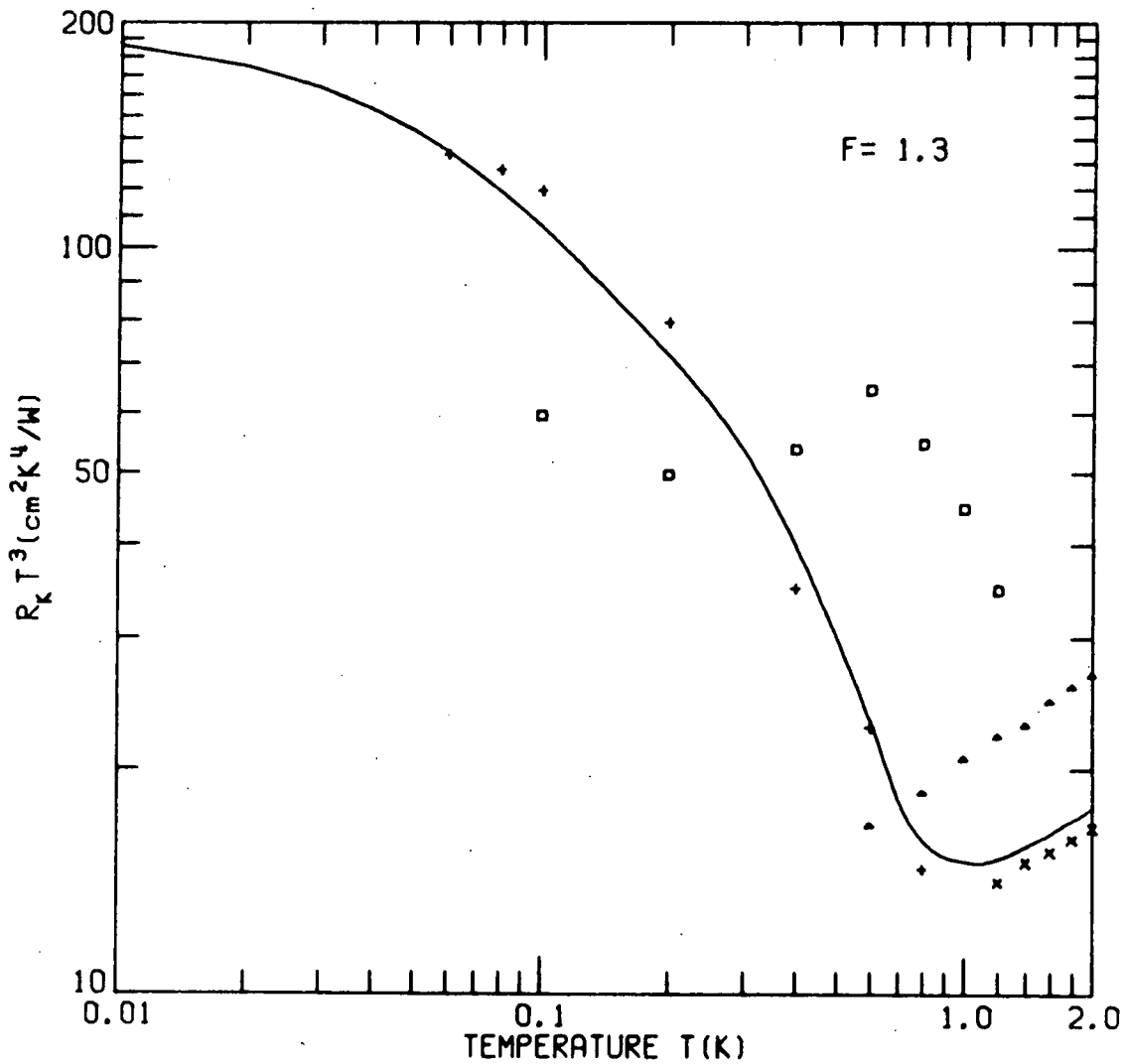

Figure 17: $R_K T^3$ calculated using an attenuation profile in the copper: V = 0.50 for 25 Å, V = 0.12 for the next 100 Å, and V = 0.06 beyond the layers. The individual points are experimental values; ▲ - Reference 21, + - Reference 51, □ - Reference 52, x - Reference 55.

IV. SUMMARY AND CONCLUSIONS

A. The Sublimation and Vapor Pressure Experiment

We have measured the sublimation and vapor pressure of Ar^{36} over a wide temperature range in the solid and for temperatures in the liquid up to the boiling point. These measurements were reproducible for two different runs to the extent that it was not possible to distinguish the two sets of data.

The effects of impurities are most evident (see Figure 2) at the lowest temperatures for which data were taken. These effects, however, represent the presence of non-condensable impurities in the vapor which at the higher temperatures have only a negligible effect on the observed pressures. The presence of condensable impurities (i.e., N_2 and O_2) have a significant effect only for temperatures in the liquid range, $T \gtrsim 84$ K, and even then the effect on vapor pressure is small; these impurities raise the vapor pressure by less than 0.1% (~ 1 Torr at 84 K).

The most important result of our experiment is that our sublimation-pressure data are in good agreement with the predictions of the improved self-consistent phonon theory of Goldman, Horton and Klein.[9,10] Our Ar^{36} data further show, when compared with equivalent data on Ar^{N}, the sublimation and vapor pressure of Ar^{36} to be consistently higher than that of Ar^{N}. This isotopic effect on sublimation pressure is commonly referred to as the vapor-pressure ratio between Ar^{36} and Ar^{N}.

Our vapor-pressure ratios are also in good agreement with the predictions of the improved self-consistent theory referred to above.

More exact knowledge of the thermodynamic properties of rare-gas solids and of isotopic effects could be determined if other kinds of experimental data were available. Some particularly useful kinds of experiments, for example, would be specific heat and thermal conductivity measurements on normal and isotopically pure rare-gas solids.

B. The Calculation of Kapitza Resistance

We calculated the Kapitza resistance, $R_K(T)$, over a range of temperatures (0.01-2.0 K) for which experimental data are available. In addition to considering the effects of phonon attenuation in the Cu, we have included the impedance matching effects associated with a dense He region of varying density at the Cu-He^4 interface.

As we have seen from our initial calculations, neither of these effects, when considered alone, is sufficient to explain the experimentally observed R_K values. By considering only phonon attenuation effects in the Cu, we can obtain R_K values which agree in magnitude with experimental R_K values at low temperatures; $T \leq 0.5$ K. We can, furthermore, obtain the experimentally observed temperature dependence, at these lower temperatures, by allowing the attenuation to vary with distance from the copper surface. It is not possible, however, to obtain agreement with experiment in the magnitude or T dependence of R_K for $T \gtrsim 0.5$ K without also considering the effects of impedance matching.

We believe we have shown the importance of considering impedance matching effects in conjunction with phonon attenuation effects on Kapitza resistance. It is clear that the magnitude and temperature

dependent features of experimentally observed Kapitza resistances are included in the results of our model. It is also clear, however, that much more experimental information than is currently available, is needed about the detailed structure of the copper and helium in the vicinity of the interface.

APPENDICES

APPENDIX A: DECOMPOSITION OF THE DISPLACEMENT FIELD

In order to decompose the displacement field into longitudinal and transverse components, we first express Equation 28 in the vector form:

$$\rho(\partial^2\vec{S}/\partial t^2) = \mu\nabla^2\vec{S} + (\lambda+2\mu)\ \underset{\sim}{\nabla}\underset{\sim}{\nabla}\cdot\vec{S}\ . \tag{A1}$$

Next, we consider the displacement field $\vec{S}$ as composed of two parts:

$$\vec{S} = \vec{S}_\ell + \vec{S}_t\ , \tag{A2}$$

such that

$$\underset{\sim}{\nabla} \times \vec{S}_\ell = 0 \tag{A3}$$

and

$$\underset{\sim}{\nabla}\cdot\vec{S}_t = 0\ . \tag{A4}$$

Equation A3 defines the longitudinal component, $\vec{S}_\ell$ and Equation A4 defines the transverse component, $\vec{S}_t$. Using Equations A3, A4 and the vector identity

$$\underset{\sim}{\nabla} \times (\underset{\sim}{\nabla} \times \vec{A}) = -\nabla^2\vec{A} + \underset{\sim}{\nabla}\underset{\sim}{\nabla}\cdot\vec{A}\ , \tag{A5}$$

we can express Equation A1 in the form:

$$\rho(\partial^2\vec{S}_t/\partial t^2) + \rho(\partial^2\vec{S}_\ell/\partial t^2) = \mu\nabla^2\vec{S}_t + (\lambda + 2\mu)\ \nabla^2\vec{S}_\ell\ . \tag{A6}$$

It is clear then, that solutions of Equation A1 can be obtained by solving the equations:

$$\rho(\partial^2\vec{S}_\ell/\partial t^2) = (\lambda + 2\mu)\ \nabla^2\vec{S}_\ell \tag{A7}$$

and

$$\rho(\partial^2\vec{S}_t/\partial t^2) = \mu\nabla^2\vec{S}_t\ . \tag{A8}$$

It is sometimes more convenient to work with the velocity fields, $\vec{v}_\ell \equiv \partial\vec{S}_\ell/\partial t$, and $\vec{v}_t \equiv \partial\vec{S}_t/\partial t$. This is particularly true when one wishes to calculate the transmission and reflection of energy at a boundary. Using Equations A7 and A8 we obtain the equations for $\vec{v}_\ell$ and $\vec{v}_t$:

$$\rho(\partial^2\vec{v}_\ell/\partial t^2) = (\lambda + 2\mu)\ \nabla^2\vec{v}_\ell\ , \tag{A9}$$

and

$$\rho(\partial^2\vec{v}_t/\partial t^2) = \mu\nabla^2\vec{v}_t\ . \tag{A10}$$

At this point we define the velocity potentials, ϕ and $\vec{\psi}$, by the equations:

$$\vec{v}_\ell = \underset{\sim}{\nabla}\phi\ , \tag{A11}$$

and

$$\vec{v}_t = \underset{\sim}{\nabla} \times \vec{\psi}\ . \tag{A12}$$

Since $\underset{\sim}{\nabla}\cdot(\underset{\sim}{\nabla} \times \vec{\psi}) = 0$ and $\underset{\sim}{\nabla} \times (\underset{\sim}{\nabla}\phi) = 0$, we then obtain, using Equations A5, and A9 - A12, the desired wave equations:

$$\rho(\partial^2\phi/\partial t^2) = (\lambda + 2\mu)\ \nabla^2\phi\ , \tag{A13}$$

and

$$\rho(\partial^2\vec{\psi}/\partial t^2) = \mu\nabla^2\vec{\psi}\ . \tag{A14}$$

Equations A13 and A14 are, respectively, Equations 29 and 30 of Chapter III.

APPENDIX B: THE ENERGY FLUX

In this section we shall consider the propagation of energy in an anisotropic, viscoelastic material. That is, we consider the general form for the stress tensor T_{ij} [49]:

$$T_{ij} = C_{ijkm}a_{km} + \eta_{ijkm}v_{km} , \tag{B1}$$

where

$$a_{km} = (1/2)[(\partial S_k/\partial x_m) + (\partial S_m/\partial x_k)] \tag{B2}$$

and

$$v_{km} = \partial a_{km}/\partial t . \tag{B3}$$

In Equation B1, C_{ijkm} is the elastic tensor and η_{ijkm} is the viscosity tensor. Equation B2 defines the strain tensor in the same way as it is defined for Equation 27, so that the equations of motion for this system are given by Equation 28:

$$\rho(\partial^2 S_i/\partial t^2) = \partial T_{ij}/\partial x_j . \tag{28}$$

The components of the elastic tensor, C_{ijkm}, have the following symmetry properties[49]:

$$C_{ijkm} = C_{jikm} = C_{jimk} = C_{ijmk} = C_{kmij} = C_{mkij} = C_{mkji} = C_{kmji} . \tag{B4}$$

This is known as Voigt symmetry and is a consequence of two assumptions: The strain tensor is symmetric (no local rotations) and the existence of the elastic potential (analogous to the Hooke's law assumption for stretching in one dimension; i.e., assuming the potential is a quadratic function of strain).

The components of the viscosity tensor, η_{ijkm}, also have this Voigt symmetry. The key assumption in this case is that the rate at which energy is absorbed is quadratic in the time derivative of strain v_{km}.

In terms of the velocity field v_i (defined in Appendix A), Equation 28 may be written

$$\rho(\partial v_j/\partial t) = \partial T_{ij}/\partial x_i \ . \tag{B5}$$

Multiplying Equation B5 by v_j and summing over repeated indices gives

$$\frac{\partial}{\partial t}[(1/2)\rho v_j v_j] = (\partial T_{ij}/\partial x_i)v_j \ . \tag{B6}$$

Using Equation B1 and the symmetry relations expressed in Equation B4, we then obtain the conservation equation:

$$\frac{\partial}{\partial t}[(1/2)\rho v_j v_j + (1/2)C_{ijkm}a_{ij}a_{km}] = \frac{\partial}{\partial x_i}(T_{ij}v_j) - \eta_{ijkm}v_{ij}v_{km} \ . \tag{B7}$$

The left side of Equation B7 is the time derivative of the energy density, and the second term on the right side of Equation B7 is the rate at which energy is absorbed. For this reason, the term $-T_{ij}v_j$ is taken to be the energy flux.

Assuming time dependent solutions (of Equation B5) having the simple harmonic form, $e^{-i\omega t}$, we find the time averaged energy flux, $\vec{P}$, with components given by Equation 33:

$$P_i = (1/2)\ \mathrm{Re}(-T_{ij}v_j^*) \ . \tag{33}$$

APPENDIX C: THE TRANSMISSION COEFFICIENTS

Applying the appropriate boundary conditions to a system of solid layers, the components of stress and velocity in the mth layer (at $z = z_m$) are related to those in the (m-1)st layer (at $z = z_{m-1}$) by the following set of equations,[48]

$$\xi_i^{(m)} = a_{ij}^{(m)} \; \xi_j^{(m-1)} \tag{C1}$$

where the $\xi_i^{(m)}$ are defined by,

$$\xi_1^{(m)} = -T_{zz}^{(m)}, \; \xi_2^{(m)} = v_x^{(m)}, \; \xi_3^{(m)} = -T_{xz}^{(m)} ,$$

and $\xi_4^{(m)} = v_z^{(m)}$.

The coefficients, $a_{ij}^{(m)}$, in Equation C1 are given by:

$$a_{11}^{(m)} = \cos 2\gamma_m \cos P_m + 2\sin^2\gamma_m \cos Q_m$$

$$a_{12}^{(m)} = (2\omega\rho_m/\kappa_m)\sin\gamma_m \cos 2\gamma_m[\cos P_m - \cos Q_m]$$

$$a_{13}^{(m)} = i[\sin 2\gamma_m \sin Q_m - (k_x/k_{mz})\cos 2\gamma_m \sin P_m]$$

$$a_{14}^{(m)} = -i\omega\rho_m[(1/k_{mz})\cos^2 2\gamma_m \sin P_m + (1/\kappa_{mz})\sin^2 2\gamma_m \sin Q_m]$$

$$a_{21}^{(m)} = (k_x/\omega\rho_m)[\cos P_m - \cos Q_m]$$

$$a_{22}^{(m)} = 2\sin^2\gamma_m \cos P_m + \cos 2\gamma_m \cos Q_m$$

$$a_{23}^{(m)} = (-i/\omega\rho_m)[(k_x^2/k_{mz})\sin P_m + \kappa_{mz} \sin Q_m]$$

$$a_{24}^{(m)} = i[\sin 2\gamma_m \sin Q_m - (k_x/k_{mz})\cos 2\gamma_m \sin P_m]$$

$$a_{31}^{(m)} = ik_x[(1/\kappa_{mz})\cos 2\gamma_m \sin Q_m - (2k_{mz}/\kappa_m^{\ 2})\sin P_m]$$

$$a_{32}^{(m)} = -i\omega\rho_m[4k_{mz}/\kappa_m^{\ 2})\sin^2\gamma_m \sin P_m + (1/\kappa_{mz})\cos^2 2\gamma_m \sin Q_m]$$

$$a_{33}^{(m)} = 2\sin^2\gamma_m \cos P_m + \cos 2\gamma_m \cos Q_m$$

$$a_{34}^{(m)} = (2\omega\rho_m/\kappa_m)\sin\gamma_m \cos 2\gamma_m[\cos P_m - \cos Q_m]$$

$$a_{41}^{(m)} = (-i/\omega\rho_m)[k_{mz}\sin P_m + (k_x^{\ 2}/\kappa_{mz})\sin Q_m]$$

$$a_{42}^{(m)} = ik_x[(1/\kappa_{mz})\cos 2\gamma_m \sin Q_m - (2k_{mz}/\kappa^2_m)\sin P_m]$$

$$a_{43}^{(m)} = (k_x/\omega\rho_m)[\cos P_m - \cos Q_m]$$

$$a_{44}^{(m)} = \cos 2\gamma_m \cos P_m + 2\sin^2\gamma_m \cos Q_m.$$

In the above expressions, the angles P_m and Q_m are defined by; $P_m = k_{mz}d_m$ and $Q_m = \kappa_{mz}d_m$, where d_m is the thickness of the mth layer. The components of the wave vectors are obtained using the form of Snell's law valid even for absorbing media: $k_{mx} = \kappa_{mx} \equiv k_x = k_{n+1}\sin\theta_{n+1}$, $k_{mz}^2 = k_m^2 - k_x^2$, and $\kappa_{mz}^2 = \kappa_m^2 - k_x^2$. The angle, γ_m, used in the remaining trigonometric functions is defined by, $\sin\gamma_m = k_x/\kappa_m$ and $\cos\gamma_m = \kappa_{mz}/\kappa_m$. For M solid layers, there are M matrices such as the one shown in Equation C1. We can multiply these M matrices together to obtain a single matrix, A_{ij}, which relates the stress and velocity components in the mth layer (at $z = z_m$) to those in the semi-infinite solid (at $z = 0$). That is,

$$\xi_i^{(M)} = A_{ij}\ \xi_j^{(0)} \tag{C2}$$

where

$$A_{ij} = a_{ik}^{(M)}\ a_{kl}^{(M-1)} \ldots a_{mn}^{(2)}\ a_{nj}^{(1)}\ .$$

For the simple case of the liquid-solid boundary of the Mth layer, we define the input impedance,[48] $Z_M^{(in)}$, as $Z_M^{(in)} = -T_{zz}^{(M)}/v_z^{(M)}$.

The input impedance for successive liquid layers is then calculated according to the recursion formula,

$$Z_j^{(in)} = Z_j[(Z_{j-1}^{(in)} - iZ_j \tan P_j)/(Z_j - iZ_{j-1}^{(in)} \tan P_j)] \ . \qquad (C3)$$

The phase angle, P_j, is defined in the same way as for the solid layers, and Z_j is the characteristic impedance of the jth layer; $Z_j = \omega\rho_j/k_{jz}$. Recalling that the waves in the jth layer are given by the scalar potential,

$$\phi_j = [A_j e^{ik_{jz}z} + B_j e^{-ik_{jz}z}]e^{i(k_x x-\omega t)} \ ,$$

we then have the following relations;

$$A_{M+1}/A_{n+1} = (\rho_{n+1}/\rho_{M+1}) \prod_{j=M+1}^{n} [(Z_j^{(in)} + Z_j)/(Z_j^{(in)} + Z_{j+1})]e^{iP_j} \qquad (C4)$$

$$B_{M+1}/A_{M+1} = (Z_M^{(in)} - Z_{M+1})/(Z_M^{(in)} + Z_{M+1}) \qquad (C5)$$

$$R \equiv B_{n+1}/A_{n+1} = (Z_n^{(in)} - Z_{n+1})/(Z_n^{(in)} + Z_{n+1}) \qquad (C6)$$

Equations C1-C6 enable us to calculate the energy transmission, TR, at the boundary of the semi-infinite solid (z = 0) and at the boundary of the semi-infinite liquid ($z = z_n$). At $z = z_n$ we have

$$TR = 1 - |R|^2 \qquad (C7)$$

At z = 0 the expressions are much more complicated, but we can describe the procedure used. In the semi-infinite solid, the velocity potentials are given by,

$$\phi_o = (A_o e^{ik_{oz}z})e^{i(k_x x-\omega t)} \quad \text{and} \quad \psi_o = (C_o e^{i\kappa_{oz}z})e^{i(k_x x-\omega t)} \ .$$

Since the shear stress component, $T_{xz}^{(M)}$, is zero at the liquid-solid interface, we can obtain a relationship between the wave amplitudes,

A_o and C_o, by using Equation C2. Furthermore, using Equations C4 and C5 we can calculate any of the other stress and velocity components at the liquid-solid interface. A_o and C_o can both then be determined. Knowing the wave amplitudes, A_o and C_o, we then calculate the energy transmission coefficient at the boundary of the semi-infinite solid according to Equation 34.

APPENDIX D: KAPITZA RESISTANCE PROGRAM

TABLE D1

List of the FORTRAN program, KR and its subroutines, used to calculate the Kapitza resistance.

```
      PROGRAM KR(OUTPUT)
      COMMON PO,CO,VO,P1,C1,C1T,V1,V1T,PS,CSL,CST,VSL,VST
      COMMON/Y/VI,W,N
      COMMON /Z/ THO,DTH
      COMMON/XY/ERROR1,DTH1,DTH2,LAST,LAST1,LAST2
      COMMON /XZ/ IFLAG,JFLAG,KFLAG
      COMMON/XZV/LFLAG,XMAXV,NV
      COMMON/TOCH/A
      COMMON/TOARRAY/TM,TRW,DTRW,TRWS,DTRWS,NMAX,DELTA,ALPHA
      COMMON/LAYERS/NINF,NSUP
      COMMON/TOK/T,DT,NOFT,DX,NT,B,ERRORA,ERRORF,TMIN,TMAX
      COMMON/DENSE/AX,BX,XMIN,XMAX
      COMMON/SAVE/PHMAX,QHMAX
      COMMON/VINS/P1S,V1S,XMINS
      COMMON/VINH/P1H
      DIMENSION TM(200),TRW(200),DTRW(200),TRWS(200),DTRWS(200)
      DIMENSION STHO(64),CTHO(64),TR(64),TL(64)
  100 FORMAT(5F15.5)
      PHMAX=50.
      QHMAX=50.
      ALPHA=.1
      DX=3.83
      F=2.
      G=.16
      XMIN=3.60
      XMAX=10.
      BX=ALOG(G)/ALOG(XMIN/XMAX)
      AX=(F-1.)*(XMIN**BX)
      T=.4 $ TMIN=.377 $ TMAX=8. $ DT=.1 $ NOFT=20 $ DELTA=.05
      F=1.4 $ XMIN=6. $ XMAXV=6. $ NV=1 $ NSUP=16 $ KFLAG=2
      ALPHA=ALPHA*(XMAX-XMIN+4.)/(XMAX-XMAXV+4.)
      NINF=XMAX-XMAXV+5
      IFLAG=1
      JFLAG=1
      LFLAG=1
      ERROR1=.01 $ ERRORA=.005 $ ERRORF=.01
      A=.353825 $ B=7.846685E8
      PO=.145 $ CO=23800.
      P1=F*PO $ P1H=P1
```

Table D1 (cont'd.)

```
      C1=-72437.+637606.*P1 $ C1T=.5*C1
      IF(KFLAG.EQ.1)C1=-44173.+468509.*P1
      PS=8.93 $ CSL=500000. $ CST=230000.
      VO=0.
      V1=0.
      VSL=.12
      V1T=V1 $ VST=VSL
      LAST1=6
      LAST2=6
      P1S=P1H $ V1S=V1 $ XMINS=XMIN
      P1S=PS $ C1=CSL $ C1T=CST $ V1S=.25 $ XMINS=20.
      XMIN=0.
      CALL KAPITZA
      END


      SUBROUTINE KAPITZA
      COMMON PO,CO,VO,P1,C1,C1T,V1,V1T,PS,CSL,CST,VSL,VST
      COMMON/XY/ERROR1,DTH1,DTH2,LAST,LAST1,LAST2
      COMMON/TOARRAY/TM,TRW,DTRW,TRWS,DTRWS,NMAX,DELTA,ALPHA
      COMMON/TOK/T,DT,NOFT,DX,NT,B,ERRORA,ERRORF,TMIN,TMAX
      DIMENSION TM(200),TRW(200),DTRW(200),TRWS(200),DTRWS(200)
  100 FORMAT(5E15.5)
  101 FORMAT(1I5,5E15.5)
      THM=ASIN(1.)
      DTH1=ASIN(CO/SCL)
      LAST=THM/DTH1
      DTH1=THM/LAST
      DTH2=(THM-LAST1*DTH1)/LAST2
      CALL INITIAL
      CALL ARRAY(TMIN,TMAX)
      NM=NMAX
      DO 2 I=1,NM
    2 PRINT 101,I,TM(I),TRW(I),DTRW(I),TRWS(I),DTRWS(I)
      T=T-DT
      DO 1 I=1,NOFT
      T=T+DT
      CALL SUMX(T,DX,ERRORA,ERRORF,FLUXT,FLUXTS)
      T3=T**3
      C2=CO**2
      RKI=B*FLUXT/C2
      RKT3=1./RKI
      RKIS=B*FLUXTS/C2
      RKTS3=1./RKIS
      RK=RKT3/T3
      RKS=RKTS3/T3
      PRINT 100,T,RK,RKT3
      PRINT 100,RKS,RKTS3
    1 CONTINUE
      RETURN
      END
```

Table D1 (cont'd.)

```
      SUBROUTINE CHOICE(X,T,TRWC,TRWCS)
      COMMON/TOCH/A
      COMMON/TOARRAY/TM,TRW,DTRW,TRWS,DTRWS,NMAX,DELTA,ALPHA
      DIMENSION TM(200),TRW(200),DTRW(200),TRWS(200),DTRWS(200)
      T1=A*T*X
      IF(T1.LT.TM(1))GO TO 1
      I=1.+ALOG(T1/TM(1))/ALOG(1.+DELTA)
      IF(I.GE.NMAX)GO TO 3
      TRWC=TRW(I)+(T1-TM(I))*DTRW(I)
      TRWCS=TRWS(I)+(T1-TM(I))*DTRWS(I)
      GO TO 2
    3 TRWC=TRW(NMAX)
      TRWCS=TRWS(NMAX)
      GO TO 2
    1 TRWC=TRW(1)
      TRWCS=TRWS(1)
    2 CONTINUE
  100 FORMAT(1I5,5E15.5)
      RETURN
      END


      SUBROUTINE INITIAL
      COMMON PO,CO,VO,P1,C1,C1T,V1,V1T,PS,CSL,CST,VSL,VST
      COMMON/X/AKO,AKO2,AK12,AKSL2,AKST,AKST2
      COMMON/VINS/P1S,V1S,XMINS
      TYPE COMPLEX AKO,AKO2,AK12,AKSL2,AKST,AKST2
      V11=V1
      V1=V1S
      AK12=(1.+(0.,1.)*V1)/C1
      AKI2=AK12**2
      AKO=(1.+(0.,1.)*VO)/CO
      AKO2=AKO**2
      AKSL2=(1.+(0.,1.)*VSL)/CSL
      AKSL2=AKSL2**2
      AKST=(1.+(0.,1.)*VST)/CST
      AKST2=AKST**2
      V1=V11
      RETURN
      END


      SUBROUTINE CONST(M,STHO,CTHO,TR,TL)
      COMMON PO,CO,VO,P1,C1,C1T,V1,V1T,PS,CSL,CST,VSL,VST
      COMMON/X/AKO,AKO2,AK12,AKSL2,AKST,AKST2
      COMMON/Y/VI,W,N
      COMMON /Z/ THO,DTH
      COMMON /XZ/ IFLAG,JFLAG,KFLAG
      COMMON/DENSE/AX,BX,XMIN,XMAX
      COMMON/VECTOR/AKSLZ,AKSTZ,AKX,AKX2,AK1Z
      COMMON/TRIGF/S2GST,C2GST
      COMMON/SAVE/PHMAX,QHMAX
```

Table D1 (cont'd.)

```
      TYPE COMPLEX AKO,AKO2,AK12,AKSL2,AKST,AKST2
      TYPE COMPLEX AKX,AKX2,AKOZ,AK1Z,AKSLZ,AKSTZ
      TYPE COMPLEX SGST,SGST2,S2GST,S2GST2,CGST,C2GST,C2GST2
      TYPE COMPLEX ZO,Z1,ZSL,ZST,ZN,PH,TANPH
      TYPE COMPLEX AKI,AKIZ,ZI,R
      TYPE COMPLEX EXPH,AL,SINPH,COSPH
      TYPE COMPLEX R2,AT,V2Z,FLUXSL,FLUXST,FLUXI
      TYPE COMPLEX AK2Z
      TYPE COMPLEX U,V,ATAL,ZN1,W4
      DIMENSION U(4),V(4)
      DIMENSION STHO(M),CTHO(M),TR(M),TL(M)
  100 FORMAT(5E15.5)
      DO 1 K=1,M
      THO=THO+DTH
      STHO(K)=SIN(THO)
      CTHO(K)=COS(THO)
      AKX=AKO*STHO(K)
      AKX2=AKX**2
      AKOZ=CSQRT(AKO2-AKX2)
      AK1Z=CSQRT(AK12-AKX2)
      AKSLZ=CSQRT(AKSL2-AKX2)
      IF(AKSLZ.EQ.(0.,0.))GO TO 3
      AKSTZ=CSQRT(AKST2-AKX2)
      SGST=AKX/AKST
      CGST=AKSTZ/AKST
      S2GST=2.*SGST*CGST
      SGST2=SGST**2
      C2GST=1.-2.*SGST2
      C2GST2=C2GST**2
      S2GST2=1.-C2GST2
      ZO=PO/AKOZ
      RZO=REAL(ZO)
      GO TO (16,17),KFLAG
   16 CONTINUE
      ZSL=PS/AKSLZ
      IF(AKSTZ.EQ.(0.,0.))GO TO 11
      ZST=PS/AKSTZ
      ZN=ZSL*C2GST2+ZST*S2GST2
      GO TO 12
   11 ZN=ZSL
   12 CONTINUE
      RZN+REAL(ZN)
      TO TO (6,7),IFLAG
    6 CONTINUE
      IF(AK1Z.EQ.(0.,0.))GO TO 18
      Z1=P1/AK1Z
      GO TO 19
   18 Z1=(1.E50,1.E50)
   19 CONTINUE)
      AL=2.*ZSL/(ZN+Z1)
      ZI=Z1
      PH=10.*XMIN*W*AK1Z
      IF(AIMAG(PH).GT.PHMAX)PH=(1.,0.)*REAL(PH)+(0.,1.)*PHMAX
```

Table D1 (cont'd.)

```
      IF(AIMAG(PH).GT.PHMAX)PH=(1.,0.)*REAL(PH)+(0.,1.)*PHMAX
      COSPH=CCOS(PH)
      IF(COSPH.EQ.(0.,0.))GO TO 13
      TANPH=CSIN(PH)/COSPH
      ZN=Z1*(ZN-(0.,1.)*Z1*TANPH)/(Z1-(0.,1.)*ZN*TANPH)
      GO TO 14
   13 ZN=Z1*Z1/ZN
   14 CONTINUE
      GO TO 20
   17 XMIN1=XMIN
      CALL SOLIDUS(ZN1,ATAL,U,V,W4)
      ZN=ZN1
      ZI=ZN
   20 CONTINUE
      DO 2 L=1,N
      DI=(XMAX+4.-XMIN)/N
      D=DI*(2.*L-1.)/2.
      PI=PO*(1.+AX/((D+XMIN)**BX))
      CI=-44173.+468509.*PI
      GO TO (9,10),JFLAG
    9 VI=V1*(PI/PO-1.)
   10 CONTINUE
      AKI=(1.-(0.,1.)*VI)*(CI**2)
      AKI=1./AKI
      AKIZ=CSQRT(AKI-AKX2)
      IF(AKIZ.EQ.(0.,0.))GO TO 21
      Z1=ZI
      ZI=PI/AKIZ
      GO TO 22
   21 Z1=ZI
      ZI=(1.E50,1.E50)
   22 CONTINUE
      IF(KFLAG.EQ.2.AND.L.EQ.1)GO TO 23
      EXPH=CEXP((0.,1.)*PH)
      AL=AL*EXPH*(ZN+Z1)/(ZN+ZI)
      GO TO 24
   23 AL=(1.,0.)
      P2=PI
      R2=(ZN-ZI)/(ZN+ZI)
      AK2Z=AKIZ
   24 CONTINUE
      PH=10.*W*AKIZ*DI
      IF(AIMAG(PH).GT.PHMAX)PH=(1.,0.)*REAL(PH)+(0.,1.)*PHMAX
      COSPH=CCOS(PH)
      IF(COSPH.EQ.(0.,0.))GO TO 15
      TANPH=CSIN(PH)/COSPH
      ZN=ZI*(ZN-(0.,1.)*ZI*TANPH)/(ZI-(0.,1.)*ZN*TANPH)
      GO TO 2
      15 ZN=ZI*ZI/ZN
    2 CONTINUE
      EXPH=CEXP((0.,1.)*PH)
      AL=AL*EXPH*(ZN+ZI)/(ZN+ZO)
```

Table D1 (cont'd.)

```
      GO TO 4
    7 CONTINUE
      AL=2.*ZSL/(ZN+ZO)
      GO TO 4
    3 R=(1.,0.)
      AL=(0.,0.)
      GO TO 5
    4 CONTINUE
      R=(ZN-ZO)/(ZN+ZO)
      AL=AL*PO/PS
    5 CONTINUE
      IF(KFLAG.EQ.2)GO TO 25
      TR(K)=1.-R*CONJG(R)
      AL=AL*AKSLZ/AKOZ
      TL(K)=AL*CONJG(AL)*RZN/RZO
      GO TO 26
   25 TR(K)=1.-R*CONJG(R)
      XMIN=XMIN1
      IF(W4.EQ.(0.,0.))GO TO 27
      AL=AL*PS/P2
      V2Z=(0.,1.)*AK2Z*AL*(1.-R2)
      AL=V2Z/W4
      AT=AL*ATAL
      FLUXSL=(U(1)*AL+V(1)*AT)*CONJG(U(4)*AL+V(4)*AT)
      FLUXST=(U(3)*AL+V(3)*AT)*CONJG(U(2)*AL+V(2)*AT)
      FLUXI=PO*CONJG(AKOZ)
      TL(K)=REAL(FLUXSL+FLUXST)/REAL(FLUXI)
      GO TO 26
   27 TL(K)=TR(K)
   26 CONTINUE
    1 CONTINUE
      RETURN
      END


      SUBROUTINE SOLIDUS(ZN1,ATAL,U,V,W4)
      COMMON PO,CO,VO,P1,C1,C1T,V1,V1T,PS,CSL,CST,VSL,VST
      COMMON/X/AKO,AKO2,AK12,AKSL2,AKST,AKST2
      COMMON/Y/VI,W,N
      COMMON/VECTOR/AKSLZ,AKSTZ,AKX,AKX2,AK1Z
      COMMON/TRIGF/S2GST,C2GST
      COMMON/DENSE/AX,BX,XMIN,XMAX
      COMMON/XZV/LFLAG,XMAXV,NV
      COMMON/SAVE/PHMAX,QHMAX
      COMMON/VINS/P1S,V1S,XMINS
      TYPE COMPLEX AKO,AKO2,AK12,AKSL2,AKST,AKST2
      TYPE COMPLEX AKSLZ,AKSTZ,AKX,AKX2,AK1Z
      TYPE COMPLEX S2GST,C2GST,SG1,CG1,SG12,S2G1,S2G12,C2G1,C2G12
      TYPE COMPLEX ZN1,ATAL,ANUM,ADEN,AK1T,AK1T2,AK1TZ
      TYPE COMPLEX QH,PH,SINQH,COSQH,SINPH,COSPH,SINQHB,SINPHA
      TYPE COMPLEX A,U,V,W1,W4
      DIMENSION A(4,4),U(4),V(4)
```

Table D1 (cont'd.)

```
      P11=P1 $ P1=P1S $ V1T1=V1T $ V1T=V1S $ XMIN1=XMIN $ XMIN=XMINS
      AK1T=(1.+(0.,1.)*V1T)/C1T
      AK1T2=AK1T**2
      AK1TZ=CSQRT(AK1T2-AKX2)
      SG1=AKX/AK1T
      CG1=AK1TZ/AK1T
      SG12=SG1**2
      C2G1=1.-2.*SG12
      S2G1=2.*SG1*CG1
      C2G12=C2G1**2
      S2G12=1.-C2G12
      PH=10.*W*AK1Z*XMIN
      IF(AIMAG(PH).GT.PHMAX)PH=(1.,0.)*REAL(PH)+(0.,1.)*PHMAX
      SINPH=CSIN(PH)
      COSPH=CCOS(PH)
      IF(PH.EQ.(0.,0.))GO TO 5
      SINPHA=SINPH/AK1Z
      GO TO 6
    5 SINPHA=10.*W*XMIN*(1.,0.)
    6 CONTINUE
      QH=10.*W*AK1TZ*XMIN
      IF(AIMAG(QH).GT.QHMAX)QH=(1.,0.)*REAL(QH)+(0.,1.)*QHMAX
      SINQH=CSIN(QH)
      COSQH=CCOS(QH)
      IF(QH.EQ.(0.,0.))GO TO 7
      SINQHB=SINQH/AK1TZ
      GO TO 8
    7 SINQHB=10.*W*XMIN*(1.,0.)
    8 CONTINUE
      A(1,1)=C2G1*COSPH+2.*SG12*COSQH
      A(1,2)=2.*P1*SG1*C2G1*(COSPH-COSQH)/AK1T
      A(1,3)=(0.,1.)*(S2G1*SINQH-AKX*C2G1*SINPHA)
      A(1,4)=-(0.,1.)*P1*(C2G12*SINPHA+S2G12*SINQHB)
      A(2,1)=AKX*(COSPH-COSQH)/P1
      A(2,2)=2.*SG12*COSPH+C2G1*COSQH
      A(2,3)=-(0.,1.)*(AKX2*SINPHA+AK1TZ*SINQH)/P1
      A(2,4)=(0.,1.)*(S2G1*SINQH-AKX*C2G1*SINPHA)
      A(3,1)=(0.,1.)*AKX*(C2G1*SINQHB-2.*AK1Z*SINPH/AK1T2)
      A(3,2)=-(0.,1.)*P1*(4.*AK1Z*SG12*SINPH/AK1T2+C2G12*SINQHB)
      A(3,3)=2.*SG12*COSPH+C2G1*COSQH
      A(3,4)=2.*P1*SG1*C2G1*(COSPH-COSQH)/AK1T
      A(4,1)=-(0.,1.)*(AK1Z*SINPH+AKX2*SINQHB)/P1
      A(4,2)=(0.,1.)*AKX*(C2G1*SINQHB-2.*AK1Z*SINPH/AK1T2)
      A(4,3)=AKX*(COSPH-COSQH)/P1
      A(4,4)=C2G1*COSPH+2.*SG12*COSQH
      IF(NV.EQ.0)GO TO 13
      POV=PO
      V1V=V1
      CALL VISCUS(POV,V1V,A)
      XMIN1=XMAXV
   13 CONTINUE
      U(1)=(0.,1.)*PS*C2GST
```

Table D1 (cont'd.)

```
      U(2)=(0.,1.)*AKX
      U(3)=2.*(0.,1.)*PS*AKSLZ*AKX/AKST2
      U(4)=(0.,1.)*AKSLZ
      V(1)=(0.,1.)*PS*S2GST
      V(2)=-(0.,1.)*AKSTZ
      V(3)=-(0.,1.)*PS*C2GST
      V(4)=(0.,1.)*AKX
      ANUM=(0.,0.)
      ADEN=(0.,0.)
      DO 1 I=1,4
      ANUM=ANUM+A(3,I)*U(I)
    1 ADEN=ADEN+A(3,I)V(I)
      IF(ADEN.EQ.(0.,0.))GO TO 9
      ATAL=-ANUM/ADEN
      W1=(0.,0.)
      W4=(0.,0.)
      DO 2 I=1,4
      W1=W1+A(1,I)*(U(I)+V(I)*ATAL)
    2 W4=W4+A(4,I)*(U(I)+V(I)*ATAL)
      GO TO 10
    9 CONTINUE
      W1=(0.,0.)
      W4=(0.,0.)
      DO 3 I=1,4
      W1=W1+A(1,I)*V(I)
    3 W4=W4+A(4,I)*V(I)
   10 IF(W4.EQ.(0.,0.))GO TO 11
      ZN1=W1/W4
      GO TO 12
   11 ZN1=(1.E50,1.E50)
   12 CONTINUE
      P1=P11 $ V1T=V1T1 $ XMIN=XMIN1
      RETURN
      END


      SUBROUTINE VISCUS(POV,V1V,A)
      COMMON/Y/VI,W,N
      COMMON/XZV/LFLAG,XMAXV,NV
      COMMON/VECTOR/AKSLZZ,AKSTZZ,AKX,AKX2,AK1ZZ
      COMMON/DENSE/AX,BX,XMIN,XMAX
      COMMON/SAVE/PHMAX,QHMAX
      COMMON/VINS/P1S,V1S,XMINS
      COMMON/VINH/P1H
      TYPE COMPLEX AKX,AKX2
      TYPE COMPLEX AKSLZZ,AKSTZZ,AK1ZZ
      TYPE COMPLEX AK12,AK1T,AK1T2,AK1Z,AK1TZ
      TYPE COMPLEX SG1,CG1,CG12,S2G1,S2G12,C2G1,C2G12
      TYPE COMPLEX QH,PH,SINQH,COSQH,SINPH,COSPH,SINQHB,SINPHA
      TYPE COMPLEX A,B,C
      DIMENSION A(4,4),B(4,4),C(4,4)
  100 FORMAT (1I5)
```

Table D1 (cont'd.)

```
101 FORMAT(5E15.5)
    DO 2 L=1,NV
    DO 1 I=1,4
    DO 1 J=1,4
  1 B(I,J)=A(I,J)
    D1=(XMAXV-XMIN)/NV
    D=D1*(2.*L-1.)/2.
    P1=POV*(1.+AX/((D+XMIN)**BX))
    IF(P1S.NE.P1H)P1=P1H
    V1=V1V*(P1/POV-1.)
    C1=-72437.+637606.*P1
    IF(LFLAG.EQ.2)C1=-44173.+468509.*P1
    AK12=(1.-(0.,1.)*V1)*(C1**2)
    AK12=1./AK12
    GO TO (3,4),LFLAG
  3 C1T=.5*C1
    V1T=V1
    AK1T2=(1.-(0.,1.)*V1T)*(C1T**2)
    AK1T2=1./AK1T2
    AK1T=CSQRT(AK1T2)
    GO TO 5
  4 C1T=C1*(SQRT(1.5*V1)+.0001)
    AK1T=(1.+(0.,1.))/C1T
    AK1T2=AK1T**2
  5 CONTINUE
    AK1Z=CSQRT(AK12-AKX2)
    AK1TZ=CSQRT(AK1T2-AKX2)
    SG1=AKX/AK1T
    CG1=AK1TZ/AK1T
    SG12=SG1**2
    C2G1=1.-2.*SG12
    S2G1=2.*SG1*CG1
    C2G12=C2G1**2
    S2G12=1.-C2G12
    PH=10.*W*AK1Z*D1
    IF(AIMAG(PH).GT.PHMAX)PH=(1.,0.)*REAL(PH)+(0.,1.)*PHMAX
    SINPH=CSIN(PH)
    COSPH=CCOS(PH)
    IF(PH.EQ.(0.,0.))GO TO 15
    SINPHA=SINPH/AK1Z
    GO TO 16
 15 SINPHA=10.*W*D1*(1.,0.)
 16 CONTINUE
    QH=10.*W*AK1TZ*D1
    IF(AIMAG(QH).GT.QHMAX)QH=(1.,0.)*REAL(QH)+(0.,1.)*QHMAX
    SINQH=CSIN(QH)
    COSQH=CCOS(QH)
    IF(QH.EQ.(0.,0.))GO TO 17
    SINQHB=SINQH/AK1TZ
    GO TO 8
 17 SINQHB=10.*W*D1*(1.,0.)
  8 CONTINUE
```

Table D1 (cont'd.)

```
      A(1,1)=C2G1*COSPH+2,*SG12*COSQH
      A(1,2)=2.*P1*SG1*C2G1*(COSPH-COSQH)/AK1T
      A(1,3)=(0.,1.)*(S2G1*SINQH-AKX*C2G1*SINPHA)
      A(1,4)=-0.,1.)*P1*(C2G12*SINPHA+S2G12*SINQHB)
      A(2,1)=AKX*(COSPH-COSQH)/P1
      A(2,2)=2.*SG12*COSPH+C2G1*COSQH
      A(2,3)=-(0.,1.)*(AKX2*SINPHA+AK1TZ*SINQH)/P1
      A(2,4)=(0.,1.)*(S2G1*SINQH-AKX*C2G1*SINPHA)
      A(3,1)=(0.,1.)*AKX*(C2G1*SINQHB-2.*AK1Z*SINPH/AK1T2)
      A(3,2)=-(0.,1.)*P1*(4.*AK1Z*SG12*SINPH/AK1T2+C2G12*SINQHB)
      A(3,3)=2.*SG12*COSPH+C2G1*COSQH
      A(3,4)=2.*P1*SG1*C2G1*(COSPH-COSQH)/AK1T
      A(4,1)=-(0.,1.)*(AK1Z*SINPH+AKX2*SINQHB)/P1
      A(4,2)=(0.,1.)*AKX*(C2G1*SINQHB-2.*AK1Z*SINPH/AK1T2)
      A(4,3)=AKX*(COSPH-COSQH)/P1
      A(4,4)=C2G1*COSPH+2.*SG12*COSQH
      DO 6 I=1,4
      DO 6 J=1,4
      C(I,J)=(0.,0.)
      DO 6K=1,4
    6 C(I,J)=C(I,J)+A(I,K)*B(K,J)
      DO 7 I=1,4
      DO 7 J=1,4
    7 A(I,J)=C(I,J)
    2 CONTINUE
      XMIN=XMAXV
      RETURN
      END


      SUBROUTINE SUM(HK,HKS)
      COMMON/Y/VI,W,N
      COMMON//Z/ THO,DTH
      COMMON/XY/ERROR1,DTH1,DTH2,LAST,LAST1,LAST2
      COMMON/TOSUM2/TRSCTHO,TLSCTHO,THO1,TRW1,TRWS1
      DIMENSION STHO(64),CTHO(64),TR(64),TL(64)
  100 FORMAT(3F7.3,5E15.5)
  101 FORMAT(3I7,5E15.5)
  102 FORMAT (1I5,5E15.5)
      THO1=0.
      TRW=0.
      TRWS=0.
      TRSCTHO=0.
      TLSCTHO=0.
      DO 4 J=1,LAST1
      M=1
      IF(J.EQ.1)M=2
      NI=0
      DTH=DTH1
      THO=THO1
      IF(J.EQ.1)THO=THO1-DTH
      CALL CONST(M,STHO,CTHO,TR,TL)
```

Table D1 (cont'd.)

```
      AREA=0.
      AREAS=0.
      DO 1 K=1,M
      SCTHO=STHO(K)*CTHO(K)
      AREA=AREA+.5*(TR(K)*SCTHO+TRSCTHO)
    1 AREAS=AREAS+.5*(TL(K)*SCTHO+TLSCTHO)
      TRSCTHO+TR(M)*SCTHO
      TLSCTHO+TL(M)*SCTHO
      THO1=THO
      THO=THO-DTH
      DTH=2.*DTH
    3 NI=NI+1
      DTH=DTH/2.
      M=(2**NI)/2
      IF(M.EQ.128)GO TO 9
      THO=THO-M*DTH+DTH/2.
      AREA1=.5*AREA
      AREAS1=.5*AREAS
      CALL CONST(M,STHO,CTHO,TR,TL)
      DO 2 K=1,M
      SCTHO=STHO(K)*CTHO(K)
      AREAS1=AREAS1+TL(K)*SCTHO/(2.**NI)
    2 AREA1=AREA1+TR(K)*SCTHO/(2.**NI)
      DAREA=(AREA1-AREA)/AREA
      DAREAS=(AREAS1-AREAS)/AREAS
      AREA=AREA1
      AREAS=AREAS1
      ERROR=ERROR1*TRW/((LAST+1-J)*AREA)
      ERRORS=ERROR1*TRWS/((LAST+1-J)*AREAS)
      IF(ERROR.LT.ERROR1)ERROR=ERROR1
      IF(ERRORS.LT.ETTOR1)ERRORS=ERROR1
      IF(ABS(DAREA).GT.ERROR)3,9
    9 CONTINUE
      TRW=TRW+AREA
      TRWS+TRWS+AREAS
    4 CONTINUE
      TRW=TRW*DTH1
      TRWS=TRWS*DTH1
      PRINT 102,N,W,TRW,TRWS
      TRW1=TRW/DTH2
      TRWS1=TRWS/DTH2
      CALL SUM2(TRW2,TRWS2)
      HK=TRW+TRW2
      HKS=TRWS+TRWS2
      RETURN
      END


      SUBROUTINE SUM2(TRW2,TRWS2)
      COMMON/Y/VI,W,N
      COMMON /Z/ THO,DTH
      COMMON/XY/ERROR1,DTH1,DTH2,LAST,LAST1,LAST2
```

Table D1 (cont'd.)

```
      COMMON/TOSUM2/TRSCTHO,TLSCTHO,THO1,TRW1,TRWS1
      DIMENSION STHO(64),CTHO(64),TR(64),TL(64)
  100 FORMAT(3F7,3,5E15.5)
  101 FORMAT(3I7,5E15.5)
  102 FORMAT(1I5,5E15.5)
      TRW=0.
      TRWS=0.
      DO 4 J=1,LAST2
      M=1
      NI=0
      DTH=DTH2
      THO=THO1
      CALL CONST(M,STHO,CTHO,TR,TL)
      SCTHO=STHO(M)*CTHO(M)
      AREA=.5*(TR(M)*SCTHO+TRSCTHO)
      AREAS=.5*(TL(M)*SCTHO+TLSCTHO)
      TRSCTHO=TR(M)*SCTHO
      TLSCTHO=TL(M)*SCTHO
      THO1=THO
      THO=THO-DTH
      DTH=2.*DTH
    3 NI=NI+1
      DTH=DTH/2.
      M=(2**NI)/2
      IF(M.EQ.128)GO TO 9
      THO=THO-M*DTH+DTH/2.
      AREA1=.5*AREA
      AREAS1=.5*AREAS
      CALL CONST(M,STHO,CTHO,TR,TL)
      DO 2 K=1,M
      SCTHO=STHO(K)*CTHO(K)
      AREAS1=AREAS1+TL(K)*SCTHO/(2.**NI)
    2 AREA1=AREA1+TR(K)*SCTHO/(2.**NI)
      DAREA=(AREA1-AREA)/AREA
      DAREAS=(AREAS1-AREAS)/AREAS
      AREA=AREA1
      AREAS=AREAS1
      ERROR=ERROR1*TRW1/((LAST2+1-J)*AREA)
      ERRORS=ERROR1*TRWS1/((LAST2+1-J)*AREAS)
      IF (ERROR.LT.ERROR1)ERROR=ERROR1
      IF(ERRORS.LT.ERROR1)ERRORS=ERROR1
      IF(ABS(DAREA).GT.ERROR)3,9
    9 CONTINUE
      TRW=TRW+AREA
      TRWS=TRWS+AREAS
      TRW1=TRW1+AREA
      TRWS1=TRWS1+AREAS
    4 CONTINUE
      TRW=TRW*DTH2
      TRWS=TRWS*DTH2
      TRW1=TRW1*DTH2
      TRWS1=TRWS1*DTH2
```

Table D1 (cont'd.)

```
      PRINT 102,N,W,TRW,TRWS
      PRINT 102,N,W,TRW1,TRWS1
      TRW2=TRW
      TRWS2=TRWS
      RETURN
      END


      SUBROUTINE SUMX(T,DX,ERRORA,ERRORF,FLUXT,FLUXTS)
  100 FORMAT(3I8,5E15.5)
  101 FORMAT(3F8,3,5E15.5)
  102 FORMAT(5E15.5)
      COMMON/TOCH/A
      L=0
      XL=0.
      HXL=0.
      HXLS=0.
      FLUXT=0.
      FLUXTS=0.
    3 M=0
      L=L+1
      XO=XL
      HXO=HXL
      HXOS=HXLS
      XL=XO+DX
      CALL CHOICE(XL,T,TRWS,TRWCS)
      EXL=EXP(XL)
      HXL=TRWC*(XL**4)*EXL/((1.-EXL)**2)
      HXLS=TRWCS*(XL**4)*EXL/((1.-EXL)**2)
      AREAO=.5*(HXO+HXL)
      AREAOS=.5*(HXOS+HXLS)
    2 SHX=0.
      SHXS=0.
      M=M+1
      N=(2**M)/2
      N2=2*N
      DO 1 I=1,N
      X=XO+(2*I-1)*DX/N2
      CALL CHOICE(X,T,TRWC,TRWCS)
      EX=EXP(X)
      HX=TRWC*(X**4)*EX/((L.-EX)**2)
      HXS=TRWCS*(X**4)*EX/((1.-EX)**2
      SHXS=SHXS+HXS
    1 SHX=SHX+HX
      AREA=.5*AREAO+SHX/N2
      AREAS=.5*AREAOS+SHXS/N2
      DAREA=ABS((AREA-AREAO)/AREAO)
      DAREAS=ABS((AREAS-AREAOS)/AREAOS)
      AREAO=AREA
      AREAOS=AREAS
      IF(DAREA.GT.ERRORA,OR.DAREAS.GT.ERRORA)GO TO 2
      FLUXT=FLUXT+AREA
      FLUXTS=FLUXTS+AREAS
```

Table D1 (cont'd.)

```
      DFLUX=AREA/FLUXT
      DFLUXS=AREAS/FLUXTS
      T1=A*T*X
      PRINT 100,L,M,N,T1,TRWC,FLUXT,AREA,DFLUX
      PRINT 101,XO,XL,X,T1,TRWCS,FLUXTS,AREAS,FLUXS
      IF(DFLUX.GT.ERRORF,OR.DFLUXS.GT.ERRORF)GO TO 3
      FLUXT=FLUXT*DX
      FLUXTS=FLUXTS*DX
      PRINT 102,T,FLUXT,FLUXTS
      RETURN
      END


      SUBROUTINE ARRAY(TMIN,TMAX)
      COMMON/Y/VI,W,N
      COMMON/TOARRAY/TM,TRW,DTRW,TRWS,DTRWS,NMAX,DELTA,ALPHA
      COMMON/LAYERS/NINF,NSUP
      COMMON/DENSE/AX,BX,XMIN,XMAX
      DIMENSION TM(200),TRW(200),DTRW(200),TRWS(200),DTRWS(200)
      I=1
      TM(1)=TMIN
      T=TM(1)
      N=1+(XMAX-XMIN+4.)*T/(10.*ALPHA)
      IF(N.LT.NINF)N=NINF
      IF(N.GT.NSUP)N=NSUP
      W=370.*T
      CALL SUM(HK,HKS)
      TRW(1)=HK
      TRWS(1)=HKS
    1 I=I+1
      TM(I)=(1.+DELTA)*TM(I-1)
      T=TM(I)
      DT=TM(I)-TM(I-1)
      N=1+(XMAX-XMIN+4.)*T/(10.*ALPHA)
      IF(N.LT.NINT)N=NINF
      IF(N.GT.NSUP)N=NSUP
      W=370.*T
      CALL SUM(HK,HKS)
      TRW(I)=HK
      TRWS(I)=HKS
      I1=I-1
      DTRW(I1)=(TRW(I)-TRW(I-1))/DT
      DTRWS(I1)=(TRWS(I)-TRWS(I-1))/DT
      IF(T.LE.TMAX)GO TO 1
      DTRW(I)=DTRW(I-1)
      DTRWS(I)=DTRWS(I-1)
      NMAX=I
      RETURN
      END
```

APPENDIX E: ADDITIONAL FIGURES OF TR

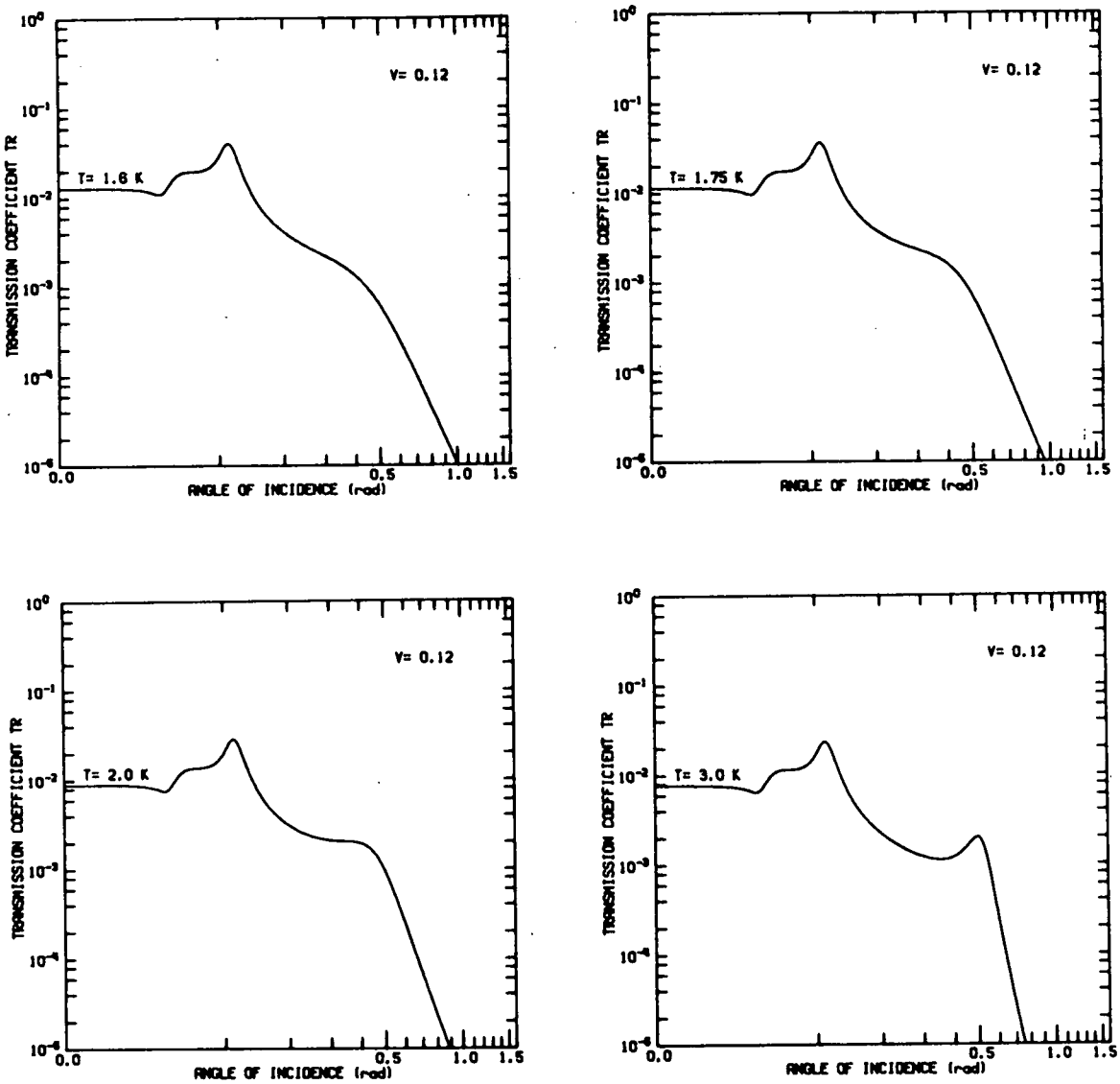

Figure E1: TR calculated at frequencies corresponding to the temperatures; 1.6, 1.75, 2.0 and 3.0 K. Only longitudinal waves are included in the first He layer.

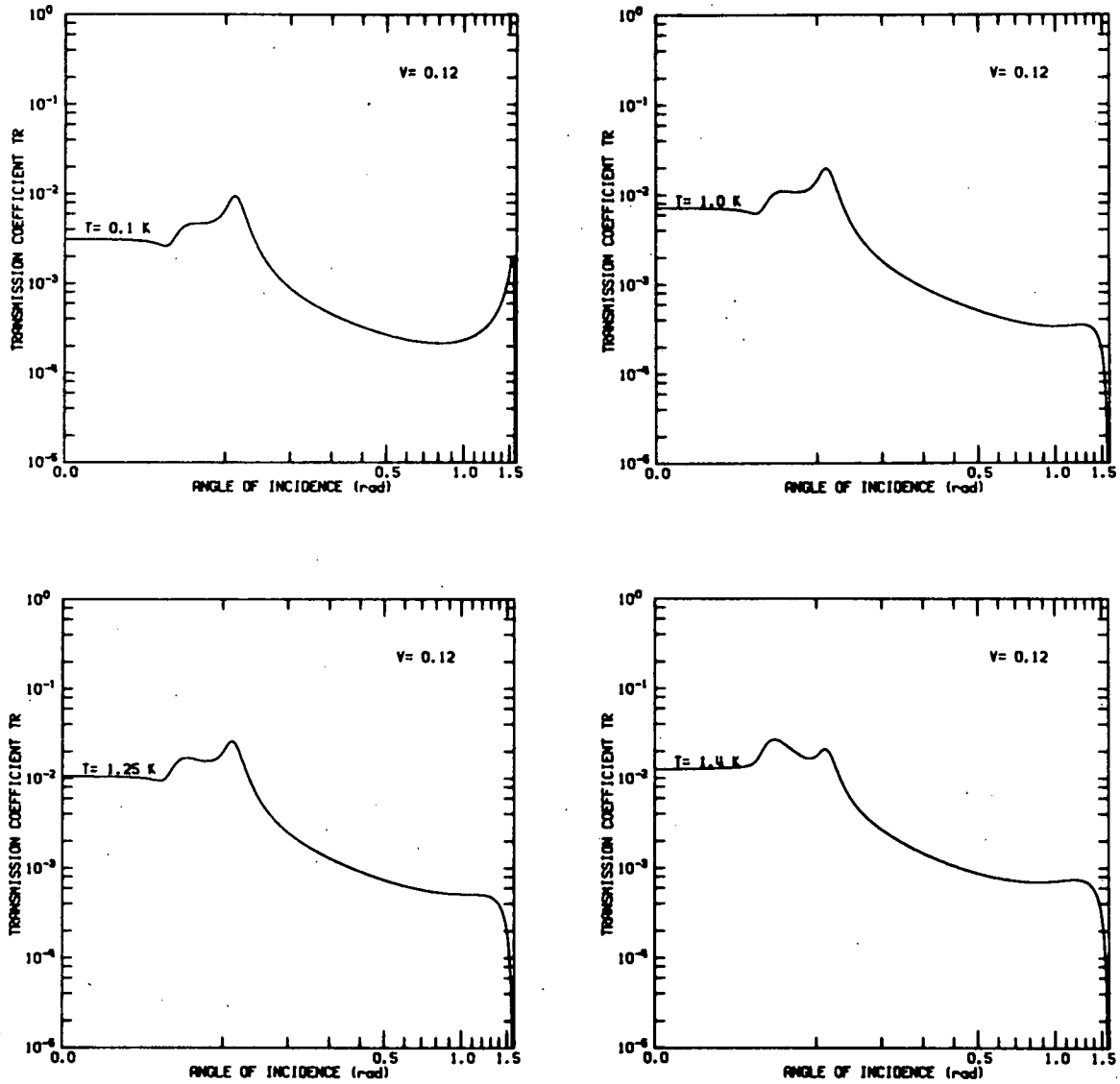

Figure E2: TR calculated at frequencies corresponding to the temperatures; 0.1, 1.0, 1.25 and 1.4 K.

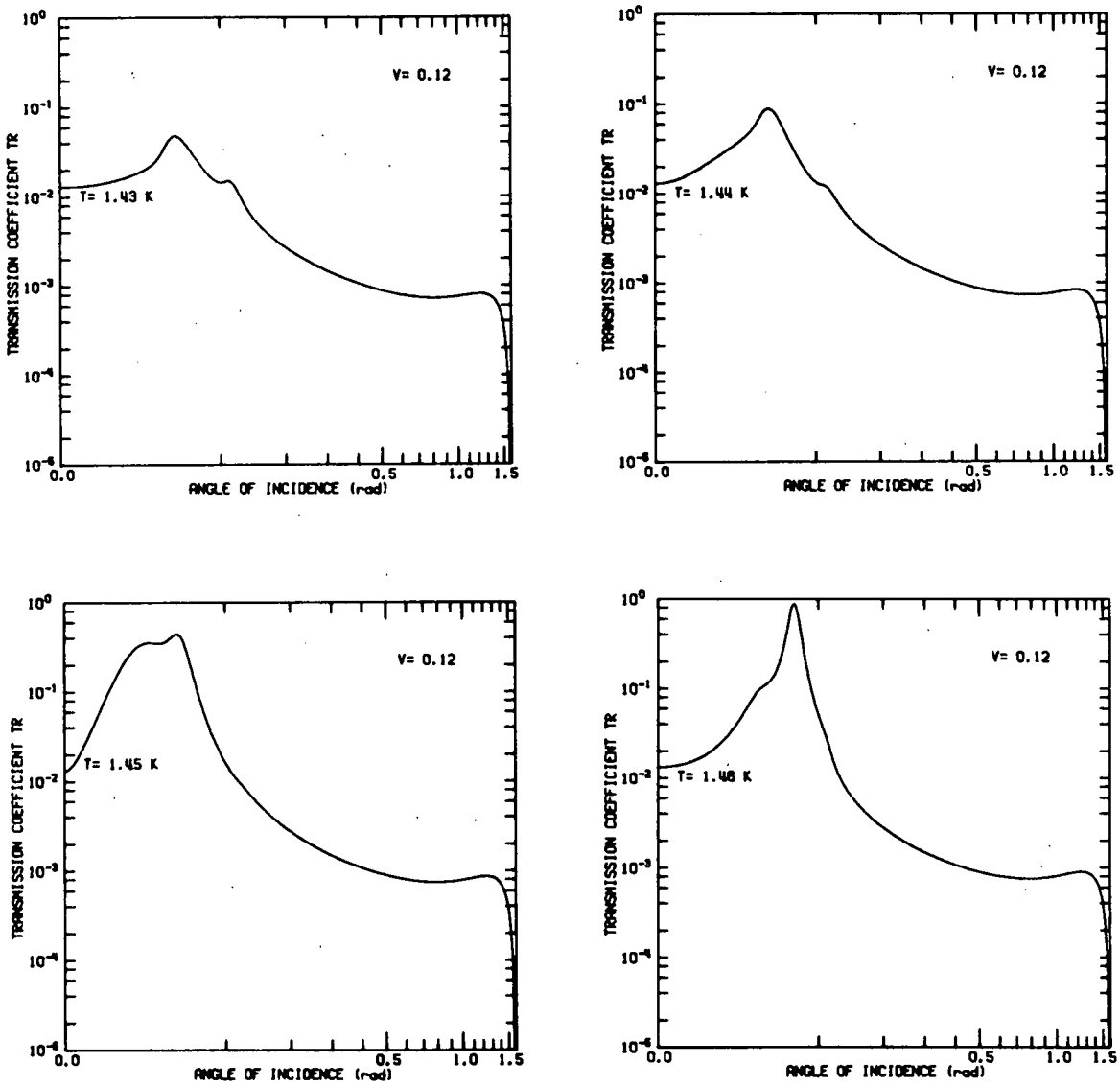

Figure E3: TR calculated at frequencies corresponding to the temperatures; 1.43, 1.44, 1.45, and 1.46 K.

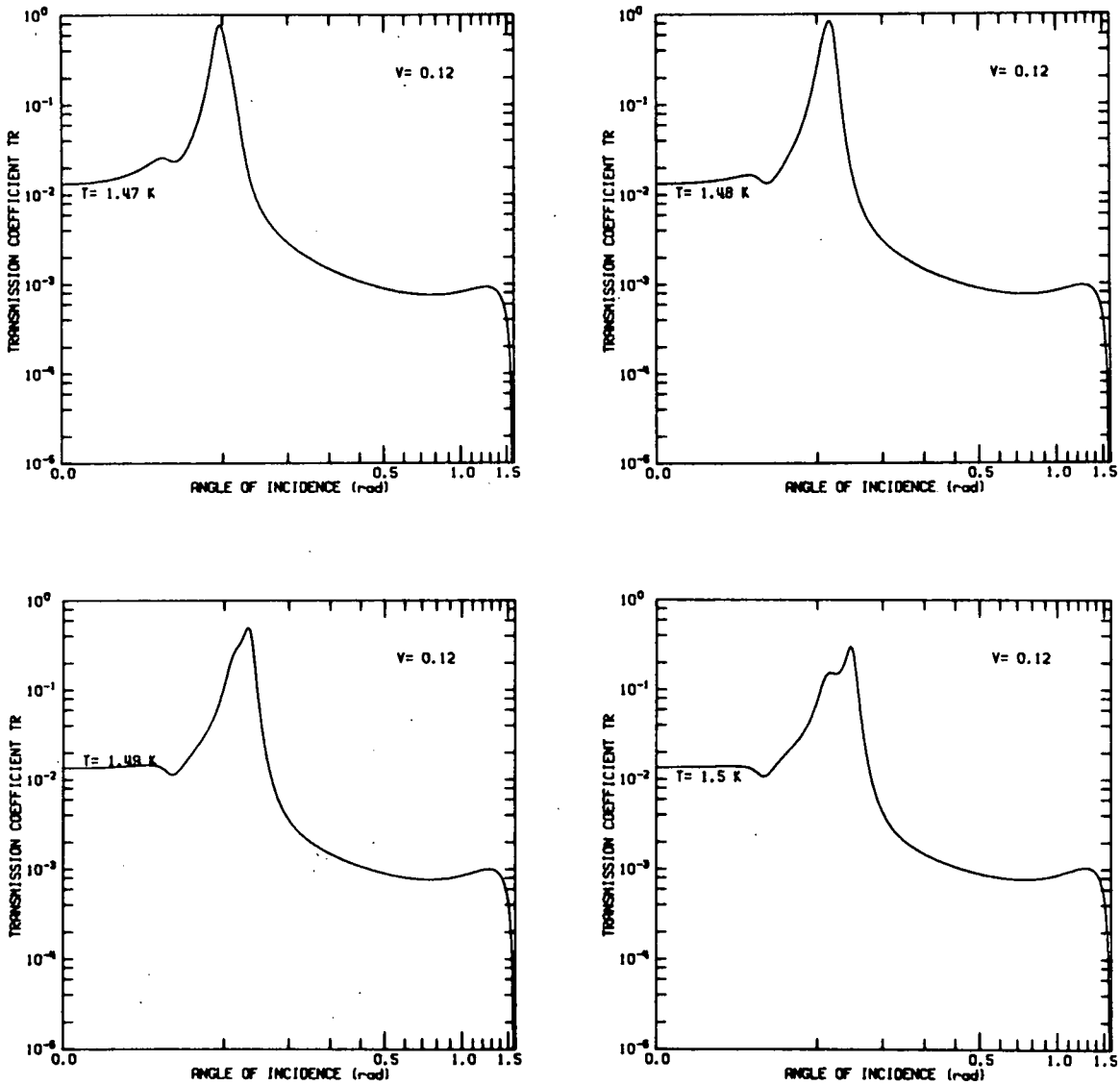

Figure E4: TR calculated at frequencies corresponding to the temperatures; 1.47, 1.48, 1.49, and 1.5 K.

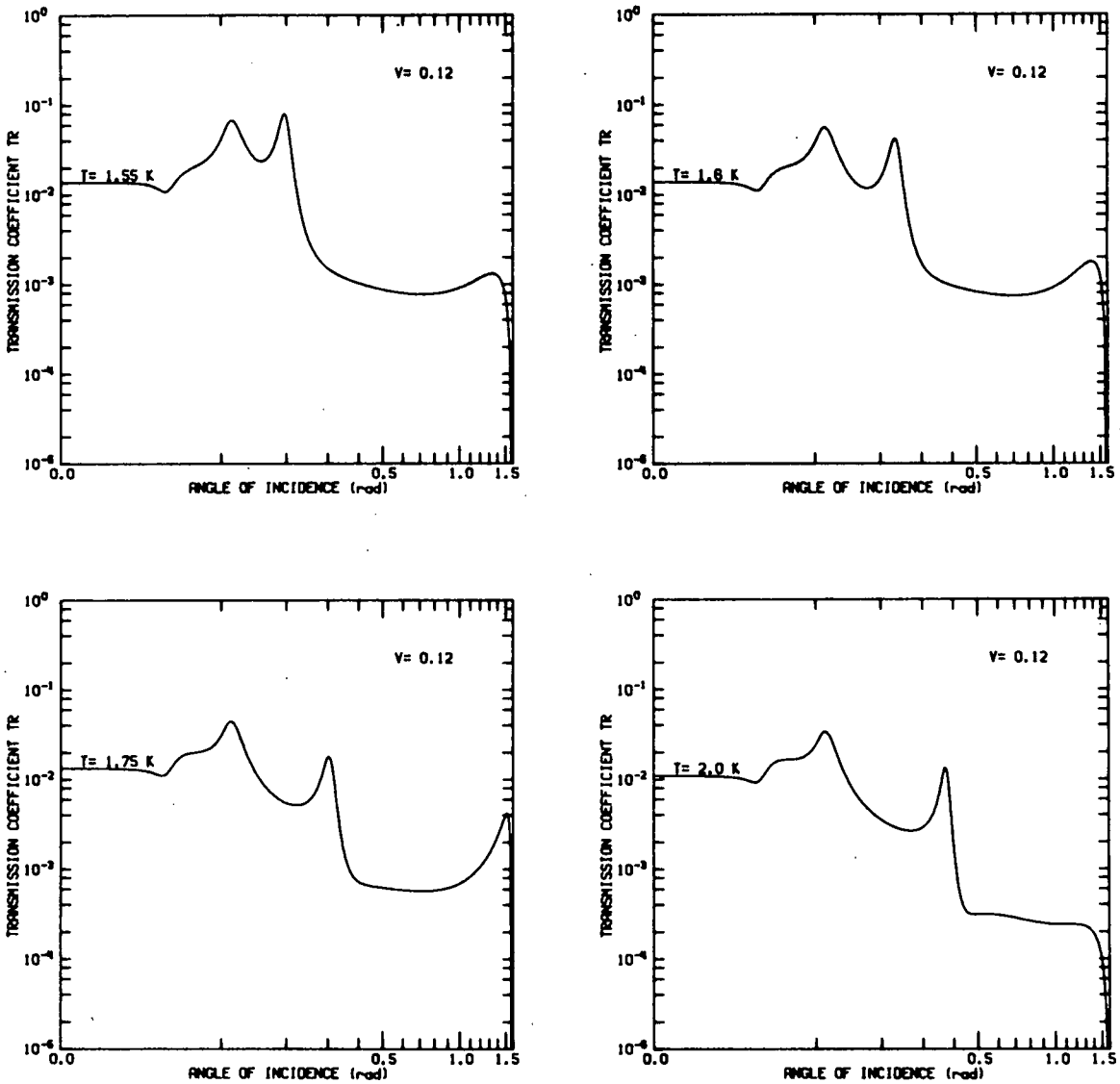

Figure E5: TR calculated at frequencies corresponding to the temperatures; 1.55, 1.6, 1.75, and 2.0 K.

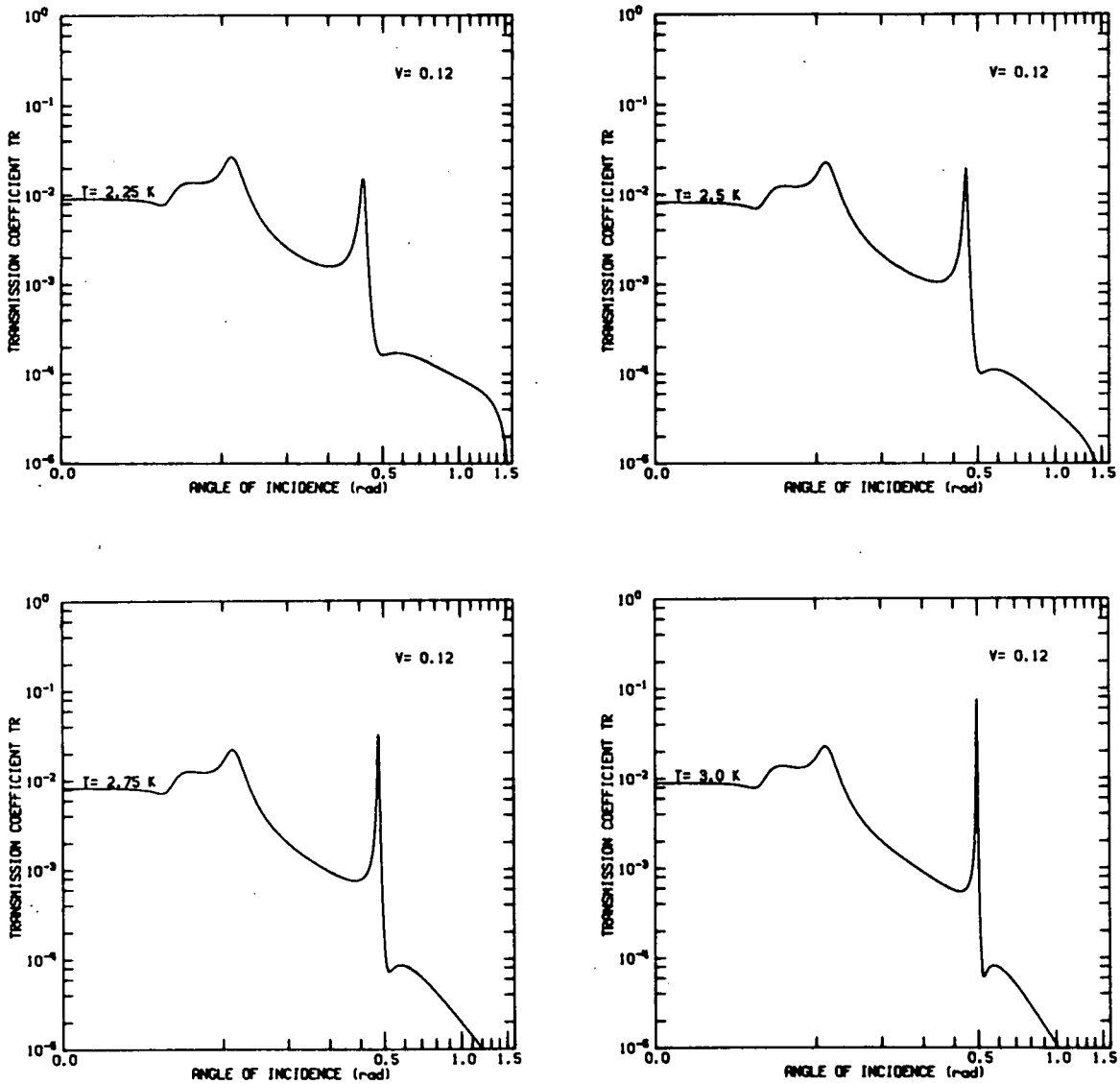

Figure E6: TR calculated at frequencies corresponding to the temperatures; 2.25, 2.5, 2.75, and 3.0 K.

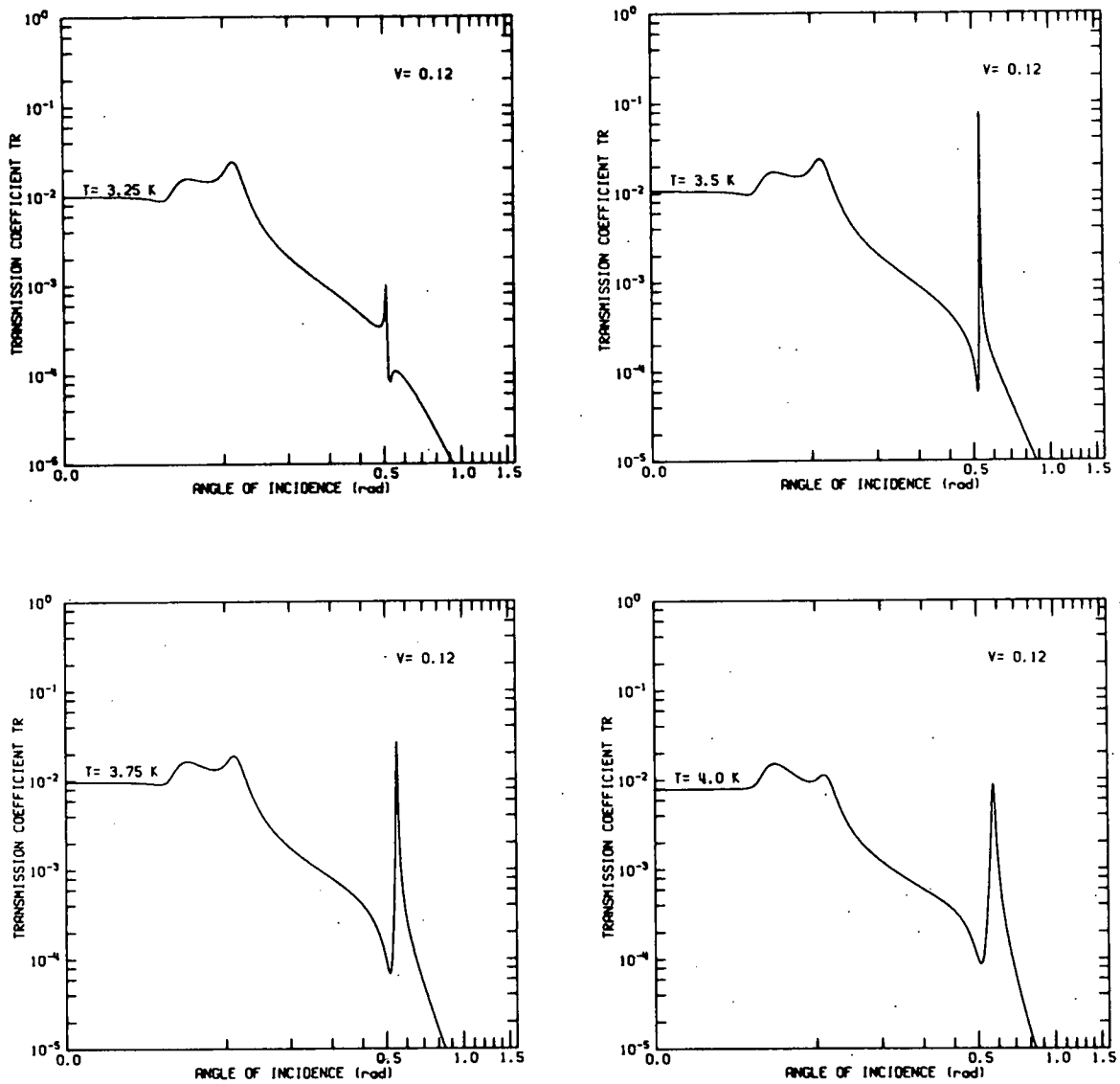

Figure E7: TR calculated at frequencies corresponding to the temperatures 3.25, 3.5, 3.75, and 4.0 K.

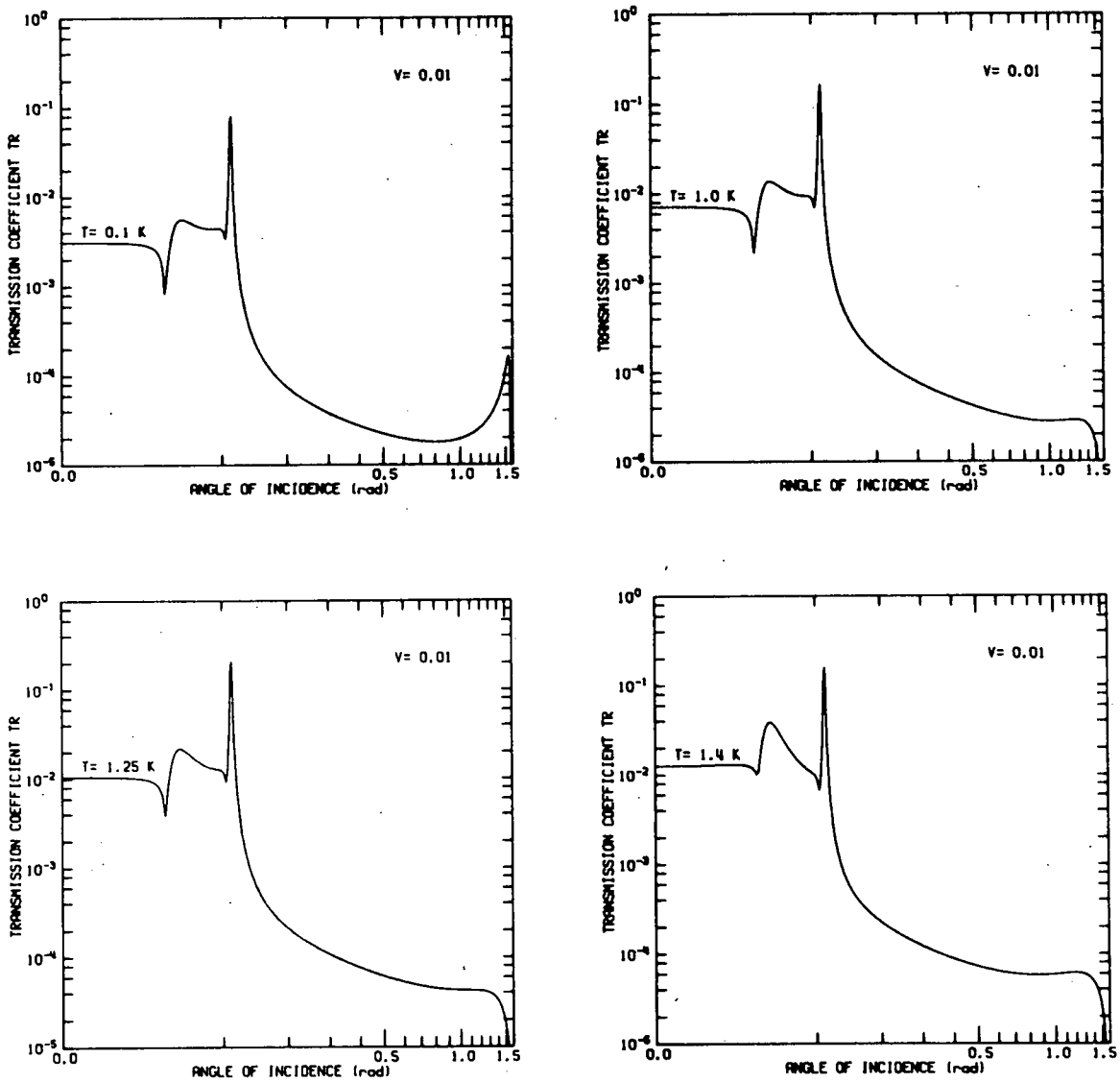

Figure E8: TR calculated for a small attenuation, V = 0.01, at frequencies corresponding to the temperatures; 0.1, 1.0, 1.25, and 1.4 K.

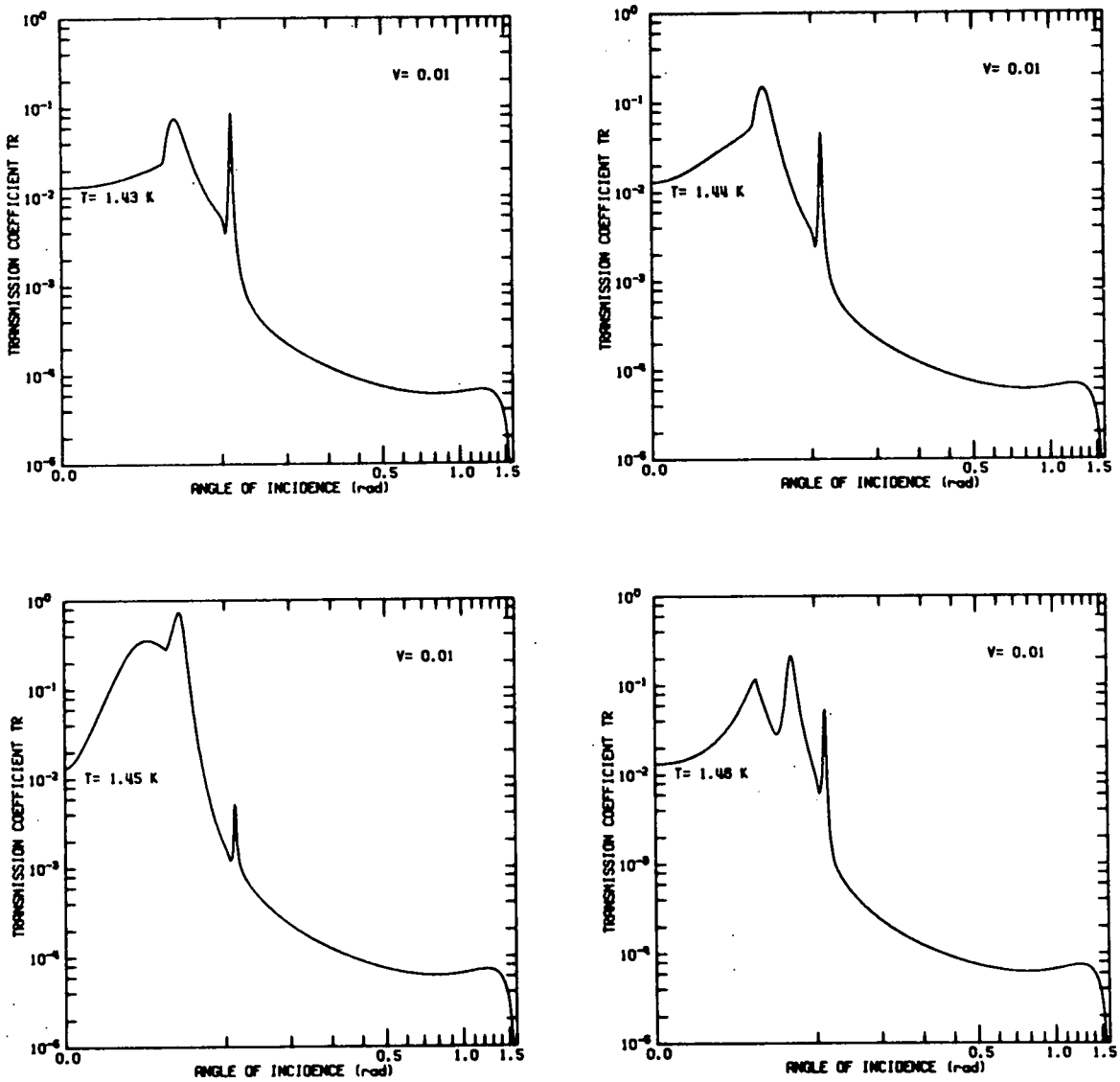

Figure E9: TR calculated for a small attenuation, V = 0.01, at frequencies corresponding to the temperatures; 1.43, 1.44, 1.45, and 1.46 K.

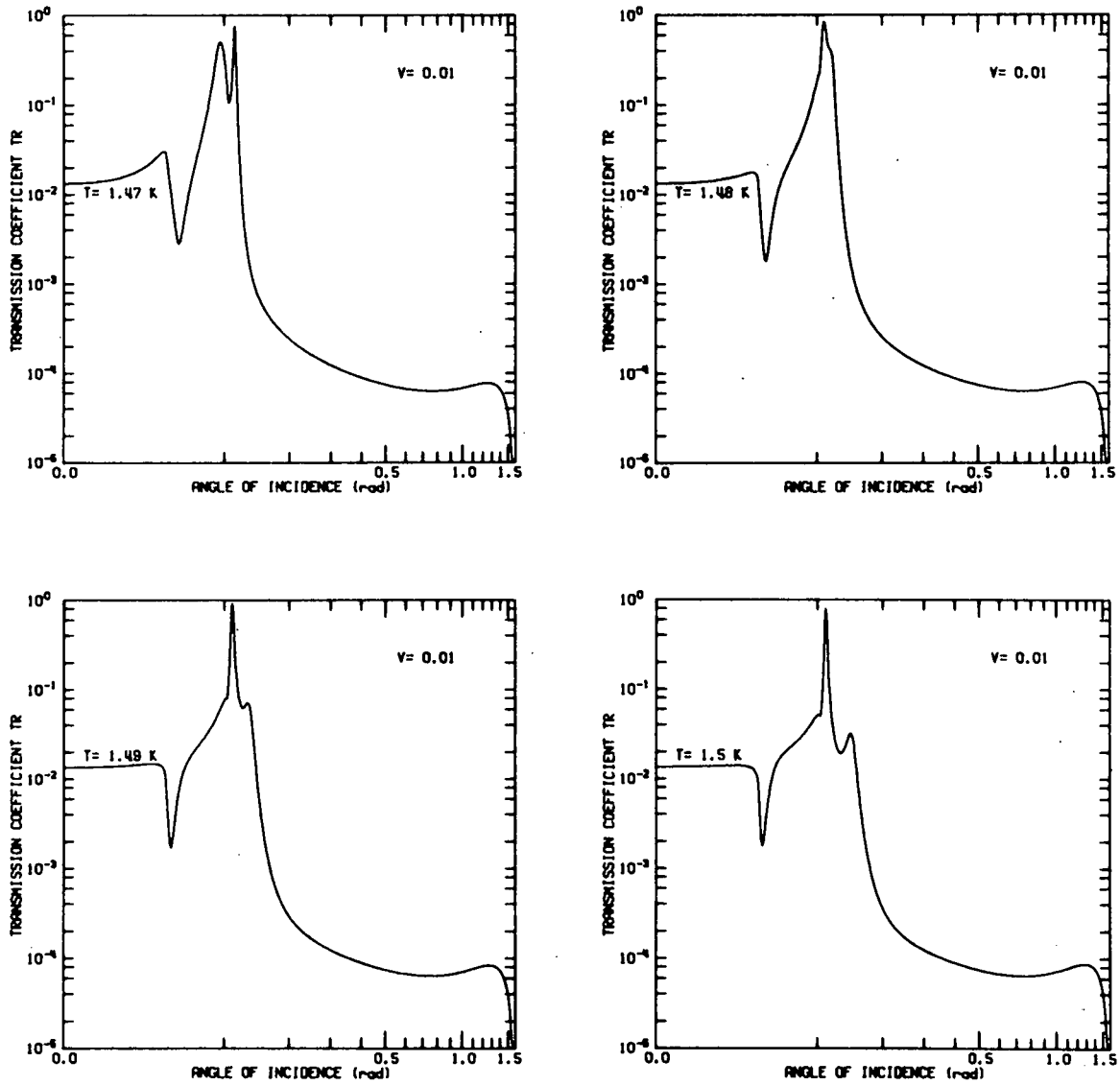

Figure E10: TR calculated for a small attenuation, V = 0.01, at frequencies corresponding to the temperatures; 1.47, 1.48, 1.49, and 1.5 K.

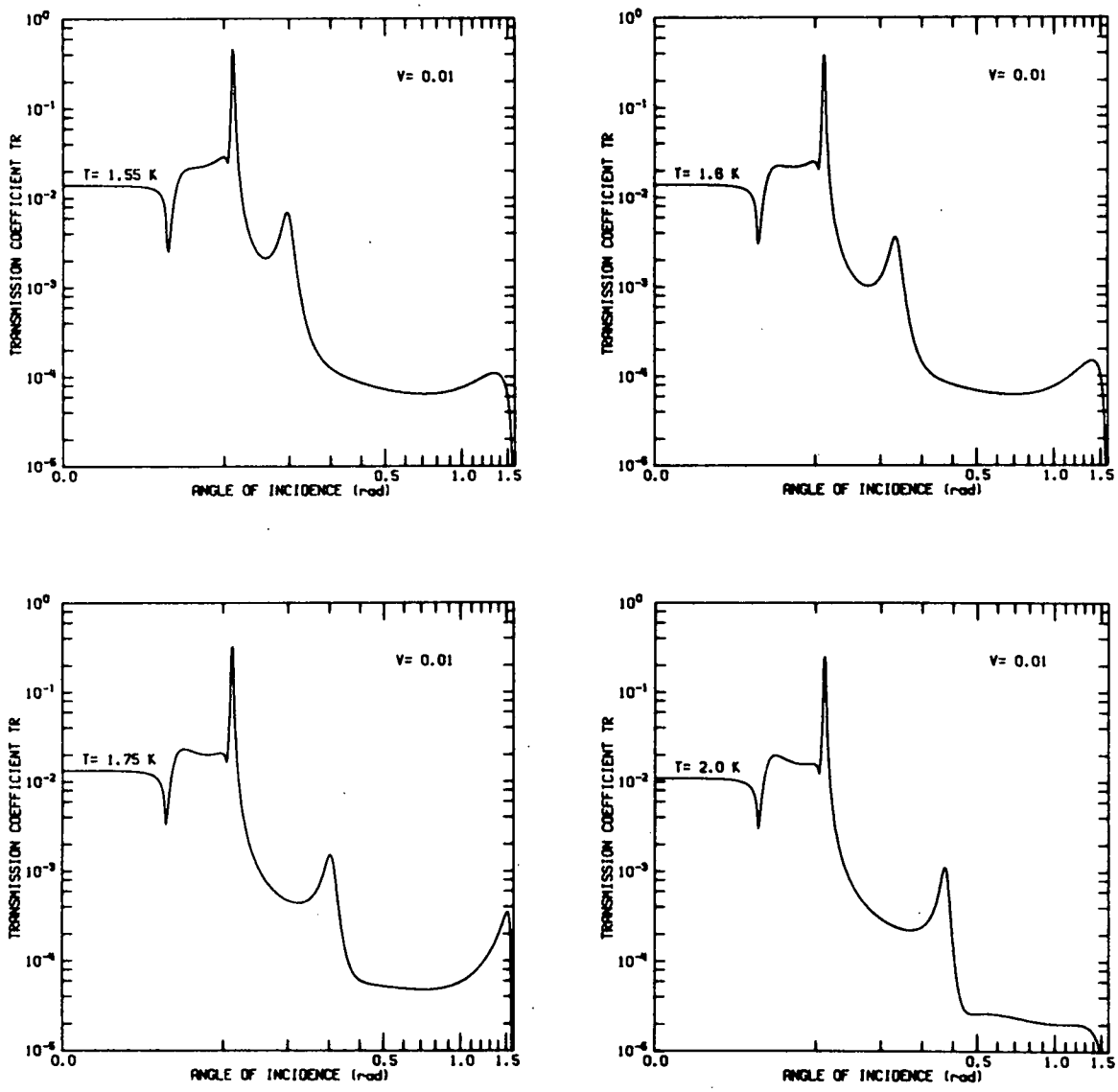

Figure E11: TR calculated for a small attenuation, V = 0.01, at frequencies corresponding to the temperatures; 1.55, 1.6, 1.75, and 2.0 K.

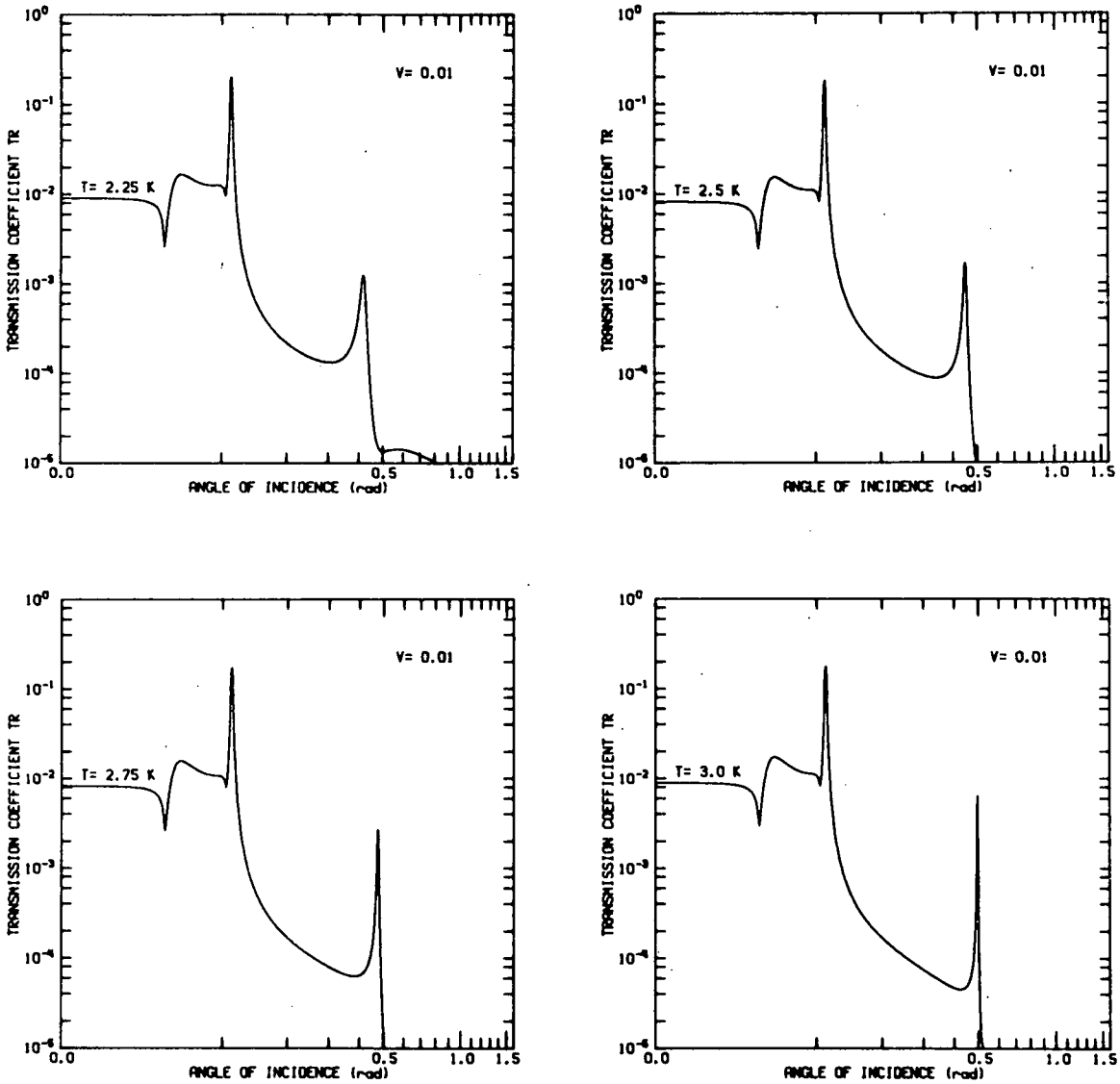

Figure E12: TR calculated for a small attenuation, V = 0.01, at frequencies corresponding to the temperatures; 2.25, 2.5, 2.75, and 3.0 K.

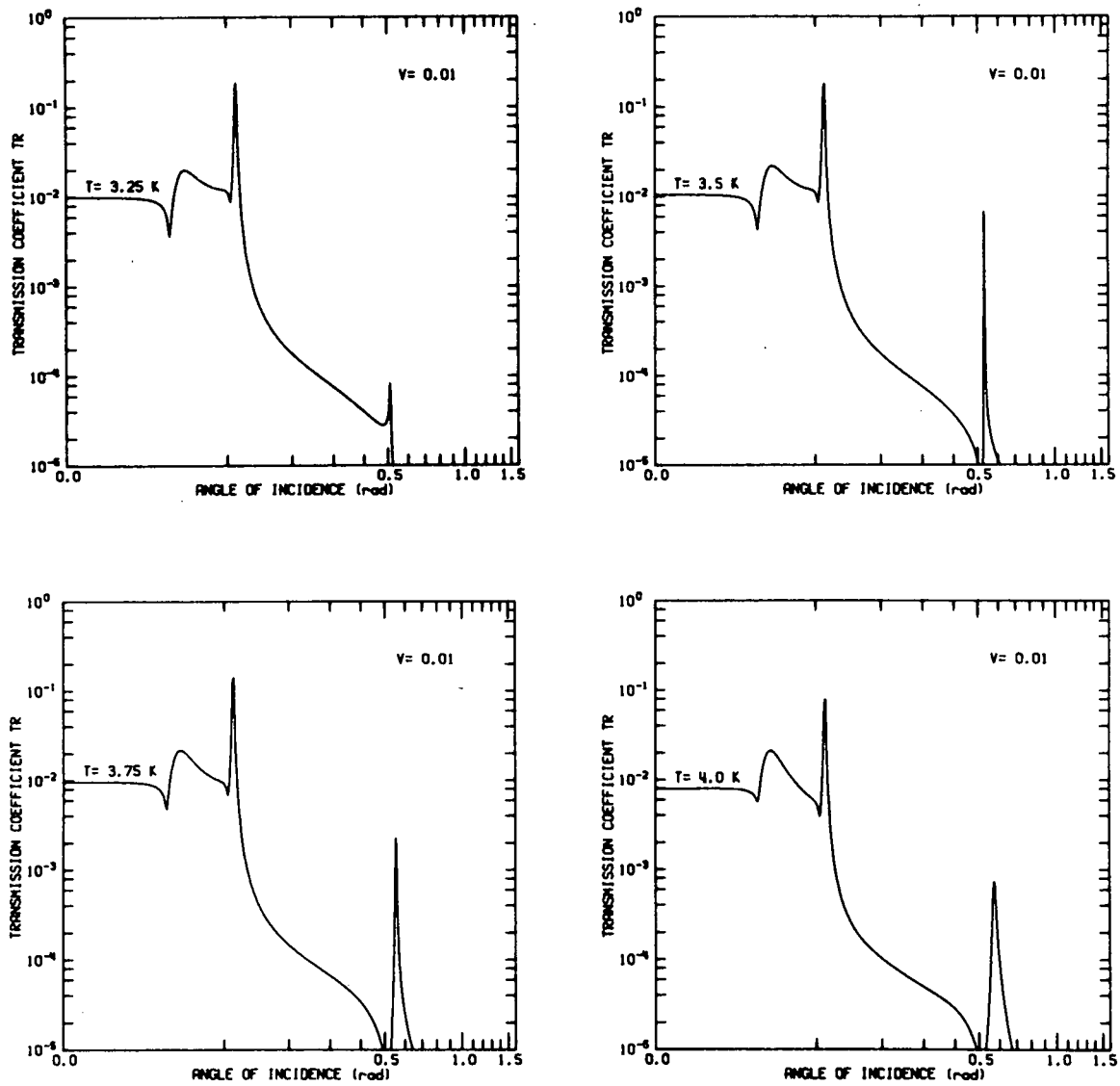

Figure E13: TR calculated for a small attenuation, V = 0.01, at frequencies corresponding to the temperatures; 3.25, 3.5, 3.75, and 4.0 K.

APPENDIX F: TABULATION OF CALCULATED $R_K T^3$ VALUES

TABLE F1

Kapitza resistance, R_K, in the form $R_K T^3$, as a function of phonon attenuation in the copper.

Loss Factor V	Kapitza Resistance x (Temperature)^3 $R_K T^3$ ($cm^2\ K^4/W$)
0.0	1270
0.001	540
0.002	501.9
0.003	480.6
0.004	465.2
0.005	452.1
0.006	440.7
0.007	430.4
0.008	420.6
0.009	411.6
0.01	401.8
0.02	334.3
0.03	287.2
0.04	250.8
0.05	223.4
0.06	201.4
0.07	183.2
0.08	168.3
0.09	155.8
0.10	145.0
0.11	135.5
0.12	127.2
0.13	119.9
0.14	113.4
0.15	107.6
0.16	102.4
0.17	97.6
0.18	93.3
0.19	89.4
0.20	85.8
0.21	82.5
0.22	79.4
0.23	76.6
0.24	74.0

Table F1 (cont'd.)

Loss Factor V	Kapitza Resistance x (Temperature)^3 $R_K T^3$ ($cm^2\ K^4/W$)
0.25	71.5
0.26	69.2
0.27	67.1
0.28	65.1
0.29	63.2
0.30	61.4
0.4	48.1
0.5	39.6
0.6	33.8
0.7	29.7
0.8	26.5
0.9	24.0
1.0	22.0

TABLE F2

Calculated $R_K T^3$ values used in Figure 8.

T(K)	$R_K T^3$ (cm^2 K^4/W) (upper curve)	(lower curve)
0.01	128.2	127.6
0.02	129.8	128.0
0.03	131.3	128.4
0.04	132.8	128.8
0.05	134.2	129.2
0.06	135.6	129.5
0.07	136.8	129.7
0.08	138.0	129.9
0.09	139.0	130.0
0.1	140.0	130.1
0.2	143.5	126.0
0.3	136.4	113.2
0.4	122.3	94.8
0.5	107.4	77.3
0.6	95.4	63.6
0.7	87.3	51.7
0.8	82.2	46.9
0.9	79.1	45.5
1.0	77.2	45.3
1.1	76.1	45.7
1.2	75.6	46.5
1.3	75.4	47.7
1.4	75.5	49.0
1.5	75.7	50.2
1.6	76.0	51.5
1.7	76.3	52.7
1.8	76.7	53.8
1.9	77.0	54.8
2.0	77.3	56.0

TABLE F3

Calculated $R_K T^3$ values used in Figures 9-11.

T(K)	$R_K T^3$ (cm^2 K^4/W)					
	Figure 9		Figure 10		Figure 11	
	V=0.12	V=0.25	V=0.12	V=0.25	V=0.12	V=0.25
0.01	127.6	71.7	127.6	71.8	127.6	71.8
0.02	128.0	72.0	128.2	72.1	128.3	72.2
0.03	128.4	72.3	128.8	73.5	129.0	72.7
0.04	128.8	72.6	129.4	72.9	129.7	73.1
0.05	129.2	72.9	130.0	73.4	130.4	73.6
0.06	129.5	73.2	130.5	73.8	131.0	74.0
0.07	129.7	73.4	131.0	74.1	131.6	74.5
0.08	129.9	73.6	131.4	74.5	132.1	74.9
0.09	130.0	73.8	131.8	74.8	132.6	75.3
0.1	130.1	73.9	132.1	75.1	133.1	75.7
0.2	126.0	72.4	131.8	75.9	134.9	77.7
0.3	113.2	65.6	123.7	72.4	130.7	76.4
0.4	94.8	55.1	108.2	64.3	120.3	71.4
0.5	77.3	44.8	89.1	53.9	104.8	63.3
0.6	63.6	37.2	71.0	43.5	86.7	53.5
0.7	51.7	30.9	57.9	35.8	70.9	44.4
0.8	46.9	28.4	49.7	30.9	59.2	37.4
0.9	45.5	27.6	44.8	27.8	51.1	32.5
1.0	45.3	27.5	41.7	25.9	45.3	29.0
1.1	45.7	27.7	40.1	24.8	42.0	26.9
1.2	46.5	28.4	39.2	24.3	39.6	25.1
1.3	47.7	29.2	38.9	24.1	37.9	24.0
1.4	49.0	30.1	38.8	24.0	36.9	23.4
1.5	50.2	31.0	39.2	24.3	36.2	22.9
1.6	51.5	31.9	40.0	24.5	35.9	22.7
1.7	52.7	33.0	41.2	25.3	35.7	22.7
1.8	53.8	33.7	41.7	26.0	35.7	22.7
1.9	54.8	34.4	42.6	26.6	36.0	23.0
2.0	56.0	35.2	43.5	27.2	36.5	23.2

TABLE F4

Calculated $R_K T^3$ values used in Figures 12 and 13.

T(K)	$R_K T^3$ (cm^2 K^4/W)			
	Figure 12		Figure 13	
	V=0.12	V=0.25	V=0.12	V=0.25
0.01	127.7	71.8	127.8	71.8
0.02	128.4	72.3	128.7	72.4
0.03	129.2	72.8	129.6	73.1
0.04	129.9	73.3	130.5	73.7
0.05	130.7	73.8	131.4	74.3
0.06	131.3	74.3	132.3	74.9
0.07	132.9	74.7	133.1	75.5
0.08	132.5	75.2	133.8	76.1
0.09	133.0	75.6	134.5	76.6
0.10	133.5	75.9	135.2	77.1
0.2	134.1	77.5	138.5	80.4
0.3	127.5	74.9	135.4	80.0
0.4	114.3	68.0	126.3	76.0
0.5	96.6	58.5	113.3	69.2
0.6	78.7	48.2	98.8	61.2
0.7	64.3	39.9	84.7	52.5
0.8	54.3	33.9	72.6	45.2
0.9	47.7	29.8	62.8	39.1
1.0	43.5	27.1	55.3	34.3
1.1	40.7	25.3	49.5	30.7
1.2	39.1	24.3	45.2	27.9
1.3	38.2	23.7	42.2	26.2
1.4	37.7	23.4	39.8	24.6
1.5	37.7	23.4	38.1	23.6
1.6	37.8	23.6	36.9	22.9
1.7	38.3	23.9	36.1	22.4
1.8	38.9	24.3	35.7	22.1
1.9	39.5	24.7	35.4	22.0
2.0	40.3	25.2	35.3	22.0

TABLE F5

Calculated $R_K T^3$ values for Figures 14-17.

T(K)	$R_K T^3$ (cm^2 K^4/W)			
	Figure 14	Figure 15	Figure 16	Figure 17
0.01	126.2	178.2	175.3	186.0
0.02	125.3	166.0	161.2	174.5
0.03	124.4	154.8	148.3	163.3
0.04	123.5	145.1	137.1	152.8
0.05	122.5	137.1	127.6	143.1
0.06	121.5	130.5	119.8	134.2
0.07	120.5	125.1	113.3	126.2
0.08	119.4	120.6	107.8	118.9
0.09	118.3	116.8	103.1	112.4
0.1	117.1	113.5	99.0	106.5
0.2	102.4	95.3	76.2	71.7
0.3	84.7	78.6	59.9	53.5
0.4	66.9	60.6	45.1	39.8
0.5	52.2	46.4	34.2	30.0
0.6	41.3	36.3	26.6	23.3
0.7	32.9	28.8	21.0	18.2
0.8	29.2	25.4	18.7	16.1
0.9	27.9	24.2	17.8	15.3
1.0	27.4	23.8	17.5	15.1
1.1	27.4	23.7	17.4	15.0
1.2	27.7	23.9	17.6	15.2
1.3	28.2	24.3	17.9	15.5
1.4	28.8	24.8	18.3	15.8
1.5	29.4	25.3	18.7	16.1
1.6	30.0	25.8	19.1	16.4
1.7	30.7	26.3	19.5	16.8
1.8	31.2	26.8	19.9	17.1
1.9	31.7	27.2	20.2	17.4
2.0	32.4	27.7	20.6	17.8

LIST OF REFERENCES

LIST OF REFERENCES

1. C.W. Leming and G.L. Pollack, Phys. Rev. B2, 3323 (1970).

2. C.W. Leming, Sublimation Pressures of Solid Argon, Krypton, and Xenon, Ph.D. Thesis, Michigan State University (1970).

3. H.H. Chen, R.A. Aziz, and C.C. Lim, Can. J. Phys. 49, 1569 (1971).

4. M.W. Lee, S. Fuks, and J. Bigeleisen, J. Chem. Phys. 53, 4066 (1970).

5. K. Clusius, K. Schleich, and M. Vogelmann, Helv. Chim. Acta 46, 1705 (1963).

6. G. Boato, G. Casanova, and M.E. Vallauri, Nuovo Cimento 16, 505 (1960).

7. G. Boato, G. Casanova, G. Scoles, and M.E. Vallauri, Nuovo Cimento 20, 187 (1961).

8. G. Boato, G. Scoles, and M.E. Vallauri, Nuovo Cimento 23, 1041 (1962).

9. M.L. Klein, W. Blizard, and V.V. Goldman, J. Chem. Phys. 52, 1633 (1970).

10. V.V. Goldman, G.K. Horton, and M.L. Klein, Phys. Rev. Lett. 21, 1527 (1968).

11. P.L. Kapitza, J. Phys. USSR 4, 181 (1941).

12. I.M. Khalatnikov, Zh. Eksp. Teor. Fiz. 22, 687 (1952).

13. G.L. Pollack, Rev. Mod. Phys. 41, 48 (1969).

14. R.M. Mazo, Ph.D. thesis, Yale University, 1955, Chap. 1.

15. L.J. Challis, K. Dransfeld, J. Wilks, Proc. Roy. Soc. (London) A260, 31 (1961).

16. E. Long and L. Meyer, Advanc. Phys. (Phil. Mag. Suppl.) 2, 1 (1953).

17. H. Haug and K. Weiss, Phys. Letters 40A 19 (1972).

18. I.M. Khalatnikov and I.N. Adamenko, Zh. Eksp. Teor. Fiz. 63, 745 (1972).

19. R.E. Peterson and A.C. Anderson, Phys. Letters 40A, 317 (1972).

20. R.E. Peterson and A.C. Anderson, J. Low Temp. Phys. 11, 639 (1973).

21. Kuang Wey-Yen, JETP 15, 635 (1962).

22. Y. Larher, J. Chim. Phys. 65, 114 (1968).

23. G.H. Wannier, Statistical Physics, (John Wiley and Sons, Inc., New York, 1966).

24. F.W. DeWette, L.H. Fowler, B.R.A. Nijboer, Physica 54, 2 (1971).

25. L.S. Salter, Trans. Faraday Soc. 59, 657 (1963).

26. J. Kistemaker, Physica 11, 277 (1945).

27. A.E. de Vries and P.K. Rol. Vacuum 15, 135 (1965).

28. T. Takeishi and Y. Sensui, Trans. Faraday Soc. 59 2503 (1963).

29. S. Dushman, Scientific Foundations of Vacuum Technique, (John Wiley and Sons, Inc., New York), 59 (1962).

30. D.L. Losee and R.O. Simmons, Phys. Rev. 172, 934 (1968).

31. B.L. Smith and J.A. Chapman, Phil. Mag. 15, 739 (1967).

32. E.R. Dobbs, B.F. Higgins, G.O. Jones, D.C. Piercey, and D.P. Riley, Nature 178, 483 (1956).

33. J.O. Hirschfelder, C.F. Curtiss, and R.B. Bird, Molecular Theory of Gases and Liquids (John Wiley and Sons, Inc., New York, 1964).

34. P. Flubacher, A.J. Leadbetter, and J.A. Morrison, Proc. Phys. Soc. 78, 1449 (1961).

35. C. Kittel, Introduction to Solid State Physics, (John Wiley and Sons, Inc., New York, 1967).

36. I.J. Zucker, Nuovo Cimento 54, 177 (1968).

37. J.L. Opsal and D.K. Christen (unpublished).

38. M.L. Klein (private communication).

39. J. Bigeleisen, J. Chem. Phys. 34, 1485 (1961).

40. J.M. Worlock, Phys. Rev. 147, 636 (1966).

41. P.N. Thatcher, Phys. Rev. 156, 975 (1967).

42. L.I. Schiff, Phys. Rev. 59, 839 (1941).

43. E.S. Sabisky and C.H. Anderson, Phys. Rev. A7, 790 (1973).

44. W.H. Keesom, Helium (Elsevier, 1942) p. 240.

45. C.A. Swenson, Phys. Rev. 79, 626 (1950).

46. D.O. Edwards and R.C. Pandorf, Phys. Rev. 140, A816 (1965).

47. J.S. Dugdale and J.P. Franck, Phil. Trans. R. Soc. 257, 1 (1964).

48. L.M. Brekovskikh, Waves in Layered Media (Academic Press, New York, 1960) Chap. 1.

49. L.D. Landau and E.M. Lifshitz, Theory of Elasticity (Pergamon Press, Oxford, 1970) p. 153.

50. F.L. Becker and R.L. Richardson, in: Research Techniques in Non-destructive Testing, (Academic, London, 1970) Vol. 1.

51. A.C. Anderson, J.I. Connolly, and J.C. Wheatley, Phys. Rev. 135 A, 910 (1964).

52. K.N. Zinov'eva, JETP 33, 1205 (1971).

53. B.M. Abraham, Y. Eckstein, J.B. Ketterson, M. Kuchnir, and P.R. Roach, Phys. Rev. A1, 250 (1970).

54. J.H. Vignos and H.A. Fairbank, Proc. 8th Int. Conf. Low Temp. Phys. (Butterworth, 1963) p. 31. See also, Figs. 29 and 30, Chap. 21 of Liquid and Solid Helium by J. Wilks (Clarendon Press, Oxford, 1967).

55. L.J. Challis, Proc. Phys. Soc. (London) 80, 759 (1962).